

In-Situ Monitoring and Quality Assurance Algorithms for Laser Powder-Bed Fusion

by

Katayoon Taherkhani

A thesis

presented to the University of Waterloo

in fulfillment of the

thesis requirement for the degree of

Doctor of Philosophy

in

Mechanical and Mechatronics Engineering

Waterloo, Ontario, Canada, 2022

© Katayoon Taherkhani 2022

Examining Committee Membership

The following served on the Examining Committee for this thesis. The decision of the Examining Committee is by majority vote.

- External Examiner: Yu Zou, Ph.D.
Assistant Professor
Department of Materials Science & Engineering
University of Toronto
- Supervisor: Ehsan Toyserkani, Ph.D.
Professor
Department of Mechanical and Mechatronics Engineering
University of Waterloo
- Internal Member: Marco Alfano, Ph.D.
Associate Professor
Department of Mechanical and Mechatronics Engineering
University of Waterloo
- Internal Member: Arash Arami, Ph.D.
Assistant Professor
Department of Mechanical and Mechatronics Engineering
University of Waterloo
- Internal-External Member: Karim Sallaudin Karim, Ph.D.
Professor
Department of Electrical and Computer Engineering
University of Waterloo

Author's Declaration

This thesis consists of material all of which I authored or co-authored: see Statement of Contributions included in the thesis. This is a true copy of the thesis, including any required final revisions, as accepted by my examiners.

I understand that my thesis may be made electronically available to the public.

Statement of Contributions

I would like to acknowledge my co-authors who contributed to the research described in this thesis:

- Prof. Ehsan Toyserkani: Supervising the research, providing the original idea for the current thesis, editing and reviewing papers, and providing experimental facilities.
- Dr. Esmat Sheydaeian: Guiding the research work in the area of laser powder bed fusion, brainstorming, and designing samples.
- Dr. Christopher Eischer: Helping the project by providing decrypted data, guiding the study in the area of EOSTATE, and facilitating the access to the DAQ system of EOS M290.
- Dr. Martin Otto: Guiding the research work in the area of laser powder bed fusion machine, EOS M290.
- Gerd Cantzler: Helping in running the experiments with MQTT broker and updating the EOS M290 actuator.

Abstract

This dissertation describes the development of advanced in-situ defect detection algorithms using analytical and machine learning methods, followed by intermittent control systems to minimize the number of defects in parts fabricated by a commercial laser powder bed fusion (LPBF) system. To detect pores initiated from the lack-of-fusion phenomenon, light intensity emitted from the melt pool is measured by in-situ photodiode-based monitoring systems and then analyzed by multiple analytical methods, including Absolute Limits (AL), Signal Dynamics (SD), and Short-Term Fluctuations (STF). In addition, a customized Self-Organizing Map (SOM) algorithm, an unsupervised machine learning method, is developed for the same purpose. To calibrate and validate the detection methods, two sets of experiments are devised. The first set includes parts with embedded micro-voids to purposefully mimic the lack-of-fusion in parts composed of Hastelloy-X to assess the sensor response and customize algorithms in terms of required thresholds, data size, etc. The second set includes parts with stochastic/randomized pores, induced normally due to the process disturbances, to evaluate the effectiveness of the detection algorithms in the regular print. The printed samples are CT-scanned, and the data from both sets of experiments are analyzed by the segmentation method to examine the correlation. The results of the intentionally seeded defects demonstrate that voids larger than 120 μm are detectable by the AL algorithm, while the 100 μm void size is detectable by the SOM algorithm. The evaluation matrices are further used to validate stochastic/randomized distributions of pores at different process parameters, including relatively low laser powers of 175, 150, 125, and 100 W, high hatching distances of 110, 130, and 150 μm , and process speeds of 1100, 1300, and 1500 mm/sec. The results reveal that the pores created by low laser power are predicted with the True Positive (TP) rate of >75% by SOM and <30% by AL. However, the SOM exhibits TP rate results similar to those of AL in identifying pores induced due to high hatching distances and high speeds, whereas the SOM improves the True Negative (TN) rates up to 31% and 20% for such samples, respectively. Additionally, the SOM demonstrates the improvement in computational speed when it computes the defects per layer 86% faster than AL.

The SOM algorithm is integrated with a close-loop control system in an intermittent fashion when the laser power is intelligently increased in the successive layer and on top of the defective zone to heal the induced defects. To this end, the defects predicted by the SOM are clustered in a specific area of each layer using the K-means algorithm. The optimized area around the center of defects is the position at which the laser power should be changed in the following deposition layer. To identify the optimum

laser power value, various artificial voids are designed and embedded in the coupon samples. Then, a capping layer on the artificial voids is manufactured by increasing the laser power from the nominal value. Based on the optimum power and defect size, knowledge-based rules are defined to increase the laser power in the successive layer to consequently heal the defects created during the process. The new laser power value is calculated in a Laser Correction File (LCF) after the deposition of each layer. This closed-loop approach needs a Message Queuing Telemetry Transport (MQTT) broker to connect data acquisition, data correction, defect detection algorithm, LCF calculation, and the actuator (e.g., laser in this case). The controller is applied to two new sets of experiments to evaluate its performance. Its performance shows that the part density can substantially be increased when the controller is on compared to the printed parts when the controller is off.

Acknowledgments

The realization of this research work would have not been possible without the help and support of several people to whom I wish to express my gratitude.

I would like to express my sincere gratitude to my esteemed supervisor, Professor Ehsan Toyserkani, for his valuable support, guidance, advice, and encouragement through the completion of the work. Under his mentorship, I had the opportunity to advance my scientific knowledge at the University of Waterloo.

I hereby acknowledge my thesis examining committee members, Prof. Yu Zou from the University of Toronto, Prof. Marco Alfano, Prof. Arash Arami, and Prof. Karim Sallaudin Karim from the University of Waterloo, for taking the time to review my thesis and provide their valuable feedback and suggestions.

I would also like to acknowledge the financial support of the Natural Sciences and Engineering Research Council of Canada (NSERC) Network for Holistic Innovation in Additive Manufacturing (HI-AM), the Department of Mechanical and Mechatronics Engineering of the University of Waterloo, and Women in Engineering of the University of Waterloo.

This academic experience has shown the value of interdisciplinary collaboration. I had the unique pleasure to work with the wonderful research group of EOS Company, Dr. Christopher Eischer, Dr. Martin Otto, and Gerd Cantzler, working together toward achieving a unified goal.

I would like to thank my current and past colleagues at the Multi-scale Additive Manufacturing (MSAM) Laboratory research at the University of Waterloo, Dr. Esmat Sheydaeian and Henry Ma, for their assistance and advice.

I would like to offer thanks to the technical staff team at the University of Waterloo, Jerry Rathapakdee, Karl Rautenberg, James Farnsworth, and Robert Cieniawski, for their amazing effort in assisting me with the experimental tests.

Finally and most importantly, I owe my deep and sincere gratitude to my parents and brothers for their continuous and unparalleled love, help, and support. I also extend my special thanks to my husband, Meisam, for his cheerful motivation and support in enabling me to pursue my academic goals.

Dedication

To my beloved Family

Table of Contents

Examining Committee Membership.....	ii
Author’s Declaration	iii
Abstract	v
Acknowledgments	vii
Dedication	viii
List of Figures	xii
List of Tables.....	xv
Chapter 1 . Introduction.....	1
1.1 Research Motivation.....	1
1.2 Research Objectives	2
1.3 Thesis Outline.....	5
Chapter 2 . Background and Literature Review	7
2.1 Abstract	7
2.2 Additive Manufacturing (AM) and Laser Powder-Bed Fusion (LPBF).....	7
2.3 Fundamental Challenges of LPBF.....	7
2.4 Formation of Defect in LPBF	8
2.5 Quality Assurance	8
2.5.1 In-situ sensors.....	9
2.5.2 Monitoring techniques.....	17
2.6 Summary	23
Chapter 3 . Development of a defect-detection platform using photodiodes signals collected from the melt pool of laser powder-bed fusion.....	24
3.1 Abstract	24
3.2 Methodologies and Experimental Setups	24

3.2.1 Design of experiments and process parameters.....	24
3.2.2 In-situ monitoring devices	28
3.2.3 Analysis of the data collected by in-situ monitoring	29
3.2.4 Image processing algorithm.....	34
3.2.5 Statistical analysis	36
3.2.6 Computed tomography (CT-Scanning)	36
3.3 Results and Discussion.....	40
3.3.1 Analysis of the data collected by Absolute Limits algorithm.....	40
3.3.2 Computed tomography (CT-Scanning)	46
3.4 Summary	56
Chapter 4 . An unsupervised machine learning algorithm for in-situ defect-detection in laser powder-bed fusion	57
4.1 Abstract	57
4.2 Methodologies and Experimental Setups	57
4.2.1 Design of experiments	57
4.2.2 The clustering algorithm.....	60
4.2.3 Computed tomography (CT-Scanning)	63
4.3 Results and discussion.....	65
4.3.1 Predicting porosity using SOM and comparing the result with CT-scanning	65
4.4 Summary	74
Chapter 5 . Development of an intermittent controller for LPBF.....	75
5.1 Abstract	75
5.2 Methodologies and Experimental Setups	75
5.2.1 The detrending algorithm	75
5.3 Design of experiments	81

5.3.1 Identifying the optimum amount of laser power to heal defects	81
5.3.2 Validating the controller by two different sets of experiments	83
5.4 Computed tomography (CT-Scanning)	86
5.4.1 N-series sample	86
5.4.2 X-series sample	87
5.4.3 Y-series sample	88
5.5 Results and discussion	89
5.5.1 Identifying the optimum amount of laser power to heal defects	89
5.5.2 Validating the controller by two different experimental sets	92
5.6 Summary	95
Chapter 6 . Conclusions and Future Work	97
6.1 Conclusions	97
6.2 Recommendations and Future Work	98
Letter of copyright permission	100
References	110

List of Figures

Figure 1-1: Concept of closed-loop control for a typical LPBF process	2
Figure 1-2: Graphical flowchart of the research conducted in the current thesis	4
Figure 2-1: Sub-categories of radiative and non-radiative sensors used in LPBF.....	10
Figure 2-2: Relative emphasis of in-situ sensors reported in the literature using LPBF	10
Figure 2-3: Schematic cross-section of P-N photodiode (Republished with permission of John Wiley and Sons, from [3])	11
Figure 2-4: The on-axial position of (a) pyrometer (Source: Republished with permission of Elsevier, from [41]) and (b) ICI (Source: Republished with permission of Elsevier, from [42])	13
Figure 2-5: The off-axial position of (a) camera (Source: Republished with permission of Elsevier, from [43]) and (b) DLSR camera (Source: Republished with permission of Elsevier, from [44]).....	14
Figure 2-6: Relative emphasis of in-situ sensors arrangement based on their types reported in the literature using LPBF	14
Figure 2-7: The procedure of segmentation method from initialization (first row) to the final map (second row) (Source: Republished with permission of Elsevier, from [56])	18
Figure 2-8: Three Layer-wise Optical Tomography (OT) images used in LPBF (Source: Republished with permission of AIP Publishing, from [57])	19
Figure 2-9: (a) Mean value and (b) standard deviation of the GP prediction over the processing parameters; black dots represent the locations of the training data points showing very low values of the standard deviation. (Source: Republished with permission of Springer Nature, from [74]).....	22
Figure 3-1: CAD model of reference samples: a) series R b) series T.	25
Figure 3-2: 2D cross-sections of samples showing the distribution of the artificial voids in samples: a) R2 which includes 6 similar sets of three sizes of defects (\emptyset , $H=200 \mu\text{m}$, \emptyset , $H=150 \mu\text{m}$, and \emptyset , $H=100 \mu\text{m}$), b) R3 which is including 3 similar sets of six sizes of defects (the diameter: $\emptyset =320 \mu\text{m}$, $\emptyset=280 \mu\text{m}$, $\emptyset=240 \mu\text{m}$, $\emptyset =200 \mu\text{m}$, $\emptyset=160 \mu\text{m}$, and $\emptyset=120 \mu\text{m}$ and the height: $H=200 \mu\text{m}$), c) R4 which is including 6 similar sets of three sizes of defects ($\emptyset=300 \mu\text{m}$, $\emptyset=250 \mu\text{m}$, and $\emptyset=200 \mu\text{m}$), and d) R5 which is including 5 similar sets of one size of the defect (\emptyset , $H=200 \mu\text{m}$) printed in 3 scenarios of distribution (5×5 , 9×9 , and 8×8). \emptyset is diameter and H is height, both in μm	26
Figure 3-3: Samples layout on the build plate: a) R series; b) T series.	28
Figure 3-4: Schematic of LPBF equipped with on-axis and off-axis photodiodes.....	29
Figure 3-5: Schematic of a) photodiode data collection, b) applying one of the algorithms and tuning threshold ranges, c) magnifying part of the signal to show signal perturbation, and d) one layer of the sample included yellow pixels which are corresponding to the location of signal perturbation.	30
Figure 3-6: Schematic of a) Absolute Limits (AL), b) Signal Dynamics (SD), and c) Short Term Fluctuations (STF) after applying the threshold.	31
Figure 3-7: Schematic of a) sample R2 included artificial voids and five successive layers on top of the artificial voids with radius and height of b) $100 \mu\text{m}$, c) $150 \mu\text{m}$, and d) $200 \mu\text{m}$. .	32
Figure 3-8: a) An example of an image generated by the software for one layer of the print, b) Selection of 49 regions of interest around each defect in sample R2 at Location 1.	35

Figure 3-9: The schematic of a) a sample that is segmented in 82 batches, b) a batch, which is divided into 4356 voxels (which includes three layers).....	37
Figure 3-10: Two adjacent voxels with considering area of a) 30 μm and b) 60 μm from each edge.	37
Figure 3-11: The schematic of when one yellow pixel located at the edge of voxel and a) no yellow pixels identified in the adjacent voxel, b and c) two yellow pixels identified in one of the voxels, and d) two yellow pixels identified in both voxels (please check Figure 3-9c for the size of voxels).	38
Figure 3-12: Schematic to compare the CT-Scan and EOSTATE software results to establish a matching matrix.	39
Figure 3-13: The population and distribution of indications for AL algorithm – R-series (Figure 3-3a).	41
Figure 3-14: The percentage of average and standard deviation of yellow indicators in the region of interests for the selected layers based on the output of the AL algorithm (Samples R2, R3, R4, R6, R7, and R8 are shown by pink, teal, purple, orange, green, and blue, respectively).	43
Figure 3-15: The percentage of average and standard deviation of yellow indicators in the region of interest for the selected layers and after applying the AL algorithm (Sample R5). D1, D2, and D3 mean three different void distribution embedded in sample R5 (D1= 5 \times 5, D2= 8 \times 8, and D3= 9 \times 9).	44
Figure 3-16: CT data for a) R4- location 4 b) R7- location 1 c) T4- location 4.	47
Figure 3-17: The amount of shrinkage in the sample a) R2- location 4 b) R3- location 4 c) R4- location 4 d) R5- location 4 for each type of defects.	48
Figure 3-18: The amount of shrinkage in the sample R7 a) Location 1, b) Location 2, c) Location 3, d) Location 4, e) Location 5, f) Location 6, g) Location 7, and h) Location 8....	52
Figure 3-19: The amount of shrinkage in the sample R8 a) Location 1, b) Location 2, c) Location 3, d) Location 4, e) Location 5, f) Location 6, g) Location 7, and h) Location 8....	52
Figure 4-1: CAD model of a) R1-1 [40] () and b) P1-1.....	58
Figure 4-2: P-series sample layout on the build plate.....	59
Figure 4-3: SOM concept and iterations to map nodes to the input space (redraw and adapted from [88]).....	62
Figure 4-4: a) Neighbour weight distances and b) the population size of each cluster after applying the SOM with 1 \times 9 clusters	63
Figure 4-5: μCT scan result of front view of a) R2, b) R3, c) R4, and d) R5 samples, and top view of e) R2, f) R3, g) R4, and h) R5 samples.....	64
Figure 4-6: CT scan result of P-series sample	65
Figure 4-7: Defect detection procedure which demonstrated a) sample geometry with artificial defects in layer n , b) capping layer geometry of layer $n+1$, c) light intensity signal of capping layer on the layer $n+1$, d) light intensity signal of layer $n+1$ after applying the SOM with 1 \times 9 dimensions, and e) capping layer geometry of layer $n+1$ after applying the SOM with 1 \times 9 dimensions	66
Figure 4-8: Defect position identified by a) AL-EOSTATE, b) SOM, and c) CT-scan in sample R5 with the distribution of 8 \times 8.....	69

Figure 5-1: One example of the defect detection procedure in which a) a layer with artificial defects with the size of $200\ \mu\text{m}\times 200\ \mu\text{m}\times 200\ \mu\text{m}$ and b) the positions of defects after applying the SOM algorithm on the capping layer on artificial defects in Sample R2 76

Figure 5-2: One example of a) applying the SOM algorithm on the capping layer on artificial defects to highlight the positions of defects shown by red colour and b) identifying the center of each cluster by K-means algorithm (artificial defects size is $200\ \mu\text{m}\times 200\ \mu\text{m}$ embedded in Sample R2)..... 78

Figure 5-3: Considering a square with a size of $0.6\times 0.6\ \text{mm}^2$ around the center of clusters in layer $n+1$ printed on top of layer n with defect size of \emptyset , $H=200\ (\mu\text{m})$ 79

Figure 5-4: CAD model of Samples: a) N1, b) N2, c) N3, and d) N4 82

Figure 5-5: 3D and 2D cross-sections of samples showing the distribution of the artificial defects in Samples: a) N1, b) N2, c) N3, and d) N4. 82

Figure 5-6: (a) Sample layout and (b) printed samples on the build plate..... 83

Figure 5-7: a) 3D view of X1, b) 3D view of X2, c) x-z coordinate of X-series samples, and d) x-y coordinate of X-series samples showing the distribution of the artificial defects 84

Figure 5-8: a) 3D view of Y1 and b) 3D view of Y2..... 85

Figure 5-9: (a) Sample layout of X-series, (b) printed X-series samples on the build plate, c) Sample layout of Y-series, and (d) printed Y-series samples on the build plate 86

Figure 5-10: CT scan result of N-series sample..... 87

Figure 5-11: CT scan result of Samples a) X1 and b) X2..... 88

Figure 5-12: CT scan result of Samples a) Y1 and b) Y2..... 88

Figure 5-13: Percentage of healing of five sizes of artificial defects after applying sixteen amounts of laser power 90

Figure 5-14: Percentage of sizes of μm -healed defects after applying sixteen amounts of laser power on the consecutive layer of defects with the size of a) \emptyset , $H=400\ \mu\text{m}$, b) \emptyset , $H=300\ \mu\text{m}$, and c) \emptyset , $H=200\ \mu\text{m}$ 91

Figure 5-15: The histogram of pores identified in samples a) Y1 and b) Y2 95

List of Tables

Table 2-1: The sampling frequency and wavelength of photodiodes used in the LPBF studies, as well as any additional filters/lens	12
Table 2-2: Mapping of the literature on in-situ photodiode of LPBF to monitor the process signature.....	15
Table 2-3: Some commercial sensors mounted on the LPBF machines.....	17
Table 2-4: Machine learning techniques applied in LPBF to detect porosity.....	20
Table 3-1: Types and print parameters in print 1: 8 samples printed in 6 locations.....	27
Table 3-2: Types and print parameters in print 2: 4x6 samples.....	27
Table 3-3: Applying the detection algorithms on the five consecutive layers after the defect (Layer 0: last layer of the international defect) (sample R2, defect radius= 200 μ m and defect height=200 μ m).....	33
Table 3-4: Applying the AL algorithm to the datasets collected by on-axial and off-axial photodiodes on layer 1 based on the explanation in Table 3 3 (sample R2, defect radius= 200 μ m and defect height=200 μ m).....	34
Table 3-5: Number of pixels per radius of each circular area for each sample with different defect size (each pixel is representing the average value of intensity signal in the area of 5.55x5.55 (μ m \times μ m)).....	35
Table 3-6: Confusion matrix to compare the prediction of the algorithm (AL) and the actual defect (CT-scan).....	38
Table 3-7: The Reference of Figure 3-14 and Figure 3-15.....	42
Table 3-8: The range of p-value from ANOVA single factor analysis of the variance.....	46
Table 3-9: The percentage of identification for each size of the defect and density of each sample.....	48
Table 3-10: The percentage of identification for each size of the defect and density of sample R7.....	50
Table 3-11: The percentage of identification for each size of the defect and density of sample R8.....	51
Table 3-12: Accuracy (%) of AL algorithm to predict pores based on the CT-Scan result for sample R7 with two different sizes of distance (30 μ m and 60 μ m) from each voxel to avoid missing any partial pores or pores located on the edge of the voxel.....	53
Table 3-13: Accuracy (%) of AL algorithm to predict pores based on the CT-Scan result for sample R8 with two different sizes of distance (30 μ m and 60 μ m) from each voxel to avoid missing any partial pores or pores located on the edge of the voxel.....	53
Table 3-14: Evaluation metrics of AL algorithm based on the CT-Scan result for sample R7.....	54
Table 3-15: Evaluation metrics of AL algorithm based on the CT-Scan result for sample R8.....	54
Table 3-16: Evaluation metrics of AL algorithm based on the CT-Scan result for sample T3.....	55
Table 3-17: Evaluation metrics of AL algorithm based on the CT-Scan result for sample T4.....	55
Table 4-1: Types and print parameters in P-series sample	59
Table 4-2: Density of P-series sample	65

Table 4-3: Applying SOM algorithms with 5, 6, 7, 8, 9 and 10 clusters to the on-axial photodiode signal to layer $n+1$ (sample R2: defect radius= 150 μm and defect height= 150 μm , sample R3: defect radius= 200 μm and defect height= 160 μm , sample R4: defect radius= 250 μm , and sample R5: defect radius= 200 μm , defect height= 200 μm , and defect distribution= 5×5)	67
Table 4-4: Comparison between the average radius of identified defects after applying 1×8 and 1×9 SOMs in layer $n+1$ with the average radius of defects in layer n	68
Table 4-5: The percentage of identification for each size of the defect in samples R2-R5....	69
Table 4-6: Averaged TP and TN raters by comparing 1×9 SOM algorithm and CT-Scan for samples P2, P3, and P4	70
Table 4-7: TP and TN raters by comparing the 1×9 SOM algorithm and CT-Scan for sample T2	71
Table 4-8: TP and TN raters by comparing SOM algorithm and CT-Scan for samples P5, P6, and P7.....	71
Table 4-9: TP and TN raters by comparing SOM algorithm and CT-Scan for sample T3.....	72
Table 4-10: TP and TN raters by comparing SOM algorithm and CT-Scan for samples P8, P9, and P10.....	72
Table 4-11: TP and TN raters by comparing SOM algorithm and CT-Scan for sample T4... 73	73
Table 4-12: Computational time of AL and SOM for sample P2- 1 for layers 1, 30, 60, 90, 120, 150, 180, 210, and 240.....	74
Table 5-1: Calculation of numbers of artificial defects in Samples R2, R3, and R4.....	77
Table 5-2: Average and standard deviations of numbers of indicators in Samples R2, R3, and R4 in the capping layer and defect zones based on the size	77
Table 5-3: The potential size of defects based on the identified indicators.....	78
Table 5-4: Average and standard deviations of maximum radius of X and Y directions of clusters in Samples R2 and R3 in the capping area on defective zones based on defect size	79
Table 5-5: Comparing the computational time of MATLAB and LabVIEW	80
Table 5-6: Laser power variation at capping layer in four parts of each sample based on their location.....	83
Table 5-7: Percentage of healing of five sizes of artificial defects after applying sixteen amounts of laser power	89
Table 5-8: Change of laser power in a capping zone on artificial defects based on their id based on analysis (Figure 5-7)	92
Table 5-9: Change of laser power in a capping zone on artificial defects based on their id in the real-time process	93
Table 5-10: The actual radius of defects embedded in X1 and X2 based on the CT-scan results	93

Chapter 1. Introduction

1.1 Research Motivation

Additive Manufacturing (AM) has changed the entire manufacturing field by offering unique features for fabricating complex shapes with superior mechanical properties. In the last decades, through exponential advancement, AM has been promoted from a prototyping to a mass production platform. One of the advanced AM technologies is Laser Powder-Bed Fusion (LPBF). During the LPBF process, a moving laser beam fuses thin layers of powder particles that have been spread on the build plate by a recoater. The feed container is raised, and a layer of powder material is deposited on the build platform. After a layer is deposited, the laser selectively scans and melts powder based on the Computer-Aided Design (CAD) model. The process is repeated until the build of the whole part is completed [1].

Although the LPBF process has numerous benefits, many LPBF challenges remain unaddressed, such as dimensional errors, undesired porosity, delamination of layers, and undesired material properties. The high sensitivity of LPBF processes to disturbances is one of the main challenges. For example, a small change in the laser power can cause a large change in the melt pool size. Additionally, the LPBF process is governed by many process parameters, such as laser power, scan strategy, hatch spacing, scan speed, gas flow, and recoater speed. These factors profoundly affect the process, causing defects [1], [2]. To make the process more stable and less susceptible to disturbances, it is important to understand how the parameters affect the process and product quality. Typically, the AM process parameters can be categorized into two groups: 1- intrinsic and 2- extrinsic. Intrinsic parameters are those related to the substrate and powder properties. On the other hand, extrinsic parameters are related to the hardware used in the process, such as the laser, powder feeder, recoater, positioning system, etc. In general, there is no direct control of intrinsic parameters; however, the effects of changes in intrinsic parameters can be compensated for by controlling the extrinsic parameters. The control of extrinsic parameters is relatively easy with most of the parameters mentioned above. Commercial systems are equipped with built-in controllers that allow users to set the desired values. This is the approach that is used in many applications. Much trial and error are needed to obtain parameters that result in good quality for a specific application. These parameters are then used in open-loop process control. The controllable parameters are set to predefined values, and there is no feedback from the process output to adjust the parameters. Additionally, open-loop control of AM processes is useful when the application is fixed and must be repeated. Finding the right parameters is very time-consuming; however, as long as there is no change in the application, this control method is effective and efficient.

However, the need for quality assurance has pushed industries and academies to look at closed-loop control of the process. By applying a closed-loop controller, process parameters (e.g., laser power) can be monitored in real-time and changed during the process to tune one or more process parameters by sending an order to an actuator(s) for fabricating desired parts, as demonstrated in Figure 1-1.

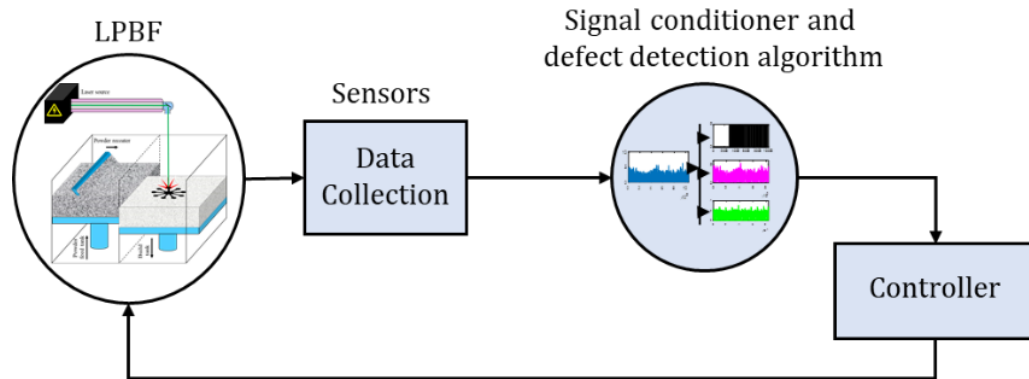


Figure 1-1: Concept of closed-loop control for a typical LPBF process

1.2 Research Objectives

The main objective of this thesis is the development of customized in-situ defect detection methods using analytical and machine learning algorithms, as well as the development of intermittent control systems for the commercial LPBF machine to minimize the number and size of lack-of-fusion defects created in parts during the fabrication. To achieve this goal, the following research tasks were undertaken:

- Analyzing the light intensity signal captured by on-axial and off-axial photodiodes and then correlating signal disturbances to artificial and randomized lack-of-fusion defects.
- Investigating the effectiveness of three analytical algorithms to identify defects formed due to the lack-of-fusion (LoF) phenomenon by comparing the results of these algorithms with the results of a Computed Tomography scan (CT- scan) through the volumetric approach.
- Customizing the Self-Organizing Map (SOM) algorithm by applying it on the light intensity signal for clustering the intensity signal, mapping each cluster to the geometry, and identifying the corresponding cluster to the lack-of-fusion defects by comparing the result with the CT- scan through the volumetric approach.

- Clustering the identified indicators using the K-means algorithm in each 1×1 (mm^2) and optimizing the targeted area around the center of clusters as the position at which the laser power should be changed.
- Designing and analyzing various sizes of artificial defects when their capping layer was fabricated by increasing the laser power in order to identify the optimum laser power for healing/minimizing lack-of-fusion defects.
- Using Data Acquisition system (DAQ) to collect real-time data from the process, including laser X-Y geometry, laser power, laser modulation, and off-axial and on-axial intensity signals.
- Connecting the data acquisition system, defect detection method, and the actuator via a Message Queuing Telemetry Transport (MQTT) broker for providing communication among different components of the control system.
- Testing the intermittent control system by means of two sets of experiments and validating the effectiveness of the controller by comparing the results with CT-scan results.

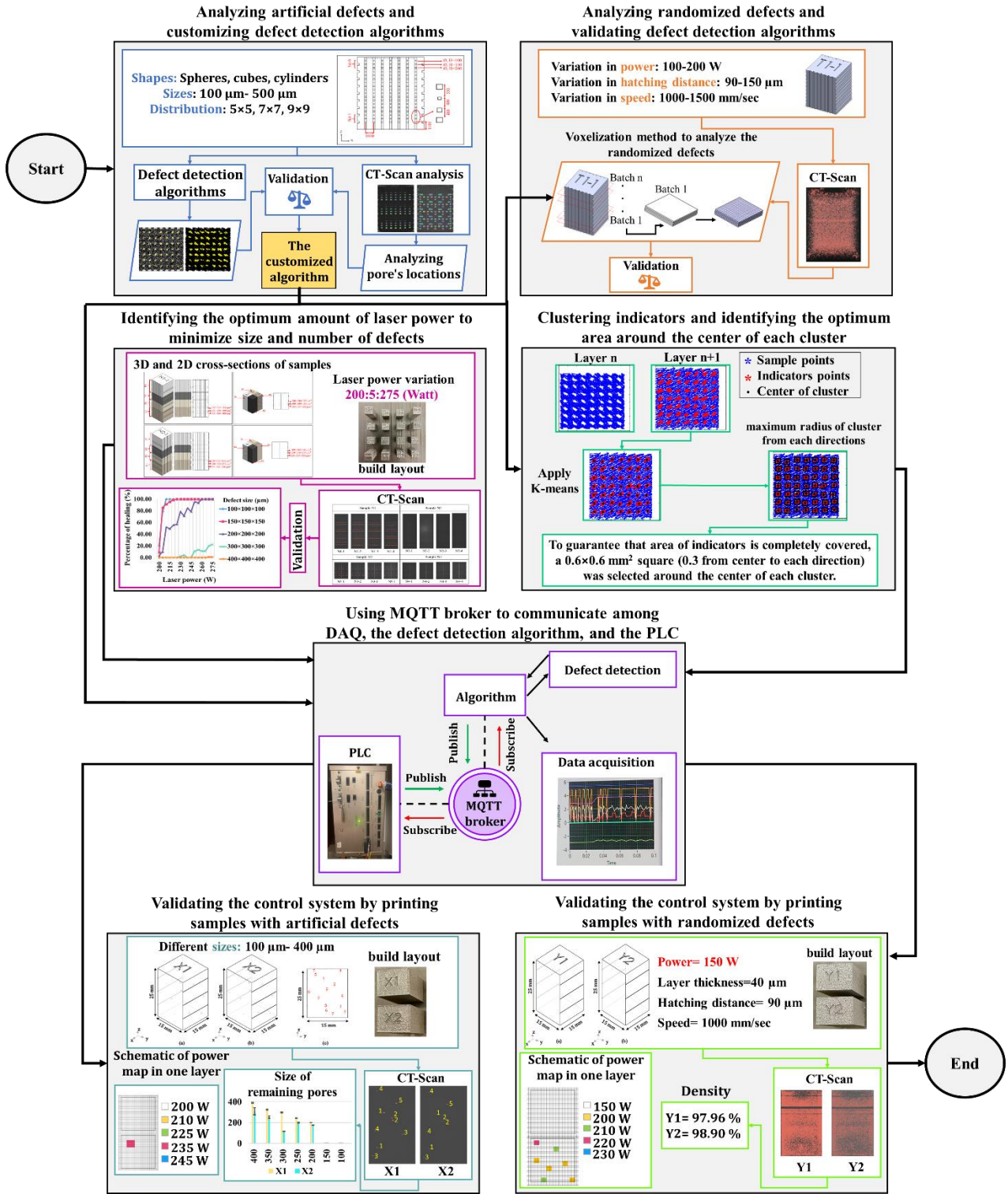


Figure 1-2: Graphical flowchart of the research conducted in the current thesis

1.3 Thesis Outline

This thesis includes six chapters. Chapter 1 outlines the problem definition, motivation, and objectives of the present research. The related literature on the lack-of-fusion defects, in-situ monitoring devices, and monitoring algorithms applied to the LPBF studies is reviewed in Chapter 2. Three analytical defect detection algorithms, such as Absolute Limits (AL), Signal Dynamics (SD), and Short-Term Fluctuations (STF), are analyzed and customized in Chapter 3 to identify the defects created in the fabricated part. To improve the detection rate and increase the speed of detection, the Self-Organizing Map (SOM) algorithm is used to detect lack-of-fusion defects in Chapter 4. In both Chapter 3 and Chapter 4, defect detection algorithms are validated using CT-scan through a volumetric approach. Chapter 5 discusses the development of the intermittent control system in which knowledge-based rules are defined for increasing the laser power during the process to minimize lack-of-fusion defects in the part fabricated by a commercial LPBF system. Finally, conclusions and future work are outlined in Chapter 6.

Chapter 2 to Chapter 5 are adapted from the author's published work and manuscripts submitted or will be submitted for publication, as follows:

- Chapter 2 is some sections of the book published in John Wiley and Sons and some sections of the review article which will be submitted in the following year:
 - E. Toyserkani, D. Sarker, O. O. Ibhado, F. Liravi, P. Russo, K. Taherkhani, *Metal Additive Manufacturing*, 1st ed. John Wiley, 2021, doi: 10.1002/9781119210801. [3]
 - K. Taherkhani and E. Toyserkani, “A critical review of in-situ sensors and machine learning monitoring algorithms in laser powder-bed fusion”.
- Chapter 3 is a journal article published in the Journal of Additive Manufacturing
 - K. Taherkhani, E. Sheydaei, C. Eischer, M. Otto, and E. Toyserkani, “Development of a defect-detection platform using photodiode signals collected from the melt pool of laser powder-bed fusion,” *Addit. Manuf.*, vol. 46, p. 102152, Oct. 2021, doi: 10.1016/J.ADDMA.2021.102152. [4]
- Chapter 4 is a journal article submitted to the Journal of Manufacturing Processes

- K. Taherkhani, C. Eischer, and E. Toyserkani, “An unsupervised machine learning algorithm for in-situ defect-detection in laser powder-bed fusion”.
- Chapter 5 is an article that will be filed a patent and then submitted to the Journal.

The content of these publications has been slightly modified to fit within the scope of this thesis. The license agreements are provided in the Letter of Copyright Permission section.

Chapter 2. Background and Literature Review

2.1 Abstract

Laser Powder Bed Fusion (LPBF) is one type of Additive Manufacturing (AM) process to fabricate high-density and high-quality complex parts. However, the lack of uniform quantities that affect serial production is critical in LPBF. Therefore, in-situ sensing devices and monitoring techniques are introduced to obtain in-situ data and analyze them to enhance the knowledge of the process. In this chapter, the fundamental challenges of LPBF are discussed. To address LPBF challenges, quality assurance method is defined. Also, in-situ sensors that are implemented in LPBF-AM are reviewed. Additionally, this study enlightens the latest statistical and machine learning applications (ML) to detect porosities created during LPBF.

2.2 Additive Manufacturing (AM) and Laser Powder-Bed Fusion (LPBF)

The advent of Additive Manufacturing (AM) technology played a transformational role in industrial application domains. AM is a layer-by-layer fabrication technology by which three-dimensional parts are directly developed from CAD models [3]. Through intensive research over the past three decades, significant progress has been made in the development and commercialization of the AM process in aerospace, automotive, biomedical, energy, and other industrial fields [5], [6].

One of the advanced AM technologies is Laser Powder-Bed Fusion (LPBF). During the LPBF process, a layer of material with a specific thickness is spread over the build platform. Then, a laser selectively scans the powder layer and melts powder particles according to the CAD model. The process is repeated until the desired part is completed [3]. LPBF is one of the most used AM techniques due to its capability to select a variety of materials, including titanium alloy [7], [8], nickel-based super-alloys [9], [10], aluminum alloys, and stainless steels [11]. Also, due to the ability of the process to produce high-density and high-quality complex parts, LPBF is widely used in manufactured Companies.

2.3 Fundamental Challenges of LPBF

While the LPBF technique has significantly progressed, many fundamental challenges remain unaddressed, such as dimensional errors, undesired porosity, delamination of layers, and poor or undefined material properties. Part quality is more than just the shape of the final part. The quality is fundamentally a part's ability to perform the task for which it was designed while maintaining its

structural integrity. Contributing factors are usually included in a part's specifications and typically include geometry, surface finish, and mechanical properties. Extensive research and various approaches were studied to improve the quality of fabricated parts through material characterization; however, many issues have not been solved, such as predicting and controlling defects inside the products. Since inner defects have one of the most adverse effects on mechanical properties, experimental advances rely on trial and error methods, which are costly and inefficient.

Another challenge that could affect the form and structure of a part is the number of parameters involved in LPBF. Some parameters are not controllable, but they could also influence the quality of the process, such as gas flow pressure and powder uniformity. These parameters can adversely influence the quality, resulting in low repeatability. On the other hand, the controllable parameters should also be optimized by experimental trial and error.

2.4 Formation of Defect in LPBF

As defects are one of the challenges of LPBF, detecting defects is an essential step towards increasing process confidence. Understanding the defects and conditions in which they are created can lead to better processing strategies. Two classifications of defects are keyhole and lack-of-fusion, and they are defined as below:

- 1- Key-hole: If the powder has a low packing density, the gas between the powder particles dissolves in the molten pool. The dissolved gas cannot exit the molten pool, forming a keyhole in the manufactured component. Also, when the energy input is high, more powders are over-melted, and the entrapped gas is generated in the fabricated part.
- 2- Lack-of-fusion: If the energy input is insufficient, the powder is not melted completely, and a new layer cannot be deposited on the previous layer efficiently. So, the un-melted powder remains inside the manufactured part, known as lack-of-fusion.

Many experts have conducted research to identify the optimum value of process signature to reduce porosity in the manufactured part [12]–[14]. However, the best way to reduce the defect would be quality assurance.

2.5 Quality Assurance

Quality assurance (QA) could be one solution to achieve enhanced quality AM products. The first step moving towards QA is enhancing the knowledge of the process. As a result, in-situ sensors are installed

to provide valuable information. Thus, real-time monitoring will help shed insight into the process and understand deviations through data collected by sensors. However, gathering millions of data per layer creates a big data set that requires data mining algorithms to analyze. Thus, sensing, documenting, and analyzing the dataset during the real-time process are crucial.

On the other hand, the quality assurance process must be automatically applied in a minimum amount of time. In this way, serial AM productions would be feasible in less time and at lower costs. Thus, in this thesis, some types of in-situ sensors installed in LPBF will be reviewed in Section 2.5.1, emphasizing the photodiode. Then, the monitoring techniques to analyze the in-situ data to identify porosity will be discussed in Section 2.5.2.

2.5.1 In-situ sensors

Since quality assurance and repeatability are critical problems in LPBF, many experts and commercial vendors have installed in-situ sensing equipment to capture information from the process, leading to understanding and controlling it. Types and set-up strategies of in-situ sensors are discussed in the following sections:

2.5.1.1 Types

There are several classifications of sensors suggested by different authors [3], [15]. In-situ sensors can be categorized into two major groups: radiative and non-radiative.

- Radiative sensors sense and measure radiative information. This type of sensor is widely used in manufacturing because of its satisfactory features. The radiative sensors can be classified based on their principles and outputs.
- Non-radiative sensors could measure and then convert the physical behavior of the process to the electrical signal.

Each of these categories includes sub-categories, as demonstrated in Figure 2-1.

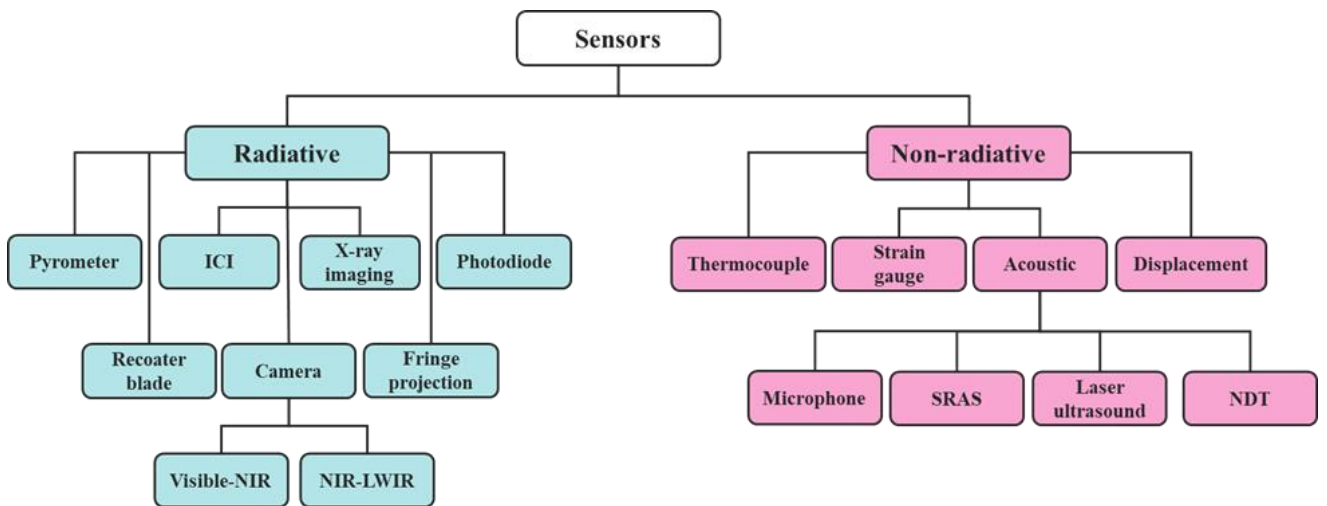


Figure 2-1: Sub-categories of radiative and non-radiative sensors used in LPBF

Figure 2-2 illustrates the volume of published papers using in-situ sensors until mid-2021. According to Figure 2-2, most studies have used radiative sensors (220 papers) followed by non-radiative sensors (31 papers). In the literature among radiative sensors, most of the papers associated with the use of the visible to near-infrared (NIR) camera (101 papers) followed by the NIR to long-wavelength infrared (LWIR) camera (37 papers), X-ray imaging (30 papers), the photodiode (21 papers), the pyrometer (16 papers), the fringe projection (7 papers), the ICI (5 papers), and the scanner sensor (3 papers). According to Figure 2-2, the use of non-radiative sensors is limited to the acoustic sensor (22 papers), the thermocouple (4 papers), strain gauge (3 papers), and the displacement sensor (2 papers).

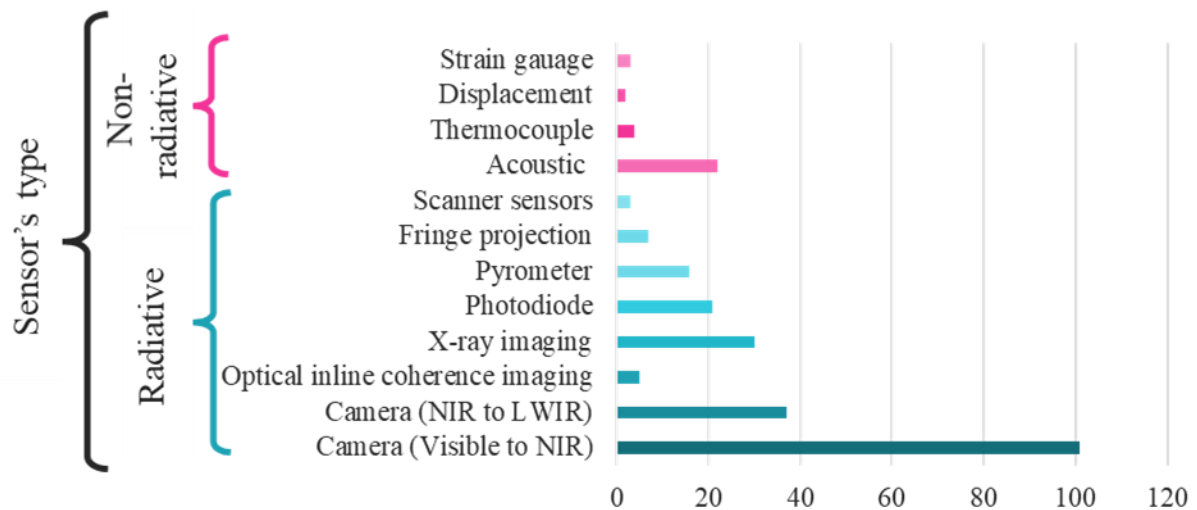


Figure 2-2: Relative emphasis of in-situ sensors reported in the literature using LPBF

For the purpose of this study, the commercial photodiode is used. Thus, the photodiode characteristics will be discussed in the following section.

- Photodiode

A photodiode is a semiconductor device with a P-N junction that converts photons into an electrical current. The P-layer junction has positive charges, and the N junction contains electrons or negative charges. Semiconductor materials (e.g., Silicon and Germanium) have a band-gap (energy gap) between their conduction and depletion bands. Enough energy (more than the energy gap) is required to stimulate electrons to move and transfer from the conduction band to the depletion band [16], [17]. When the light intensity with greater than the gap energy hits the photodiode, resulting in electrons' movement. The electrons' movement towards the cathode and holes' movement towards the anode create the electrical current, as shown in Figure 2-3. The generated electrical current is a function of applied voltage, electron charge, Boltzmann constant, and absolute temperature.

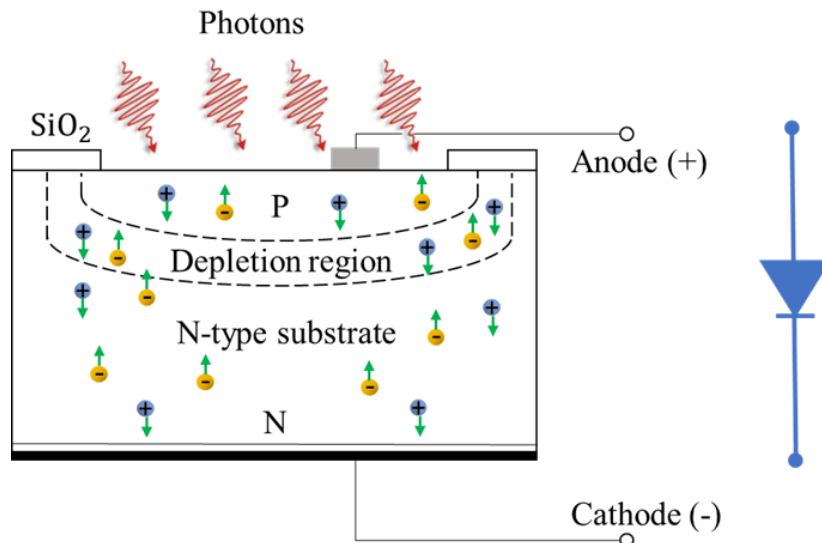


Figure 2-3: Schematic cross-section of P-N photodiode (Republished with permission of John Wiley and Sons, from [3])

For instance, silicon has an average of 1.12 electron volt energy gap between its bands [18]. It means silicon requires more than 1.12 electron volt energy to transfer the electrons. 1.12 eV energy corresponds to a wavelength shorter than 1100 nm based on Planks' law.

Although Photodiodes are commonly used in optical communication [19], [20], medical devices [21][22], and photography [23], [24], it also has applications in the LPBF process to sense thermal radiation and light emission. The thermal information is analyzed to detect dimension accuracy [25], [26], [27], [28], overheating [29]–[31], balling effect [31], abnormal process [32], [33], and porosity [4], [33]–[35].

For the first time, Kruth *et al.* [26] and Berumen *et al.* [27] installed the photodiode to monitor reflected intensity signals. A photodiode was implemented with a wavelength of 400-1000 nm and a sampling frequency of 10 kHz to measure the mean radiation emitted from the melt pool. The combination of photodiode and camera provided information to study the dimensional accuracy. Clijsters *et al.* [29], Craeghs *et al.* [30], and Gestel *et al.* [31] also placed the photodiode and the camera to monitor overheating. Gestel *et al.* showed the use of Thorlabs PDA36A photodiode (wavelength range of 350-1100 nm) to sense light intensity signals. In the study, two CMOS cameras (wavelength range of 700-1000 nm) were also used to capture images from the melt pool. The data was then analyzed to determine melt pool size, intensity, and shape to detect overheating and balling [31]. The Photodiode was also set up to discuss the plasma behavior of the melt pool. Okaro *et al.* [32] and Jayasinghe *et al.* [35] showed how three photodiodes' complex arrangements could monitor thermal radiation and plasma emission. The module was comprised of three photodiodes with 100 kHz sampling time. The first photodiode (700-1050 nm) was installed to detect plasma emission, the second photodiode (1080-1700 nm) was used to detect thermal radiation, and the third photodiode was placed to measure the intensity of the laser beam. Table 2-1 lists the wavelength and sampling time of photodiodes used in the literature. Also, Table 2-1 specifies any additional filters/lenses added to the in-situ monitoring system. This thesis uses the data of two commercial photodiodes placed in EOS M290 to identify lack-of-fusion pores. The integrated sensors' sampling frequency and wavelength ranges were 60 kHz and 750-900 nm, respectively.

Table 2-1: The sampling frequency and wavelength of photodiodes used in the LPBF studies, as well as any additional filters/lens

References	Wavelength (nm)	Sampling time (kHz)	Additional equipment	Machine
Kruth <i>et al.</i> [26] Berumen <i>et al.</i> [27]	400-1000	10	-	In-house
Gestel <i>et al.</i> [31]	350-1100	100	Amplifier 0-70 (dB)	In-house
Okaro <i>et al.</i> [32] Jayasinghe <i>et al.</i> [35]	700-1050 1080-1700	100	Focusing lens	Renishaw 500M

Egan <i>et al.</i> [33]				
Clijsters [29]	780–950	10 MHz	Optical filters	In-house
Craeghs <i>et al.</i> [30]	400-900	20	Optical filters	In-house
Demir <i>et al.</i> [11]	800-1700	1 MHz	Optical filters	In-house
Nadipalli [28]	400-1100 1200 - 1800	100	- Low-pass filters	In-house
Yadav [36]	NIR	100	Focus lens	SLM 280
Dunbar [37], [38]	520-530	100	520 and 530 band-pass filters	ProX 200
Bisht [25]	1150-1800	Unspecified	A 1150 nm high-pass filter	In-house
Artzt [39]	NIR	100	-	SLM 280

2.5.1.2 Mounting strategy

During the part qualification process, AM monitoring systems must document the build process and capture information. Two types of mounting strategies are used to set up sensors: “on-axial” and “off-axial” [40]. The on-axial sensor is placed in the optical path direction of the power source (laser), and data is transferred through the f- Θ lens, mirror, and beam splitter to the sensor. Figure 2-4 represents two set-up arrangements of the on-axial sensor.

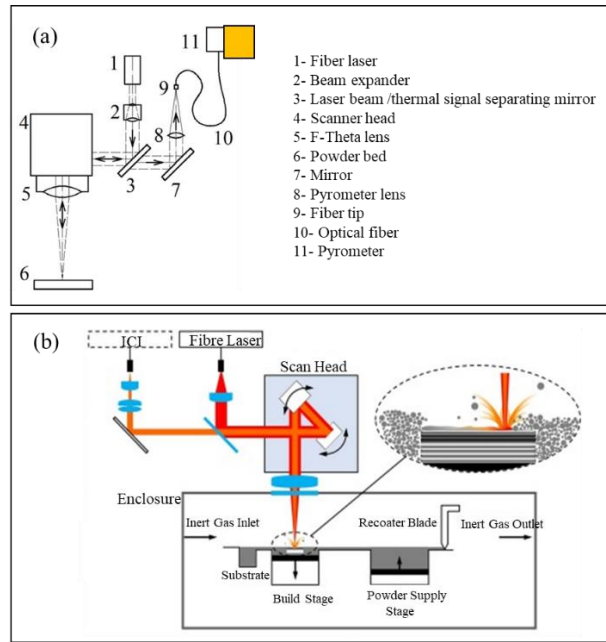


Figure 2-4: The on-axial position of (a) pyrometer (Source: Republished with permission of Elsevier, from [41]) and (b) ICI (Source: Republished with permission of Elsevier, from [42])

The off-axial sensor is installed outside the optical path with a given angle of view. Two different off-axial sensor mounting strategies are depicted in Figure 2-5.

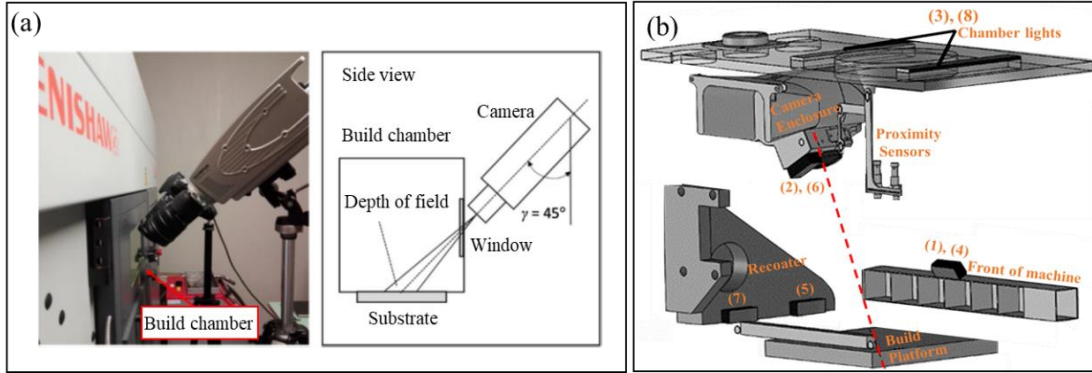


Figure 2-5: The off-axis position of (a) camera (Source: Republished with permission of Elsevier, from [43]) and (b) DLSR camera (Source: Republished with permission of Elsevier, from [44])

Figure 2-6 demonstrates the volume of papers associated with on-axial and off-axial sensor setup based on their type implemented in the LPBF system. According to Figure 2-6, the camera (visible to NIR and NIR to LWIR), pyrometer, and photodiode sensors have been installed both on-axially and off-axially. Based on the fundamental, optical inline coherence imaging was on-axially implemented, whereas X-ray imaging, fringe projection, scanner, acoustic, thermocouple, strain gauge, and displacement sensors were installed off-axially.

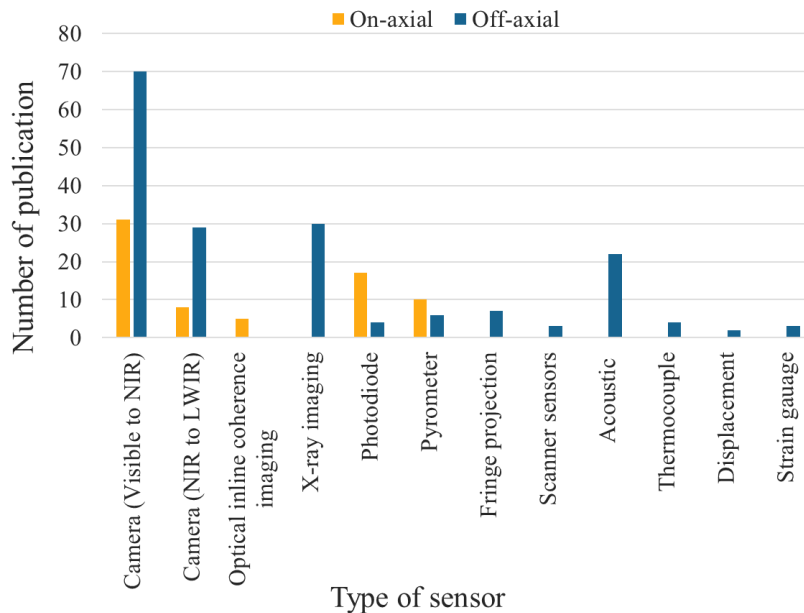


Figure 2-6: Relative emphasis of in-situ sensors arrangement based on their types reported in the literature using LPBF

Table 2-2 specifically categorizes different on-axial and off-axial photodiode arrangements to monitor the process signature used in the LPBF process.

Table 2-2: Mapping of the literature on in-situ photodiode of LPBF to monitor the process signature

On-axial sensor arrangement	Off-axial sensor arrangement
Abnormal process [32], [33] Geometry/Dimension accuracy [26], [27], [28] Overheating [29]–[31] Drift layer [36] Balling [31] Porosity [33], [34], [4] Density [35]	Emissivity [37] Geometry/Dimension accuracy [25], [28] Porosity [38]

2.5.1.3 Commercially available sensors

Although many vendors have installed sensor(s) on the LPBF machines, most of them are mainly designed to gather in-situ data that needs offline processing. As a result, to automatically generate an alarm or control the process, further developments are needed. Different developers of LPBF systems have offered process monitoring toolkits. Table 2-3 summarizes information on some of the commercial sensors mounted on the LPBF machine.

- EOS

EOS offers two modules to capture and analyze the data:

- 1) EOSTATE Meltpool Monitoring, which includes on-axial and off-axial photodiodes. Both sensors measure the light intensity emitted from the melt pool with a 60 kHz sampling frequency. After the process, the data can be analyzed using the EOSTATE monitoring software to find the intensity signal disturbance. Melt pool monitoring data is very sensitive to deviations resulting from power fluctuations. This software is used to analyze the light intensity signal in this study (0).
- 2) EOSTATE Exposure Optical Tomography includes an integrated camera to capture powder beds' images. The camera uniformly captures images in the near-infrared spectral range and with a resolution of 2560×2160 pixels. Then, the images are correlated with thermal radiation. Analyzing the correlated data is provided in the EOSTATE Exposure OT software to identify any thermal deviation. Exposure OT is more sensitive to scanning speed and hatching distance deviations [45].

- SLM Solution

SLM solution offers two toolkits to monitor the melt pool and laser power:

- 1) Melt pool monitoring (MPM) includes an on-axial pyrometer to measure thermal radiation from the melt pool at a rate of up to 100,000 times per second [46].
- 2) Laser power monitoring (LPM) is recorded as the actual emitted laser output at a rate of 100,000 times per second. The laser output is measured by uncoupling the laser beam in the optical path and reflecting it to a sensor [47].

- GE Additive (Concept Laser)

The Company offers two separate modules to collect data from the melt pool:

- 1) QM melt pool 3D module is a monitoring tool with an on-axial monitoring setup of the photodiode to estimate the melt pool area and intensity. This system provides two kinds of data. The first data set is the average intensity of the component after completing the print, and another one generates a 3D dataset of the part and its structure. This information is accessible after the process, and there is not currently used for defect correction and feedback control [48].
- 2) QM coating focus on the dose factor. That is the control amount of the powder released by the powder hopper before the recoating system. This factor depends on the sufficient powder released before the recoating operation [49].

- Renishaw

InfiniAM has been offered by Renishaw to monitor the energy input and melt pool emission. This module provides information about melt pool characteristics in high temporal resolution to provide a 2D and 3D view of the build [50].

- Trumpf

Truprint consists of a high-resolution camera to monitor melt pool, powder bed, and part geometry. The integrated camera captures powder bed images layer-by-layer. Image analysis modules are also provided, and comprehensive analysis of each layer can be performed and compared with the CAD model.

- B6 Sigma, Inc.

B6 Sigma has developed the PrintRite3D that includes Sensorpak, a set of on-axial and off-axial sensors. A software called “Inspect” to determine quality metrics and identify suspicious patterns layer-by-layer. A software called “Contour” for real-time monitoring and reconstruction of the part geometry and a module to compare the result with the CAD model.

Table 2-3: Some commercial sensors mounted on the LPBF machines

Developer	Module Name	In-situ sensor	Monitored items
EOS	EOSTATE Meltpool	Two photodiodes	Melt pool
	EOSTATE Exposure OT	Camera	Powder bed thermal map
SLM solution	Melt pool monitoring	Pyrometer	Melt pool
	Layer control system	Camera	Powder bed
GE Additive (Concept Laser)	QM melt pool 3D	Photodiode	Melt pool (area and intensity)
Renishaw	InfiniAM	Photodiode	Melt pool
Trumpf	Truprint Monitoring	Camera	Powder bed and part geometry
B6 Sigma	PrintRite3D	photodiode pyrometer	Different monitoring possibilities

2.5.2 Monitoring techniques

Achieving the excellent quality of metallic AM parts is a challenging task due to the high complexity of the physical phenomena and the lack of high fidelity and high-speed mathematical and statistical models. To address some of these challenges, much emphasis has been recently placed on the monitoring of AM processes to shed some light on the process dynamics and signatures [26], [27], [29], [51]–[54]. The monitoring techniques will be categorized into statistical and machine learning techniques. However, those methods that have been used to detect porosity will be discussed here in Sections 2.5.2.1 and 2.5.2.2.

2.5.2.1 Statistical techniques for the detection of porosity

After collecting in-situ data, the sensor's data should be processed/conditioned and analyzed to extract the desired information. Different signal conditioning and statistical methods are discussed in the literature to monitor the AM processes effectively. However, those methods used to detect porosity will be discussed in this section.

Image grabbing from the process and image segmentation method was used to detect porosity in LPBF. Foster *et al.* [55] and Abdelrahman *et al.* [56] showed how the image segmentation method could help to detect porosity. They mounted the DSLR camera and

several flash modules inside the EOS M280 build chamber to provide high image contrast. The camera was captured images from the manufacturing of samples printed with a variation of print parameters to create a lack-of-fusion. Foster applied Image processing and 3D X-ray scan to correlate the results with the CT-scan data. [55]. Although the detail of the image segmentation method was not disclosed, the study showed the potential of the technique to detect defects. Abdelrahman *et al.* has another approach in which images were cut and normalized to compare harmonized ones, and the level set segment method was applied as represented in Figure 2-7 [56]. The identification of 28 artificial defects was correlated by a CT scan using a confusion matrix. Although the accuracy of the matrix showed a high level of the true positive rate, the false-positive rate was also too high.

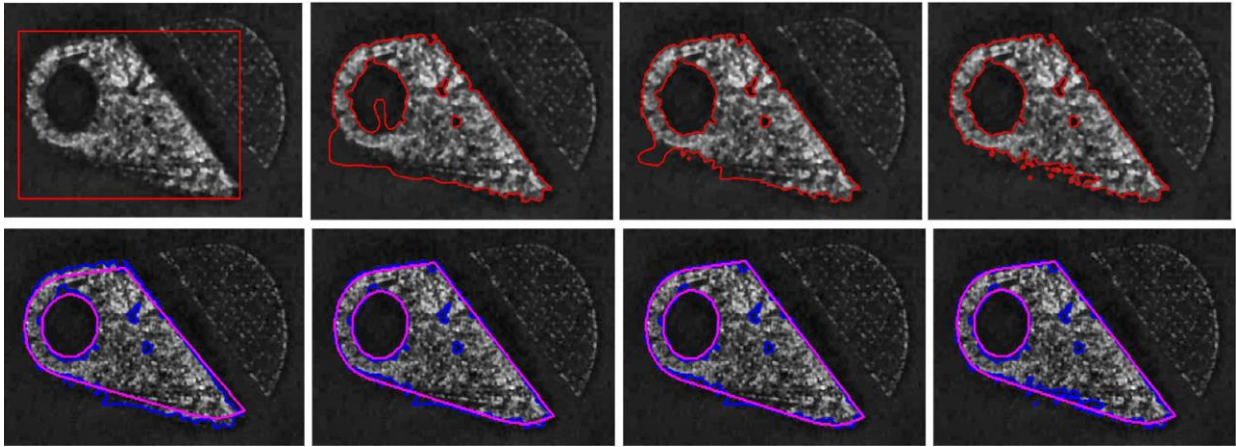


Figure 2-7: The procedure of segmentation method from initialization (first row) to the final map (second row) (Source: Republished with permission of Elsevier, from [56])

One of the emerging technology for pore detection in LPBF is a commercialized system developed by the MTU Aero Engines team [57]–[59]. They used an sCMOS camera system with a 5 Megapixels detector. The integrated sensor captures 10 frames per second. Then, all 10 capture images are combined into one single image. In the next step, the final image is correlated with the light emitted from the process. However, the emitted light is a combination of three sources (laser radiation, thermal emission, and plasma emission), as shown in Figure 2-8, so a band-pass filter was also used to filter out the laser reflection and plasma emissions from thermal radiation. Then the derived thermal signal can be used to identify its deviation. Any thermal deviation is interpreted as a potential defect in the final printed part. The final data is a layer-by-layer exposure image in which cold and hot spots correspond

to the nominal and abnormal areas with a resolution of $0.1 \text{ mm} \times 0.1 \text{ mm}$ [59], as shown in Figure 2-8. This technique is used in the EOS Exposure OT [45].

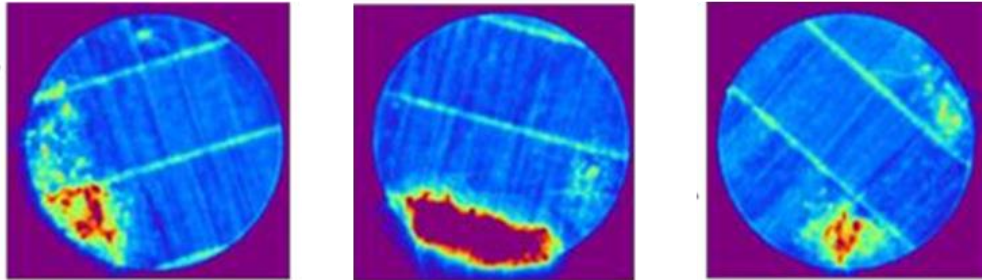


Figure 2-8: Three Layer-wise Optical Tomography (OT) images used in LPBF (Source: Republished with permission of AIP Publishing, from [57])

This technique is correlated to micro-computed tomography [58] and digital radiography [59] to identify a lack-of-fusion. Signal/data conditioning and methodologies for detection of crack and delamination.

2.5.2.2 Machine learning technique to detect porosity

Machine learning is an application of artificial intelligence (AI), providing the opportunity to learn from processes and then predict the processes through data patterns. The learning process is included in data acquisition and pattern recognition. The machine learning methods can predict the formation of flaws in real-time from LPBF due to their fast processing. Machine learning algorithms can be classified into three main groups: 1) supervised learning, 2) unsupervised learning, and 3) reinforcement learning. These methods include several sub-techniques, and some of them are used in AM quality assurance platforms. Although unsupervised and reinforcement learnings were applied on many metal AM processes to detect pores, only supervised learning has been applied to identify porosity in LPBF. The supervised learning algorithm is trained with a labeled dataset in which each input feature X is labeled with an output Y . By knowing the input and output datasets, the model is trained to identify the relationship between input and output variables. Supervised learning can solve two types of problems: classification and regression. Classification maps the function from the input to discrete output; however, the regression model is a predictive model to estimate continuous output. In the following sections, the applications of classification and regression models to detect porosity generated during the LPBF process are listed in Table 2-4.

Table 2-4: Machine learning techniques applied in LPBF to detect porosity

	Method	References
Classification	SVM	[44], [25], [62], [63], [61]
	MLP	[60], [61], [64], [65]
	CNN	[66], [67], [68], [64], [69]
	SNN	[67]
	Conditional Autoencoder	[69]
	DSCNN	[66]
	KNN	[61], [63]
Regression	GP	[70]
	NN	[71]

- Classification

In the classification method, the ultimate goal is to predict output labels based on the dataset's previous observation. Various classification methods are proposed to evaluate prediction performance; however, the most common way is to calculate the accuracy. The accuracy is the percentage of correct classification out of all predictions. Table 2-4 lists the recent classification applications in metal AM. According to Table 2-4, support vector machine (SVM), neural network (NN), and K-nearest neighbors (KNN) were applied in LPBF to detect porosity.

Scime *et al.* [62], Gobert *et al.* [44], Nadipalli *et al.* [25], Mahmoudi *et al.* [63], and Imani *et al.* [61] applied SVM to identify defects by analyzing in-situ images. For example, Scime *et al.* [62] analyzed the images from the melt pool of In718 fabricating by EOS M290. A SIFT feature technique was calculated to extract the input images based on the 36 process parameter combinations to produce one of the desirable, balling, severe keyholing, keyholing porosity, or under-melting using qualitative and quantitative measures. The images were then converted into a standard vector format or HoG under three different contrast adjustments. The images were scaled using gamma values 7 of 1 (no change), 0.75 (decreased contrast), and 10 (increased contrast) since each feature is more visible in specific contrast. The final fingerprint consisted of nine different segments to describe the gradient fields under different contrast adjustments and different melt pool regions. In the next step, t-distributed Stochastic Neighbor Embedding was used to reduce data dimension, and multi-class SVM was applied to classify input. 85.1% was reported for 10-fold cross-validation to support the feasibility of the SVM algorithm [62].

In the study of Kwon *et al.* [72], Zhang *et al.* [73], Caggiano *et al.* [68], and Shevchik *et al.* [67], the CNN was used to predict porosity created by changing print parameters. For instance, Kwon *et al.* [72] created randomized defects by changing laser power during the fabrication of seven SUS316L specimens using WINFORSYS. Under six conditions of laser power 50, 100, 150, 200, 250, 300, and

350 W, images were captured with the framerate of 2.5 kHz. After clipping and de-noising, the images were randomly used to train, validate, and test the CNN for classifying melt pool images. By dropping the number of nodes and increasing the layer number, even the images with blurred edges were achieved satisfactory results. The model had a weak performance on the Leave-one-out evaluation; however, the algorithm can find abnormal processes by simultaneous classification of various shapes. Ertay *et al.* [69] and Shevchik *et al.* [67] compared the result of CNN with other types of DNN, whereas Snow *et al.* [64] used a hybrid neural network. Ertay *et al.* [69] compared CNN and CVAE (Conditional Variational AutoEncoder) that were trained based on melt pool physics and CT-scan data. Thus, in Ertay's study in-situ sensor was not used. Shevchik *et al.* [67] compared CNN with SCNN. A fiber Bragg grating (FBG) sensor was used to capture acoustic data. The sensor was on-axially installed on Concept M2 at a distance of 20 cm away from the melt pool. In addition, the cubical sample with CL20ES stainless steel powder was printed by changing scan speed (50, 79, and 132 J/mm³) to provide three levels of energy input. In the Snow's study [64], NN and CNN models were used to identify lack-of-fusion defect. First, a 36.3-megapixel DSLR camera (Nikon D800E) and various lightening conditions were placed on a commercial 3DSystems ProX 320 from virgin Ti-6Al-4V to capture six images M1-M6 (three images after post-recoat and three images after post-scan) from 81 cylindrical coupons. The captured images from 20 coupon samples (individually and in the form of dimensional tiles) were selected and labeled by XCT using a custom automated defect recognition (ADR) algorithm [44], [60] as nominal and anomaly and fed into series of NN and CNNs models. In the beginning, each model was trained separately, and results were compared through a confusion matrix demonstrating that the CNN accuracies ranged from 69–78%, and the NN accuracies ranged from 56–66%. Then, to increase the accuracy, another technique was proposed by feeding the SoftMax outputs from CNNs and NNs to train data into another shallow neural network with five neurons in one hidden layer. The new approach resulted in an accuracy of 93.5%. Another build was fabricated to test the model, which showed an accuracy of 87.3% [64].

Another classification algorithm that was applied in LPBF is KNN. Although the KNN algorithm is easy to implement, finding the optimum k is one challenge. Besides, the accuracy of the algorithm depends on the scale, dimension, and quality of data. KNN classification method is not commonly used in the AM process. Imani *et al.* [61] applied KNN to compare its result with other ML methods. The result of KNN prediction was compared with the result of SVM and FFNN, which showed that KNN had poor performance.

- Regression

The regression model predicts the mathematical equation to map the input (x) variable to the output (y) variable. The regression model can solve many problems with discrete input, multi-input, and time-series input variables. The performance of the regression model is mostly evaluated by Mean Squared Error (MSE) and Root Mean Square Error (RMSE). Many types of regression models are proposed according to the number of input data, the shape of the regression line, and the input variable type. According to Table 2-4, the Gaussian process (GP) and neural network (NN) are regression models applied in LPBF.

The Gaussian process (GP) is used to detect porosity in the study of Tapia *et al.* [70]. Tapia *et al.* applied the GP model on experimental data to predict melt pool depth in single-track experiments [74] and porosity [70]. A simulation model was developed using a 26 training dataset, creating a variation on the process parameters (laser power, scan speed, and laser beam size combination). The GP prediction was made over processing parameters, as depicted in Figure 2-9, which showed the mean value and standard deviation of the prediction. The standard deviation value indicated less than 20 μm for most of the points; however, areas with higher STD are attributed to extrapolation. Then, the model was validated using a low mean absolute predictive error $\text{MAPE} \approx 6 \mu\text{m}$.

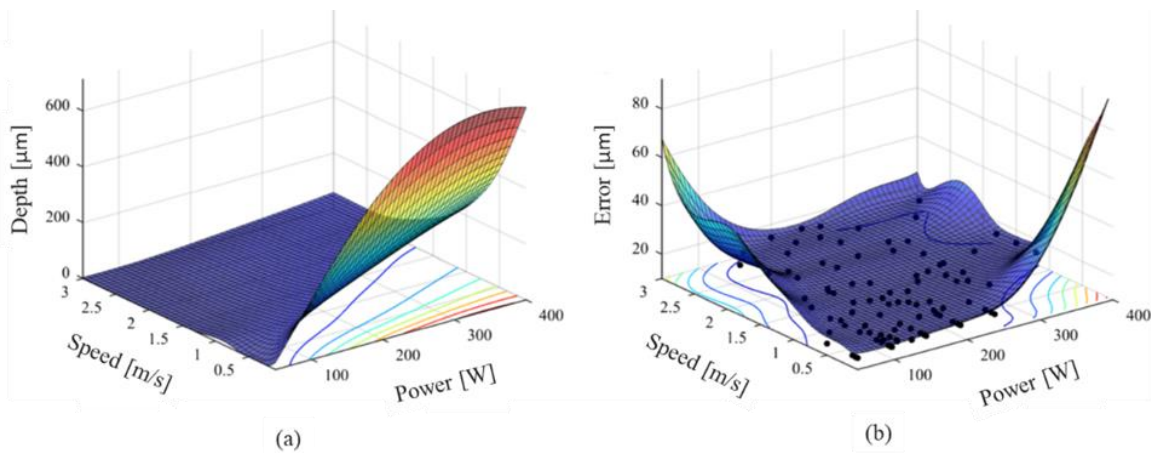


Figure 2-9: (a) Mean value and (b) standard deviation of the GP prediction over the processing parameters; black dots represent the locations of the training data points showing very low values of the standard deviation. (Source: Republished with permission of Springer Nature, from [74])

The result represented promising performance in a noisy environment. In another study, Tapia *et al.* discussed the use of GP to calibrate a convenient criterion to avoid keyhole porous [70].

The neural network also can use as a regression model to estimate continuous output. The NN regression model can be used to predict the flaws happening in the LPBF process. Williams *et al.* [71] applied the image-modality-to-image modality regression model to predict the flaws happening in the process. In the study, Spatially Resolved Acoustic Spectroscopy (SRAS) [75] was used to monitor acoustic frequency from the building of ten samples. These samples were printed by:

- i. Titanium (Ti-6Al-4V) using Renishaw AM250 machine,
- ii. Nickel alloys (CM247-LC) using ReaLizer SLM50 machine, and
- iii. Titanium alloy contaminated by tungsten using ReaLizer SLM50 machine.

The SRAS characteristics were then extracted using the Fourier transform. SRAS information (input) and optical micrograph (output) were fed into a DCB-MIR network, which is a type of fully convolutional block densely connected network and builds upon ResNet [76] and (DenseNet) [77] models. The similarity between the proposed model and optical micrograph was evaluated using cosine similarity. This criterion notified the progress in detecting the size and location of defects, especially lack-of-fusion and scratches; however, some of the prominent pores were not identified because of the limited number of input samples.

2.6 Summary

In this chapter, the laser powder-bed fusion (LPBF) process was explained, and the importance of quality assurance was discussed. Also, in-situ sensors installed in the LPBF system were discussed, which are categorized into two groups: (i) radiative and (ii) non-radiative. Besides, two types of installation to mount sensors in the LPBF system were reviewed. In-situ sensors are installed to capture information during the fabrication of parts. Afterward, the sensor's data is analyzed to identify the formation of defects. Thus, the statistical and machine learning algorithms were explained to detect porosities created in printed parts.

Chapter 3. Development of a defect-detection platform using photodiodes signals collected from the melt pool of laser powder-bed fusion

3.1 Abstract

The focus of this chapter is to highlight the systematic implementation of three analytical methods, including Absolute Limits (AL), Signal Dynamics (SD), and Short-Term Fluctuation (STF) algorithms on the datasets collected from a photodiode-based monitoring setup for in-process identification of porosity formed due to the lack-of-fusion (LoF) phenomenon. In this systematic approach, the defects are artificially designed and embedded in the coupon samples to resemble the formation of LoF pores in parts composed of Hastelloy-X. Then, the effectiveness of algorithms (AL, SD, and STF) is investigated. These algorithms are applied to understand the impact of artificial defects on the light intensity collected by on-axial and off-axial photodiodes to detect the LoF pores. The image processing algorithm is then applied to analyze the output of the software. Then, through the model developed for detecting artificial defects, randomized defects are detected to explore the impact of variation in print parameters on the detection of defects. On the other hand, the actual geometrical feature and position of defects are identified through post-processing computed tomography (CT) scanning. Then, the segmentation method and volumetric approach are used to examine the correlation between the results of the defect detection algorithm and CT-scan.

3.2 Methodologies and Experimental Setups

3.2.1 Design of experiments and process parameters

Two sets of design of experiments (DoE), including cubical samples with a size of $8 \times 8 \times 10$ (W \times L \times H) mm, were devised and labeled as R-series (Figure 3-1. a) and T-series (Figure 3-1. b). In the design of the R-series, the effect of LoF was mimicked by embedding artificial voids in the samples, as shown in Figure 3-2. Two different void geometries of cylindrical (R2, R3, and R5) and spherical (R4) shapes with different sizes were fabricated using the EOS-M290 LPBF machine. One control sample (R1) without any artificial void was also printed. To study the pores' distribution, voids were distributed at different vertical positions with respect to the build plate and different print layers location (R5, shown in Figure 3-2.d). Additionally, three samples (R6, R7, and R8) with a similar design to R2 were included in the first set of DoEs, but they were printed with different process parameters, as highlighted in Table

3-1. This arrangement will combine artificial voids and process parameter deviation on the signal intensity and stability. The print parameters listed in Table 3-1 were selected according to the print parameters used to obtain high-quality Hastelloy-X [EOS Nickel Alloy HX, Krailling, Germany] parts [78]. Each sample was printed eight times at different locations of the build plate with respect to the direction of the gas flow and the re-coater (Figure 3-3. a). In the design of each sample, vertical and horizontal grooves were added for registering the location of porosities in the CT scan datasets (Figure 3-1).

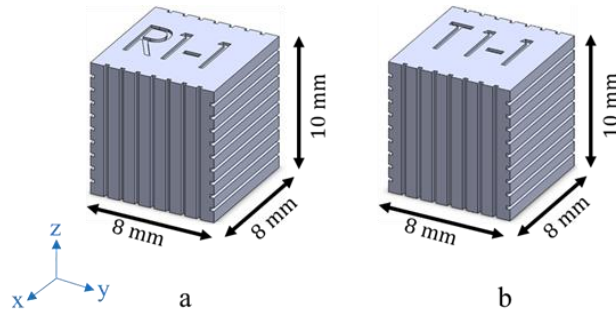


Figure 3-1: CAD model of reference samples: a) series R b) series T.

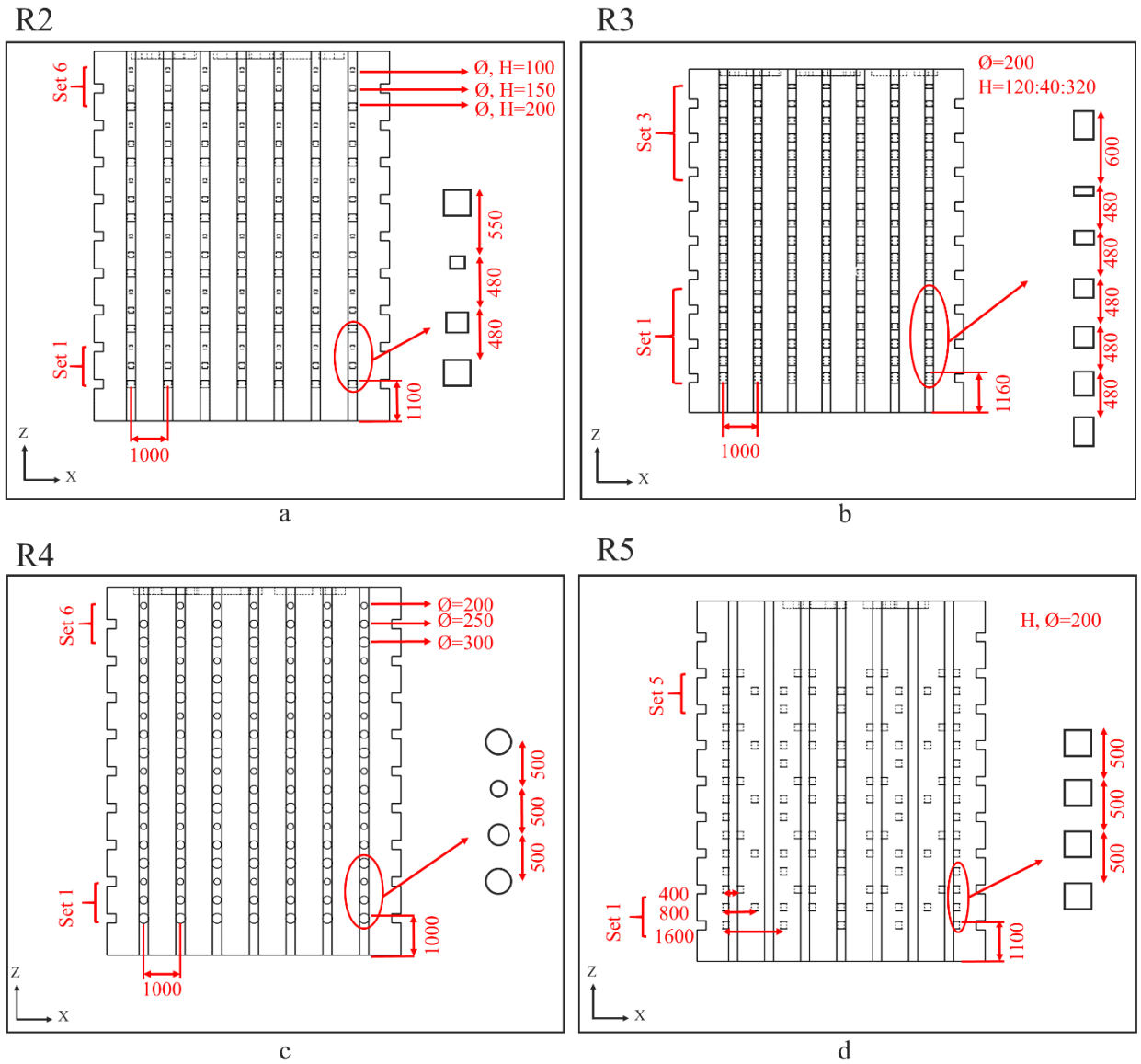


Figure 3-2: 2D cross-sections of samples showing the distribution of the artificial voids in samples: a) R2 which includes 6 similar sets of three sizes of defects (\varnothing , $H=200 \mu\text{m}$, \varnothing , $H=150 \mu\text{m}$, and \varnothing , $H=100 \mu\text{m}$), b) R3 which is including 3 similar sets of six sizes of defects (the diameter: $\varnothing =320 \mu\text{m}$, $\varnothing =280 \mu\text{m}$, $\varnothing =240 \mu\text{m}$, $\varnothing =200 \mu\text{m}$, $\varnothing =160 \mu\text{m}$, and $\varnothing =120 \mu\text{m}$ and the height: $H=200 \mu\text{m}$), c) R4 which is including 6 similar sets of three sizes of defects ($\varnothing =300 \mu\text{m}$, $\varnothing =250 \mu\text{m}$, and $\varnothing =200 \mu\text{m}$), and d) R5 which is including 5 similar sets of one size of the defect (\varnothing , $H=200 \mu\text{m}$) printed in 3 scenarios of distribution (5×5 , 9×9 , and 8×8). \varnothing is diameter and H is height, both in μm .

Table 3-1: Types and print parameters in print 1: 8 samples printed in 6 locations.

Sample #	Type of artificial voids	Power (watt)	Hatching Distance (μm)	Speed (mm/sec)
R1	Standard (no artificial voids)	200	90	1000
R2	Cylindrical voids	200	90	1000
R3	Cylindrical voids	200	90	1000
R4	Spherical voids	200	90	1000
R5	Cylindrical voids	200	90	1000
R6	Cylindrical voids at the different laser power	100	90	1000
R7	Cylindrical voids with the different hatching distance	200	150	1000
R8	Cylindrical voids with the different scanning speed	200	90	1500

In T-series, the samples were designed and printed by only varying print parameters to create randomized and stochastic voids produced by LoF. The geometry of these samples was similar to R1, and the print parameters for each one are listed in Table 3-2. Six samples from each design were labeled and arranged on the build plate (Figure 3-3. b). Additionally, in all samples (R-series and T-series), the stripe scan strategy with 67° rotation after each layer was used; but, the down-skin scan strategy (process parameters are similar to the core) was used around voids embedded in samples R2- R8. It should be noted that the data collected for this study only entails the layer that cap the defect, and for these “capping layers”, no down-skin strategy is used. Also, the 4σ spot diameter of the laser beam was 100 μm (0.004 in), where the laser used was a 400 W Yb-fiber setup.

Table 3-2: Types and print parameters in print 2: 4x6 samples.

Sample #	Type of variation	Power (watt)	Hatching distance (μm)	Speed (mm/sec)
T1	Standard	200	90	1000
T2	Power	100	90	1000
T3	Hatching distance	200	150	1000
T4	Speed	200	90	1500

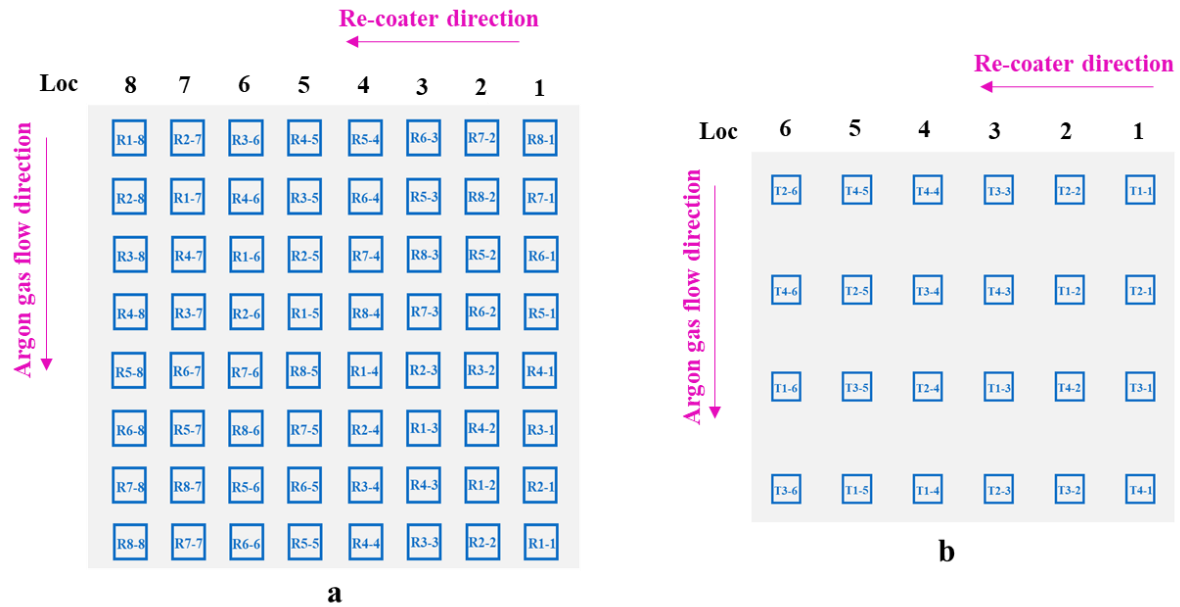


Figure 3-3: Samples layout on the build plate: a) R series; b) T series.

3.2.2 In-situ monitoring devices

The integrated sensors in the used EOS M290 setup are two photodiodes with a 60 kHz sampling frequency. On-axial and off-axial photo-diodes capture light intensity signals from the melt pool in the wavelength range of 750-900 nm. The on-axial photodiode is aligned with the laser beam path through a beam splitter, and the off-axial is fixed and mounted on the roof of the building chamber. The photodiodes collect light intensity in the visible and near-infrared ranges emitted from the melt pool [29]–[31], [79], as shown in Figure 3-4. In addition to the light intensity data, laser modulation and X/Y scanner position are recorded and stored in the associated PC.

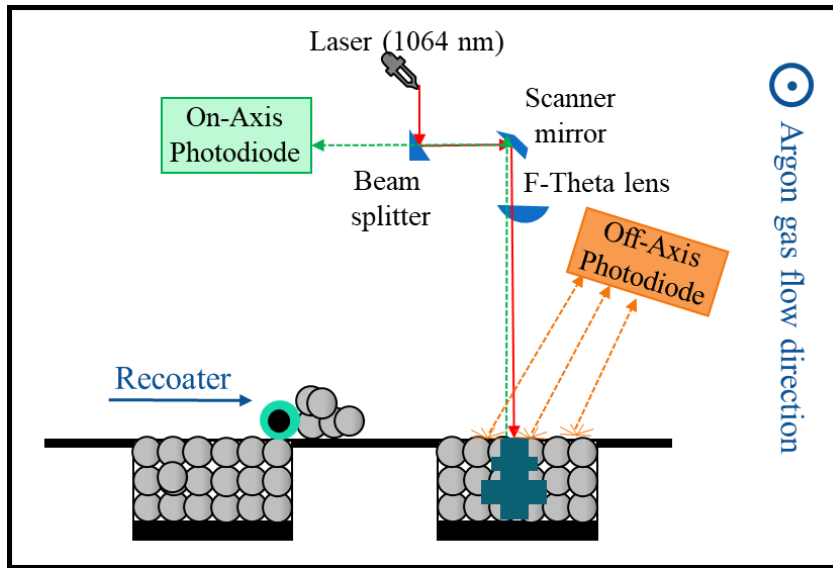


Figure 3-4: Schematic of LPBF equipped with on-axis and off-axis photodiodes.

Intensity and geometry corrections of both on-axis and off-axis photodiodes datasets are required. The intensity correction for the on-axis data should be implemented due to the chromatic aberration phenomenon. It is initiated because the wavelength of light intensity recorded by the photodiode is not the same as the wavelength optimized for the scanner mirror and f-theta lens. In contrast, because the off-axis photodiode is not on the platform's center, it gathers intensity signals from different angles and distances. The geometric correction is needed to be calculated before the print to find the platform's absolute position due to the image distortion caused by the F-theta lens and scanner mirror [45]. It should be noted that the monitoring process is designed and provided by the vendor. Additionally, intensity and geometry corrections are also implemented by the OEM's monitoring system.

3.2.3 Analysis of the data collected by in-situ monitoring

In-situ data is analyzed by two phases: 1) EOSTATE software 2) image processing and statistical analysis. The EOSTATE software is designed to analyze the photodiode signal to identify the location of fluctuation in the final part. By the software, the in-situ data is analyzed, and the result of the analysis is exported as a greyscale TIFF image per layer. TIFF images show the nominal (greyscale) and abnormal (yellow pixel which is the default of software) points of the printed part. Each pixel in the TIFF image is representing the average value of the intensity signal in the area of $5.55 \times 5.55 \mu m^2$. In

the second phase, TIFF images are then analyzed through the segmentation method and correlated with CT-scan analysis. In the following paragraphs, each step is explained in detail.

The schematic of signals and detection method is shown in Figure 3-5. Figure 3-5.a demonstrates the data collection process. After the print, data is accessible for analysis using commercial EOSTATE Meltpool Monitoring software [EOS GmbH, Krailing, Germany]. The collected data are imported to EOSTATE software.

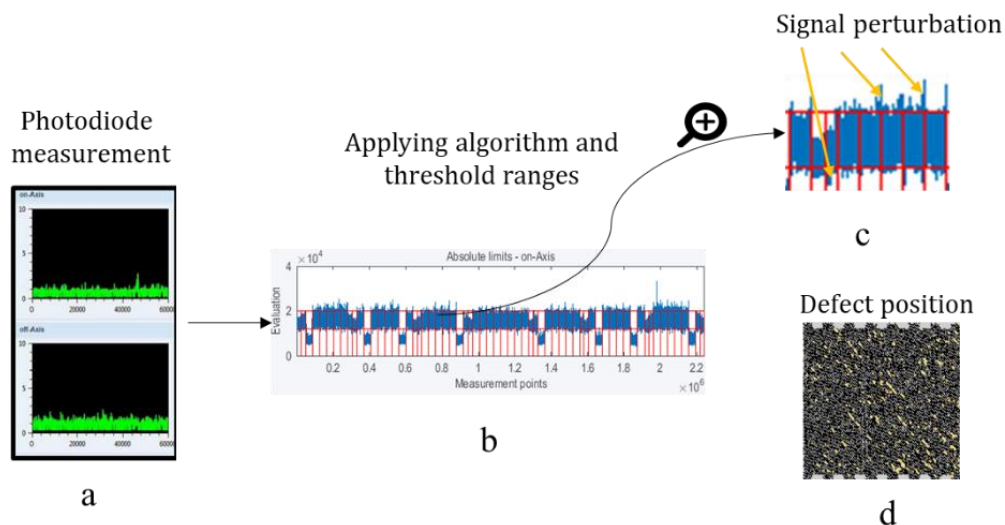


Figure 3-5: Schematic of a) photodiode data collection, b) applying one of the algorithms and tuning threshold ranges, c) magnifying part of the signal to show signal perturbation, and d) one layer of the sample included yellow pixels which are corresponding to the location of signal perturbation.

In the next step (Figure 3-5.b), data processing algorithms are applied. Three algorithms are incorporated into the software: Absolute Limits (AL), Signal Dynamics (SD), and Short Term Fluctuations (STF) [45]. These algorithms are designed to detect specific process phenomena that might affect the quality of the printed part such as sudden laser power variation, gas flow issues, and short instabilities. The central feature of all of the algorithms is the moving average [45]. Specifically, the Absolute Limits algorithm is developed to apply the moving average on the light intensity signal. The Signal Dynamics algorithm can calculate the signal disturbance in which each measured point will be compared to the mean value. This characteristic is also filtered by the moving average. The Short-Term Fluctuations is a moving average with a longer filter length. To analyze the dataset a threshold range

should be defined for each algorithm. The threshold range of Absolute Limits and Signal Dynamics algorithms are defined directly by users; however, the threshold bands of Short-Term Fluctuations algorithm are calculated based on the given upper and lower level of moving average signal (e.g. 80% to 120% of moving average signal). The schematic of each algorithm is presented in Figure 3-6. Additionally, the window size/length of moving average should be chosen for each algorithm by a user.

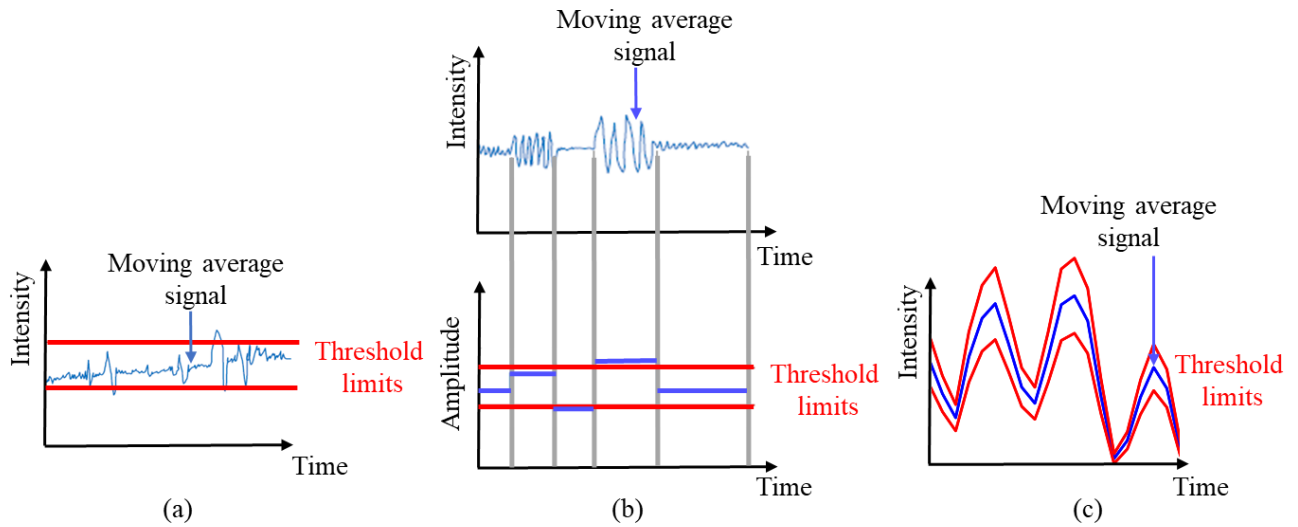


Figure 3-6: Schematic of a) Absolute Limits (AL), b) Signal Dynamics (SD), and c) Short Term Fluctuations (STF) after applying the threshold.

By applying the algorithm and threshold ranges (Figure 3-5. b), some parts of the signals might exist outside the threshold ranges. Any signal higher than the up-level threshold and lower than the down-level threshold is defined as a signal perturbation (Figure 3-5. c). Signal perturbation is visualized as a yellow pixel in a TIFF image which is corresponding to one layer of the printed part. The yellow pixel may be corresponding to the location of defects in the last TIFF images (Figure 3-5.d). As a result, the output of the software is one TIFF image per layer which could be exported for offline analysis.

The results of deploying the three algorithms were investigated on the on-axial and off-axial photodiodes data. A data screening procedure was pursued when the following ranges of threshold and the different number of window lengths for the moving average window were selected:

- 1) Absolute Limits: Threshold 10000-22000 and window length 5-30
- 2) Signal Dynamics: Threshold of 20-1000 and window length 5-30, and,

3) Short Term Fluctuations: Threshold 65-140 and window length 5-20.

It should be noted that the threshold range is normalized values based on the light intensity. From observing the results of this step, each threshold was narrowed down to a smaller band to highlight the effect of the artificial defect. The range of window length (5-30) was optimized by observing results after applying them and by matching the location of indications/yellow pixels and artificial defects.

After the screening phase, the following narrower ranges were chosen for the analysis step:

- 1) Absolute Limits with the threshold range of 12000-20000 and window length of 10,
- 2) Signal Dynamics with the threshold range of 50-800 and window length of 15, and
- 3) Short Term Fluctuations with the threshold range of 75-135 and window length of 16.

The analysis was performed on the layers that include the artificial defects followed by five successive layers (200 μm) printed on the top of that, as demonstrated in Figure 3-7b, Figure 3-7c, and Figure 3-7d for three sizes of cubical voids in sample R2. The result of sample R2 (defect radius=200 μm and defect height=200 μm) is shown in Table 3-3 to show the example of comparison among algorithms on on-axial and off-axial signals.

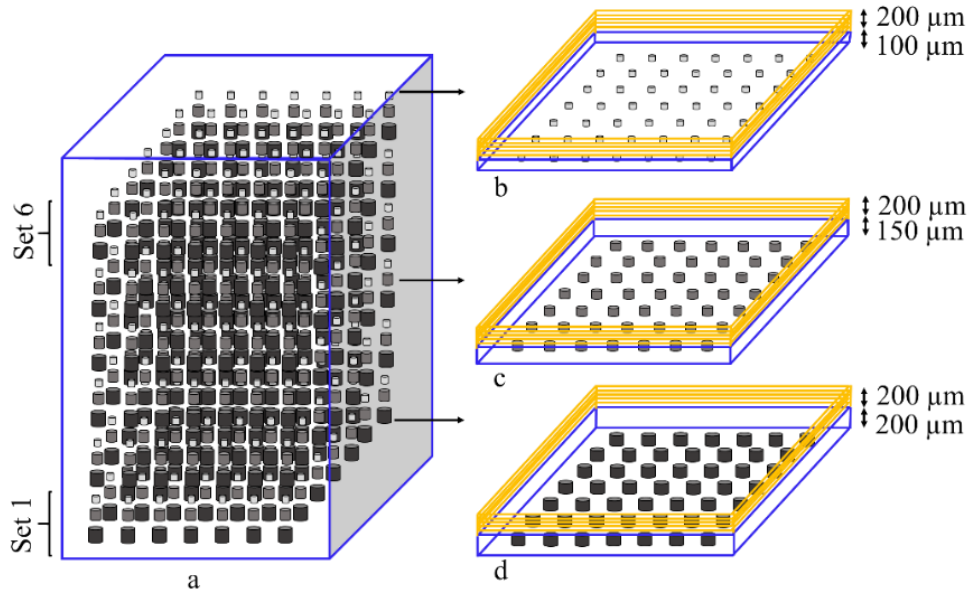
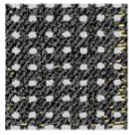
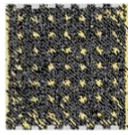


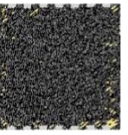
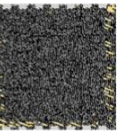
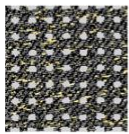
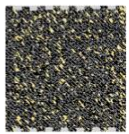
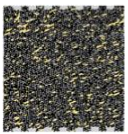
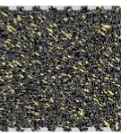
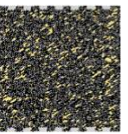
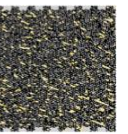
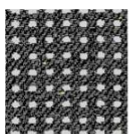


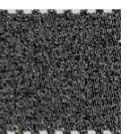
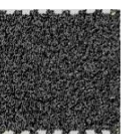
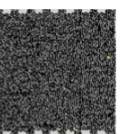



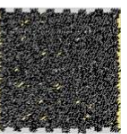
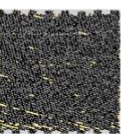
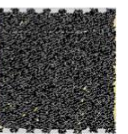
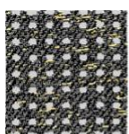
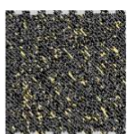

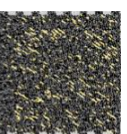
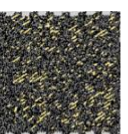
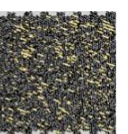



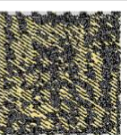
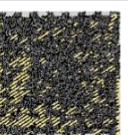
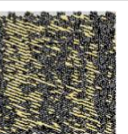


Figure 3-7: Schematic of a) sample R2 included artificial voids and five successive layers on top of the artificial voids with radius and height of b) 100 μm , c) 150 μm , and d) 200 μm .

Table 3-3: Applying the detection algorithms on the five consecutive layers after the defect (Layer 0: last layer of the international defect) (sample R2, defect radius= 200 μ m and defect height=200 μ m).

	Algorithm	Layer 0	Layer 1	Layer 2	Layer 3	Layer 4	Layer 5
On-axial photodiode	Absolute Limits						
	Signal Dynamics						
	Short Term Fluctuations						
Off-axial photodiode	Absolute Limits						
	Signal Dynamics						
	Short Term Fluctuations						

The results demonstrate a high signal fluctuation in layer 1 and layer 2 in the artificial defect zones (see yellow pixels corresponding to the artificial defects in Table 3-3). The matching result between the location of artificial defects and yellow pixels indicates that the AL algorithm, applied to both photodiodes' datasets, can effectively identify the location of defects. Furthermore, the STF algorithm applied to the on-axial photodiode dataset may identify the location of defects; however less amount of yellow pixels are found in the artificial defect zone. Besides, the STF algorithm could not identify all of the artificial defect (demonstrated in Table 3-3 column: layer1 and row On-axial STF). In addition,

yellow pixels after applying SD are not relevant to defect position. According to the results shown in Table 3-3, the AL seems to be a more suitable approach for detecting the location and size of artificial defects added to the part. Additionally, AL could minimize the irrelevant yellow pixels to defect positions which are shown after applying SD on the on-axial and off-axial signal and STF on the off-axial signal. However, by applying AL on the on-axial and off-axial signals, the on-axial signal highlights more fluctuation on the signal and better defect detection, as shown in Table 3-4. Table 3-4 shows layer 1 (printed on top of the artificial voids) for sample R2 in different positions of the build plate. Analyzing the results confirms that the application of the AL algorithm on the off-axial photodiode signal results in a fewer yellow indicators than the on-axial photodiode signal. Also, in some locations like R2-7, all defects are not identified through the off-axial photodiode signal. As a result, the on-axial photodiode datasets were selected for further analysis in this study.

Table 3-4: Applying the AL algorithm to the datasets collected by on-axial and off-axial photodiodes on layer 1 based on the explanation in Table 3-3 (sample R2, defect radius= 200 μ m and defect height=200 μ m)

Photodiode	R2-1 Layer 1	R2-2 Layer 1	R2-3 Layer 1	R2-4 Layer 1	R2-5 Layer 1	R2-6 Layer 1	R2-7 Layer 1	R2-8 Layer 1
On-axial								
Off-axial								

In the next phase, an image processing algorithm should be conducted to evaluate the performance of the algorithm.

3.2.4 Image processing algorithm

After applying the AL algorithm on the on-axial signal, the generated images were analyzed. In the first step, less than three adjacent yellow pixels were considered as noise, and more than three adjacent yellow pixels were taken into account in the next step of the analysis. In the next step, the images were segmented into areas of interest around each artificial defect using MATLAB (Figure 3-8b). The center of each circular area is located in the center of each defect. Besides, in the samples with cylindrical defects (R2, R3, R5, R6, R7, and R8), the radius of area of interest (AOI) around the artificial defect is

chosen the same as the radius of artificial defects proposed in the design file. In the sample with the spherical defects (R4), the radius of AOI is equal to the radius of the spherical defect. The following pixel numbers were considered in Table 3-5:

Table 3-5: Number of pixels per radius of each circular area for each sample with different defect size (each pixel is representing the average value of intensity signal in the area of 5.55×5.55 ($\mu\text{m} \times \mu\text{m}$)).

Sample	Defect radius (μm)	Number of Pixel per radius of the circular area
R2, R6, R7, and R8	100	28
	150	31
	200	36
R3	200	36
R4	200	36
	250	40
	300	45
R5	200	36

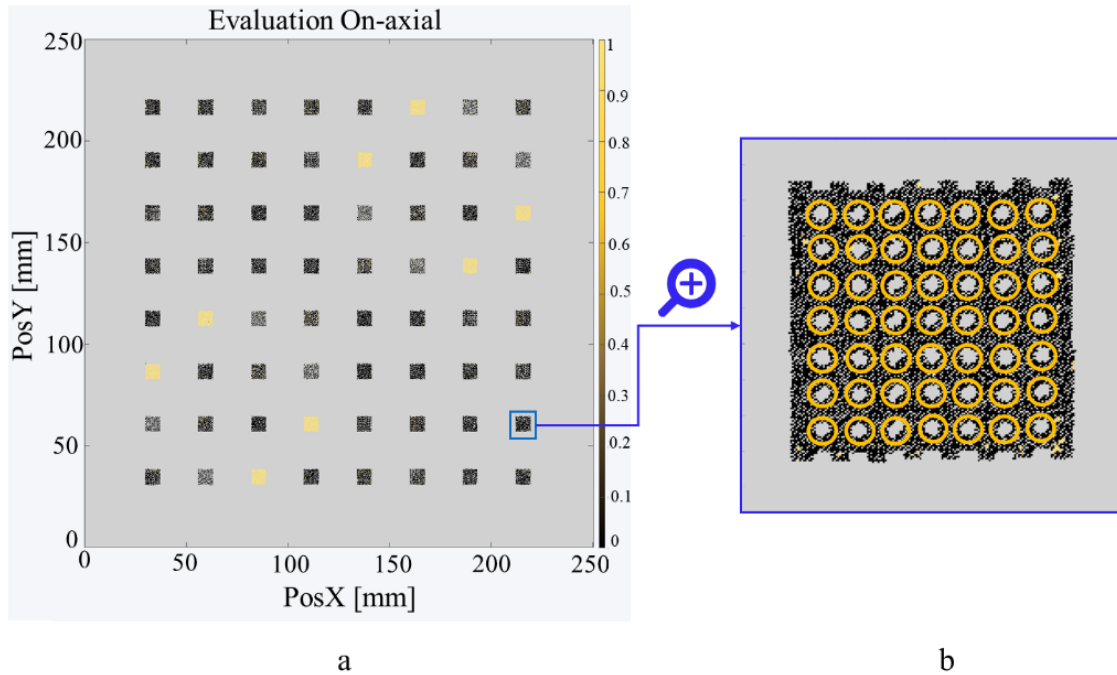


Figure 3-8: a) An example of an image generated by the software for one layer of the print, b) Selection of 49 regions of interest around each defect in sample R2 at Location 1.

In the following sections, the AL algorithm results with the selected threshold range will be presented.

3.2.5 Statistical analysis

The experiments' results are compared through the determination of the average and standard deviation of 'indicators' (yellow pixels) percentage in each cluster. Besides, to investigate the statistical significance of each input, a single factor (size and distribution separately) analysis of variance (ANOVA) with a significance level (α) of 0.05 is performed. The ANOVA is conducted on the number of indicators to study if the size/distribution of artificial defects and their location on the build plate affect the light intensity signal ($p\text{-value} < \alpha$).

3.2.6 Computed tomography (CT-Scanning)

All samples were analyzed for micro- CT scan (μ CT) to validate the actual pores' positions and distribution. The coupon samples were subjected to the X-ray μ CT on Zeiss Xradia Versa 520 system [Carl Zeiss Microscopy GmbH, Germany] with 10 W source power, 160 KV source voltage, 14 μ m voxel size, and 14 mm field of view. A HE6 filter was used, where the X-ray optics was 0.4 \times lens. Exposure time was set to 3.0 s, and the number of projections was 1601.

The analysis of the coupon samples was then performed using the Dragonfly Pro v4.0 (Object Research Systems Inc., Montréal, QC) software package to find the positions of defects (x, y, and z-direction) as well as the density of samples. It should be noted that Dragonfly provides the alignment feature to re-orient and redefine coordinates based on the STL CAD file. To this end, vertical and horizontal grooves considered in the coupon design were used to correctly register the CT data versus STL models. Consequently, the CT-Scan results were compared with the analyzed data from the photodiodes, as explained in the following sections.

3.2.6.1 Correlation between CT- scan and analyzed data

Based on the knowledge gained from detecting the artificial defects (samples R2, R3, R4, and R5), the rest of the samples in R-series (R6, R7, and R8) and T-series are investigated through a new image segmentation approach. In the first step, all collected images are stacked to create one model. In the second step, each model is segmented into 82 batches (Figure 3-9. a). Each batch includes three layers of the print (120 μ m). In the next step, each is subdivided into 4356 voxels (Figure 3-9. b). The size of each voxel is 120 (μ m) \times 120 (μ m) \times 120 (μ m) selected based on the smallest size of the artificial defects detected by analyzing the data from Section 3.2.3.

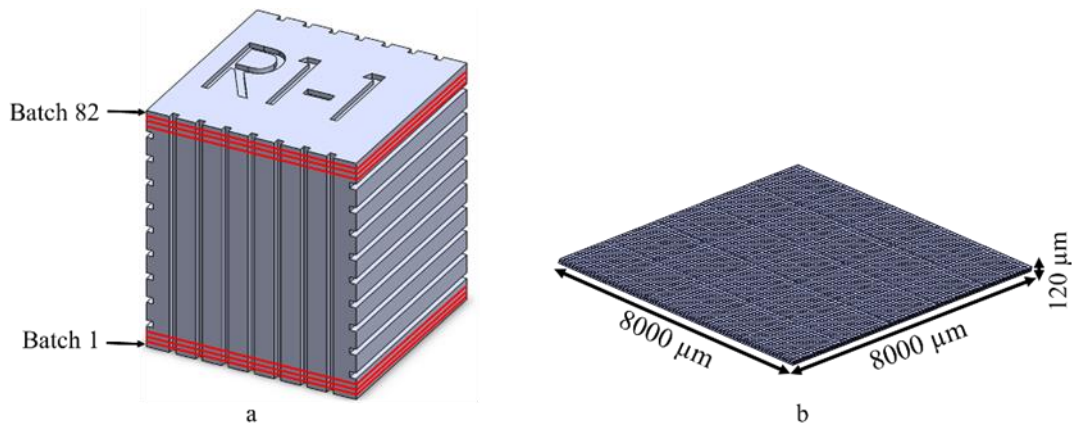


Figure 3-9: The schematic of a) a sample that is segmented in 82 batches, b) a batch, which is divided into 4356 voxels (which includes three layers).

Also, to avoid missing any partial pores or any pores located on the edge of voxels, both current and adjacent voxels are analyzed in two different area sizes: $60\ \mu\text{m}$ ($30\ \mu\text{m}$ inside the current voxel and $30\ \mu\text{m}$ inside the adjacent voxel, as demonstrated in Figure 3-10a) and $120\ \mu\text{m}$ ($60\ \mu\text{m}$ inside the current voxel and $60\ \mu\text{m}$ inside the adjacent voxel, as demonstrated in Figure 3-10b).

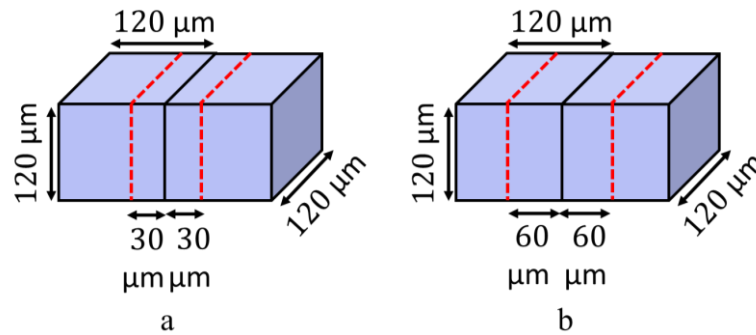


Figure 3-10: Two adjacent voxels with considering area of a) $30\ \mu\text{m}$ and b) $60\ \mu\text{m}$ from each edge.

This analysis could help when there are less than three yellow pixels located in the voxel. With less than three adjacent yellow pixels, a voxel is labeled as nominal (Section 3.2.4); however, when there is one more yellow pixel located at the edge of the voxel, then the following possibilities could be discussed:

- 1- Both adjacent voxels (voxel 1 and voxel 2 in Figure 3-11a) had zero yellow pixel in the distance of $30\ \mu\text{m}$ from the edge \rightarrow both voxels 1 and 2 were labeled as nominal.

- 2- Voxel 1 had two yellow pixels and voxel 2 had zero yellow pixel in the distance of $30\ \mu\text{m}$ from the edge (Figure 3-11b) \rightarrow voxel 1 was labeled as an anomaly and voxel 2 was labeled as nominal.
- 3- Voxel 2 had two yellow pixels and voxel 1 had zero yellow pixel in the distance of $30\ \mu\text{m}$ from the edge (Figure 3-11c) \rightarrow voxel 1 was labeled as an anomaly and voxel 2 was labeled as nominal.
- 4- Both adjacent voxels had two yellow pixels in the distance of $30\ \mu\text{m}$ from the edge (Figure 3-11d) \rightarrow both voxels 1 and 2 were labeled as an anomaly.

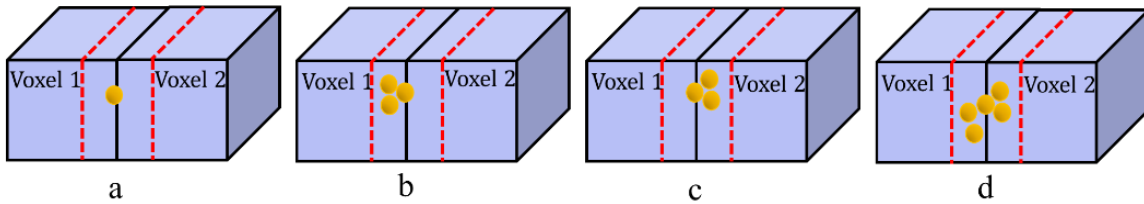


Figure 3-11: The schematic of when one yellow pixel located at the edge of voxel and a) no yellow pixels identified in the adjacent voxel, b and c) two yellow pixels identified in one of the voxels, and d) two yellow pixels identified in both voxels (please check Figure 3-9c for the size of voxels).

At the end, the result of 357192 voxels for each sample is compared with the corresponding CT data to establish the matching matrix [80]. The matching matrix is used the ground truth table in which each voxel is labeled based on the presence of porosity detected by the CT-Scan and AL algorithm. Then, each 3D neighbourhood is labeled as either pore or nominal (Table 3-6) [60][44].

Table 3-6: Confusion matrix to compare the prediction of the algorithm (AL) and the actual defect (CT-scan).

		Prediction (AL algorithm)	
		Anomaly	Nominal
Actual defect (CT-scan)	Anomaly	TP	FN
	Nominal	FP	TN

The matching matrix can evaluate the algorithm by four criteria:

- TP (true positive): Actual anomaly voxel that is correctly predicted,
- FP (false positive): Actual anomaly voxel that is wrongly predicted,

- FN (false negative): Actual nominal voxel that is wrongly predicted, and
- TN (true negative): Actual nominal voxel that is correctly predicted [81].

Besides, the accuracy of the prediction are considered given by [81]:

$$Accuracy = \frac{TP+TN}{TP+FP+FN+TN} \quad (\text{Eq 3.1})$$

A high-level schematic of the overall process is represented in Figure 3-12.

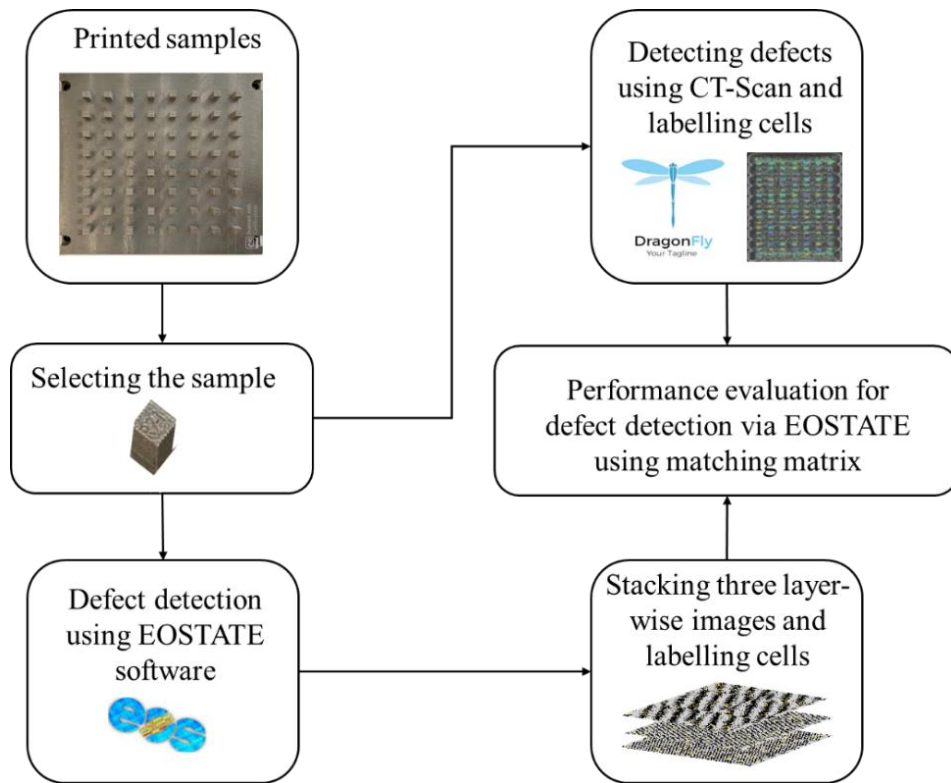


Figure 3-12: Schematic to compare the CT-Scan and EOSTATE software results to establish a matching matrix.

3.3 Results and Discussion

3.3.1 Analysis of the data collected by Absolute Limits algorithm

The results of deploying the AL algorithm and the effect of threshold ranges on Sample R1- R8 will be presented based on samples' location on the build plate. The following ranges of the threshold were chosen for the analysis of R-series samples:

- 1) Samples R1- R5: the threshold range of 12000-20000 and a window length of 10,
- 2) Sample R6: threshold 5500-11000 and window length 10,
- 3) Sample R7: threshold 12000-18000 and window length 5, and
- 4) Sample R8: threshold 10600-17000 and window length 10.

The results are presented in two sections: examples of the population and spatial distribution of the yellow pixels/indicators for each sample of R-series on selected layers (Figure 3-13) and the average number of yellow pixels/indicators and their standard deviations in the regions of interest (Figure 3-14 and Figure 3-15). The effect of artificial defect size, incorporated into the design of Samples R2, R3, R4, R6, R7, and R8, is shown in Figure 3-14 by the pink, teal, purple, orange, green, and blue colour, respectively. Moreover, the influence of artificial defect distribution is represented in Figure 3-15. The effect of underneath layers of the powder on the successive layer is discussed to identify the defect detection performance range.

3.3.1.1 Examples of the population and spatial distribution

As demonstrated in Figure 3-13, layer 1, printed in the successive layer of artificial voids, shows major yellow indicators in Samples R2, R3, R4, and R5, printed with the print parameters listed in Table 3-1. Three samples (R6, R7, and R8) were designed to mimic the artificial and randomized voids initiated due to the lack-of-fusion. Artificial defects are detectable in Samples R7 and R8. However, in Sample R6, the power was kept constant at 100 Watt, which resulted in low energy density. As a result, the ripples in the signal are not dominant adequately to be detectable or separated from the rest of the signal. In fact, the noise to signal ratio is very high in Sample R6.

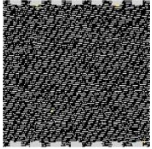
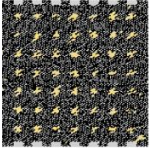
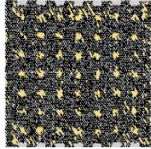
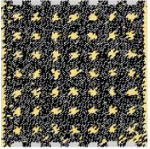
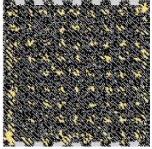
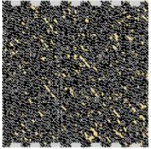
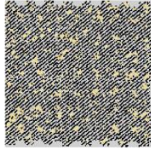
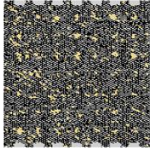
<p>R1- Layer 1- Set 1- Location 8</p> 	<p>R2- Layer 1- Set 1- Location 4 defect size (H, Ø= 200µm)</p> 	<p>R3- Layer 1- Set 2- Location 6 Defect size (H= 160 µm and Ø= 200 µm)</p> 	<p>R4- Layer 1- Set 5- Location 6 Defect size (Ø= 200 µm)</p> 
<p>R5- Layer 1- Set 3- Location 1 Defect size (H, Ø= 200 µm) Distribution 8×8</p> 	<p>R6- Layer 1- Set 5- Location 7 Defect size (H, Ø= 100 µm)</p> 	<p>R7- Layer 1- Set 6- Location 2 Defect size (H, Ø= 200 µm)</p> 	<p>R8- Layer 1- Set 5- Location 8 Defect size (H, Ø= 150 µm)</p> 

Figure 3-13: The population and distribution of indications for AL algorithm – R-series (Figure 3-3a).

3.3.1.2 Statistical analysis of artificial and randomized defects

For the confidence level, a statistical analysis is conducted on the detection datasets. Four Samples R2 to R5 are designed with a combination of artificial pore size, shape, and distribution to investigate the nature of light intensity signal at these combining circumstances. Sample R2 incorporated the variation of cylindrical height and radius of the un-melted powder layer. Sample R3 included various cylindrical void heights (120 µm- 320 µm) to mimic the un-melted powder layer; however, the radius of the cylindrical voids was kept constant (200 µm). The larger spherical defects with different spatial distributions throughout the coupons were studied in Samples R4 and R5, respectively. The average and standard deviation of the yellow pixels/indicators are shown in Figure 3-14 and Figure 3-15, shedding some light on the effect of defects' size (R2, R3, R4, R6, R7, and R8) and distribution (R5). These figures represent a deviation in the light intensity signal based on each sample's location in the build plate (Figure 3-3a). Each sample was printed multiple times to assess the repeatability factor. Six sets of R2, R4, R5, R6, R7, and R8 and three sets of R3 were printed. The figures demonstrate the average and standard deviation of all similar sizes/distribution associated with the number of sets per each sample. In Figure 3-14, nine tags (S1, S2, S3, S4, S5, S6, D1, D2, and D3) are defined which showed void sizes of each sample as demonstrated in Table 3-7. For example, sample R2- location 1 (Figure 3-14) shows three void sizes tagged as S1, S2, and S3. These tags represent all voids in R2 with the size of H, Ø= 200 µm, H, Ø= 150 µm, and H, Ø= 100 µm, respectively (see Figure 3-2a).

Table 3-7: The Reference of Figure 3-14 and Figure 3-15.

Sample	Defect type	Defect size (μm)	Tag name
R2, R6, R7, and R8	Cylindrical artificial defect	\emptyset , H=200	S1
		\emptyset , H=150	S2
		\emptyset , H=100	S3
R3	Cylindrical artificial defect	$\emptyset=200$, H=320	S1
		$\emptyset=200$, H=280	S2
		$\emptyset=200$, H=240	S3
		$\emptyset=200$, H=200	S4
		$\emptyset=200$, H=160	S5
		$\emptyset=200$, H=120	S6
R4	Spherical artificial defect	$\emptyset=300$	S1
		$\emptyset=250$	S2
		$\emptyset=200$	S3
R5	Cylindrical artificial defect	Distribution: 5 \times 5	D1
		Distribution: 9 \times 9	D2
		Distribution: 8 \times 8	D3

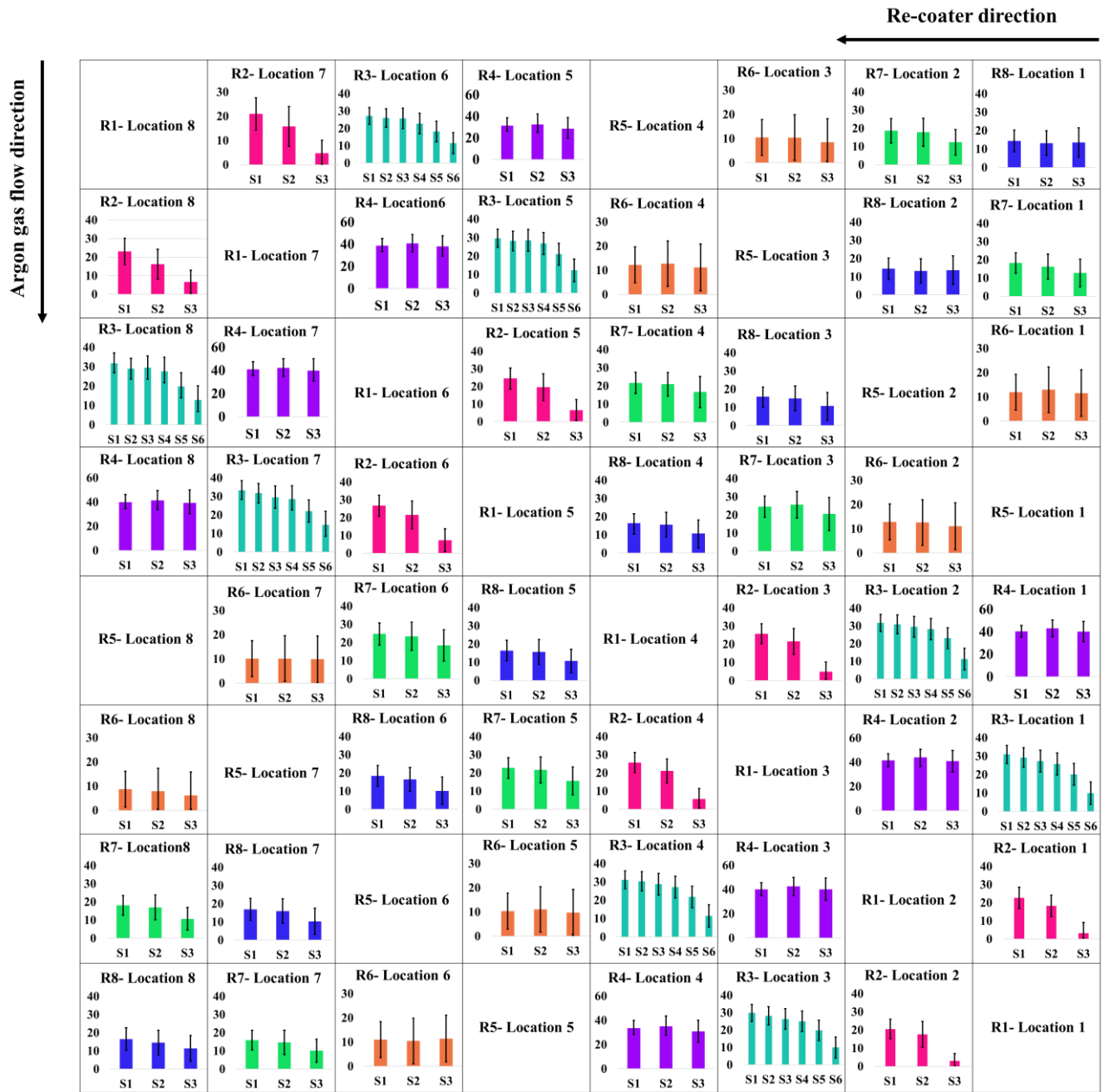


Figure 3-14: The percentage of average and standard deviation of yellow indicators in the region of interests for the selected layers based on the output of the AL algorithm (Samples R2, R3, R4, R6, R7, and R8 are shown by pink, teal, purple, orange, green, and blue, respectively).

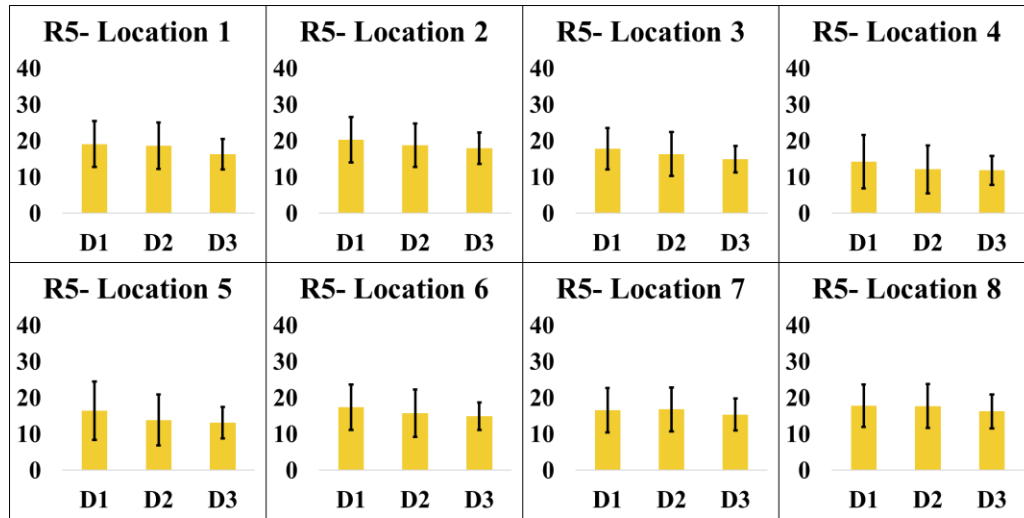


Figure 3-15: The percentage of average and standard deviation of yellow indicators in the region of interest for the selected layers and after applying the AL algorithm (Sample R5). D1, D2, and D3 mean three different void distribution embedded in sample R5 (D1= 5×5, D2= 8×8, and D3= 9×9).

It should be noted that each size of defects embedded in sample R2 (100 μm , 150 μm , and 200 μm) was created 1764 times in the build (number of defects in one set=49, number of sets in one sample=6, so the number of defects in one sample= 49×6=294, additionally numbers of locations of each sample=6. As a result, each defect was created 294×6=1764 times). Analyzing the average of the yellow pixels/indicators in the area of interest in Sample R2 (Figure 3-8) demonstrates the 5.21±5.9%, 19.93±5.48%, and 23.71±5.39% of selected areas are filled by indicators for 100 μm , 150 μm , and 200 μm cylindrical void sizes, respectively (Figure 3-14. Pink colour). The counterpart results in Sample R3 demonstrate approximately 17.69±5.55%, 20.70±5.31%, 26.45±5.77%, 28.09±6.3%, 29.15±6.21%, and 30.63±6.64% of the selected area covered by the indicators for 120 μm , 160 μm , 200 μm , 240 μm , 280 μm , and 320 μm height, respectively (Figure 3-14. Teal colour). Each size of defects in sample R3 was created 882 times in the build. The results suggest that an increase in artificial defects height yields a higher number of yellow indicators in interest areas. It may be attributed to the exceeded disturbance in the intensity signal when the un-melted powder layer's thickness increases. Additionally, the results for Samples R2 and R3 suggest that 120 μm is the smallest detection by the software. The average number of indicators in 100 μm defects for Sample R2 is half of the average number of indicators in 120 μm defects (see Sample R3). For the defects larger than 120 μm , the numbers of yellow pixels are in the same range.

The result of Sample R4 represents the average and deviation of $37.17 \pm 12.99\%$, $40.15 \pm 13.25\%$, and $38.30 \pm 10.97\%$ for the artificial defects with 200 μm , 250 μm , and 300 μm diameter (Figure 3-14. Purple colour). Also, each defect size was embedded 1764 times in sample R4. Studying the result of larger size defects in R4 indicates that the hardware and algorithm are less sensitive to defects larger than 200 μm . It may be attributed to the stability of temperature in the process when the size of defects is larger, causing less variation in signal perturbation in the emitted light according to Planck's law. The void distribution effect in Sample R5 suggests that the indicators cover approximately $17.44 \pm 6.5\%$, $16.24 \pm 6.33\%$, and $15.09 \pm 4.17\%$ of the selected areas (D1: 5×5 , D2: 9×9 , and D3: 8×8 of defects were created 750, 2430, and 1920 times). The counterpart result inspection proves that the void spatial distribution may not significantly affect the light intensity signal (Figure 3-15. yellow colour).

In Sample R6, the number of indicators is the same for different sizes of designed defects (Figure 3-14. orange colour), meaning that the detection is not successful, as discussed in Section 3.3.1.1. However, the artificial defects are identified in Samples R7 and R8, printed with a high hatching distance of 150 μm and a high-speed of 1500 mm/sec, respectively. The defect size also plays a role in the percentage of indicators in Sample R7 (Figure 3-14. green colour) and Sample R8 (Figure 3-14. blue colour); however, the effect of size in these samples is less than in samples printed with standard print parameters (R1).

As observed in Figure 3-14, the number of indicators in different positions is not uniform in the build plate. Therefore, the samples' location in the build plate confirms that the direction of gas flow and recoater affects the formation of LoF porosity, as also discussed in the literature [82]. The gas flow distribution is normally not uniform in the build plate [83], resulting in different numbers of yellow pixels/indicators while printing one identical sample at different build plate positions.

After evaluating the data for all samples, the ANOVA is conducted for exploring the effect of sample positions in the build plate, the size (samples R2, R3, R4, R6, R7, and R8), and distribution (sample R5) of artificial defects on p-value to shed some light on repeatability and confidence variance (Table 3-8).

Table 3-8: The range of p-value from ANOVA single factor analysis of the variance.

Sample	Defect type	Defect size (μm)	Effect of locations	Size of defects	Distribution of defects
R2	Cylindrical artificial defect	\emptyset , H=200	< 0.05	< 0.05	-
		\emptyset , H=150	< 0.05		
		\emptyset , H=100	< 0.05		
R3	Cylindrical artificial defect	$\emptyset=200$, H=320	< 0.05	< 0.05	-
		$\emptyset=200$, H=280	< 0.05		
		$\emptyset=200$, H=240	< 0.05		
		$\emptyset=200$, H=200	< 0.05		
		$\emptyset=200$, H=160	< 0.05		
		$\emptyset=200$, H=120	< 0.05		
R4	Spherical artificial defect	$\emptyset=300$	< 0.05	< 0.05	-
		$\emptyset=250$	< 0.05		
		$\emptyset=200$	< 0.05		
R5	Cylindrical artificial defect	Distribution: 5 \times 5	< 0.05	-	> 0.05
		Distribution: 9 \times 9	< 0.05		
		Distribution: 8 \times 8	< 0.05		
R6	Cylindrical artificial defect and randomized defect	\emptyset , H=200	< 0.05	< 0.05	-
		\emptyset , H=150	< 0.05		
		\emptyset , H=100	< 0.05		
R7	Cylindrical artificial defect and randomized defect	\emptyset , H=200	< 0.05	> 0.05	-
		\emptyset , H=150	< 0.05		
		\emptyset , H=100	> 0.05		
R8	Cylindrical artificial defect and randomized defect	\emptyset , H=200	< 0.05	< 0.05	-
		\emptyset , H=150	< 0.05		
		\emptyset , H=100	< 0.05		

The ANOVA analysis confirms that the effect of samples' positions on the number and distribution of yellow pixels/indicators in which most of the samples show a p-value < 0.05 (Table 3-8). Additionally, the effect of artificial defects' size was discussed in the previous section (Figure 3-14), and a similar conclusion is drawn when the ANOVA is conducted (Table 3-8). The ANOVA analysis supports a significant statistical difference between different sizes of defects on the light intensity signal and consequently on the number of yellow pixels/indicators. Moreover, the ANOVA analysis demonstrates an insignificant difference between the scenarios of distribution (Sample R5). As a result, the distribution of defects embedded in the sample may not be a significant factor in the light intensity signal variation.

3.3.2 Computed tomography (CT-Scanning)

The diameter and location of the pores and density of the coupon sample were calculated through the CT datasets. The front and top views of samples with the artificial defects (sample R4-4), artificial and randomized defects (sample R7-1), and the randomized defects (sample T4-4) are shown in Figure

3-16. The front and top views of samples R4-4, R7-1, and T4-4 are shown in Figure 3-16 (a, d), Figure 3-16 (b, e), and Figure 3-16 (c, f), respectively. It should be noted that the CT software enlarges the size of defects for better visualization.

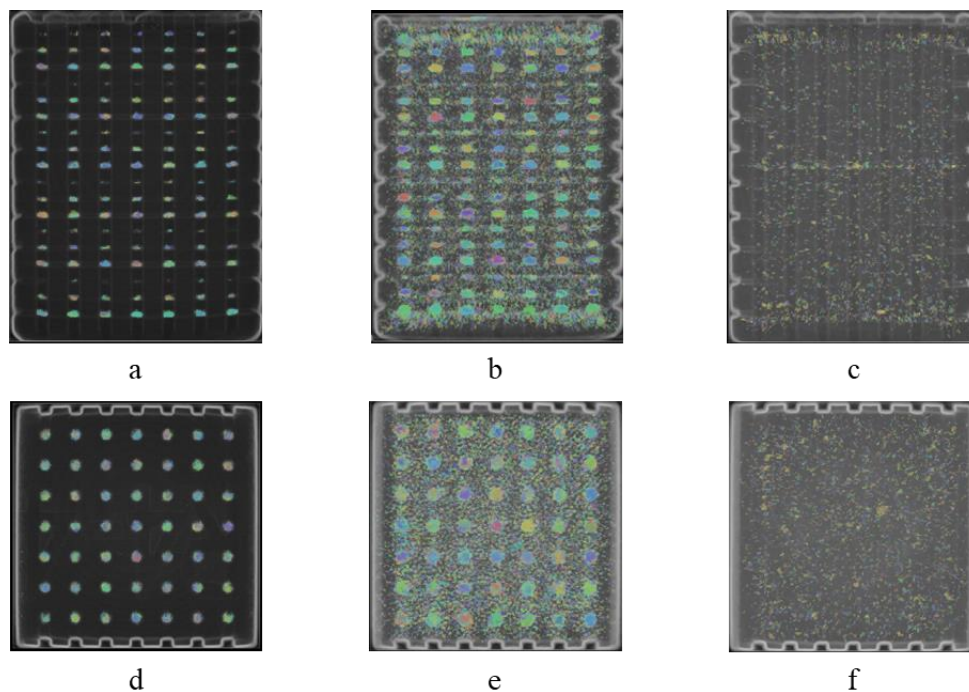


Figure 3-16: CT data of front view of a) R4- location 4, b) R7- location 1, and c) T4- location 4 and top view of d) R4- location 4, e) R7- location 1, and f) T4- location 4.

3.3.2.1 Correlation between CT- scan and Absolute Limits results for samples with artificial defects (R2, R3, R4, and R5)

Samples R2, R3, R4, and R5 from location 4 are selected to analyze by the CT-scan. In the consecutive layer of artificial defects (Layer 1), the percentage of the identified defect, with respect to the number of defects in the design, is calculated; also, the density of each part is measured (Table 3-9). It should be noted that the dimension of designed voids is shrunk in real parts, and as a result, the size of the identified defects by the CT is not the same as the designed size (Figure 3-17).

Table 3-9: The percentage of identification for each size of the defect and density of each sample.

Sample	Defect Type (μm)	Percentage of Identification by Absolute Limits (%)	Density
R2- location 4	\emptyset , H=200	100	99.89
	\emptyset , H=150	100	
	\emptyset , H=100	100	
R3- location 4	$\emptyset=200$, H=320	99.31	99.28
	$\emptyset=200$, H=280	100	
	$\emptyset=200$, H=240	100	
	$\emptyset=200$, H=200	100	
	$\emptyset=200$, H=160	100	
	$\emptyset=200$, H=120	100	
R4- location 4	$\emptyset=300$	100	99.69
	$\emptyset=250$	100	
	$\emptyset=200$	100	
R5- location 4	Distribution: 5 \times 5	76	98.08
	Distribution: 9 \times 9	77.78	
	Distribution: 8 \times 8	72.5	

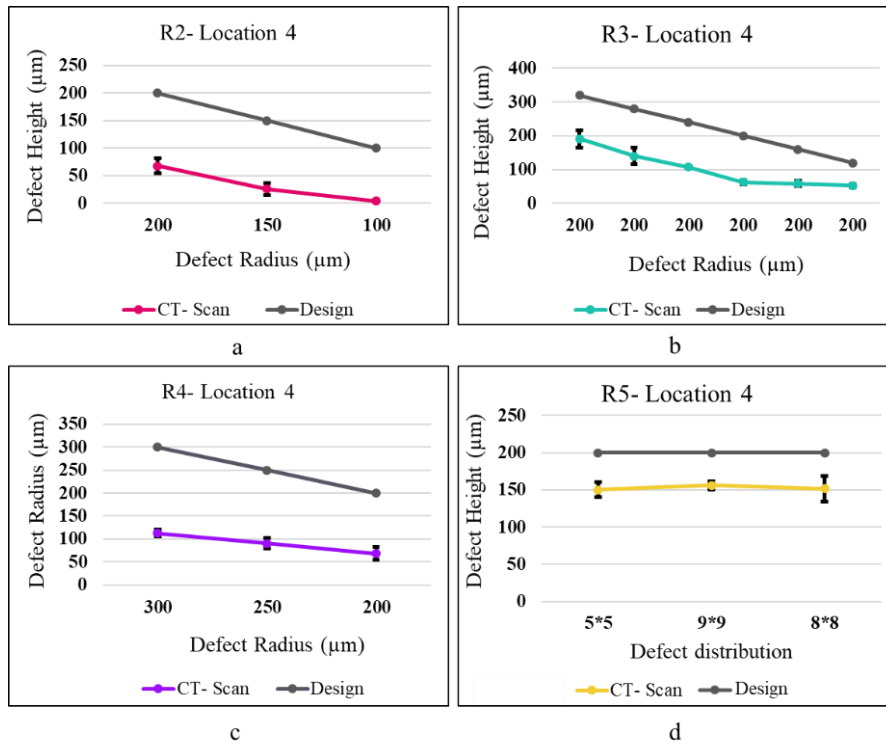


Figure 3-17: The amount of shrinkage in the sample a) R2- location 4 b) R3- location 4 c) R4- location 4 d) R5- location 4 for each type of defects.

The CT-scan analysis of Samples R1-R5 was conducted for location 4 on the build plate. It should be noted that some pores were healed in the process based on the CT-scan results. By removing those pores, the detection of MPM analysis shows most of the defects are identified (Table 3-9).

The CT-scan analysis of Samples R2, R3, R4, and R5 demonstrates the dimension deviation of defects (Figure 3-17). The deviation is limited to 150 μm in Samples R2 and R3 (Figure 3-17.a and Figure 3-17.b). However, analyzing the CT-scan of Sample R5 (Figure 3-17.d) results in only a 50 μm dimension deviation. Less dimension deviation than Sample R2 and R3 could also suggest the stability of temperature and, as a result, intensity signal in the process when encountered defects larger than 200 μm , as discussed in Section 3.3.1.2. Moreover, less deviation of R5 defects could also happen due to the shape of defects, which is cylindrical in this sample. The sample R4 defects have more deviation in the final shrunk size, and it could be due to the spherical shape of artificial defects (Figure 3-17.c). The comparison results between Sample R4 and R5 shows that all defects are larger than 200 μm , resulting in a stable intensity signal. At the same time, the defect shape embedded in Sample R4 is spherical. As a result, more deviation in Sample R4 is happened only because of the defect's shape. Also, the CT-Scan result for R5- 4 (Figure 3-17.d) confirms that defects in the gas flow direction were partially detectable.

Another important note is that although the designed voids smaller than 120 microns is not detectable, the resultant void size turned out to be around 60 to 70-micron size after shrinkage. This may suggest that the proposed methodology may detect pores that are eventually in the range of 60 to 70 microns.

3.3.2.2 Correlation between CT- scan and Absolute Limits results for samples incorporated artificial defects and randomized defect (R6, R7, and R8)

The analysis of sample R6 in previous sections showed ripples in the signal are not dominant adequately to be separated from the rest of the signal. In fact, the noise to signal ratio is high in sample R6 which leads to the distribution of yellow pixels all over the sample. So, sample R6 showed an accuracy of around 30% to detect artificial defects. The number of identified defects in the consecutive layer of the artificial defect is calculated for Samples R7 and R8. For Samples R7 and R8, the average percentage of six sets of defects is determined for H, $\text{Ø}=200 \mu\text{m}$, H, $\text{Ø}=150 \mu\text{m}$, H, $\text{Ø}=100 \mu\text{m}$ with respect to their position in the build (Table 3-10 and Table 3-11). Also, the amount of dimension deviation of R7 and R8 is shown in Figure 3-18 and Figure 3-19.

Table 3-10: The percentage of identification for each size of the defect and density of sample R7.

Sample	Defect radius and height (μm)	Percentage of Identification by Absolute Limits (%)	Density
R7- location 1	200	100	97.83
	150	100	
	100	100	
R7- location 2	200	98.94	97.68
	150	97.61	
	100	100	
R7- location 3	200	100	98.96
	150	100	
	100	100	
R7- location 4	200	100	97.88
	150	100	
	100	100	
R7- location 5	200	100	92.63
	150	100	
	100	100	
R7- location 6	200	100	98.36
	150	100	
	100	100	
R7- location 7	200	100	96.78
	150	100	
	100	100	
R7- location 8	200	100	98.1
	150	100	
	100	100	

Table 3-11: The percentage of identification for each size of the defect and density of sample R8.

Sample	Defect radius and height (μm)	Percentage of Identification by Absolute Limits (%)	Density
R8- location 1	200	100	98.83
	150	100	
	100	100	
R8- location 2	200	100	98.61
	150	100	
	100	100	
R8- location 3	200	100	98.12
	150	100	
	100	97.52	
R8- location 4	200	100	99.4
	150	100	
	100	100	
R8- location 5	200	100	98.94
	150	100	
	100	100	
R8- location 6	200	100	99.07
	150	100	
	100	100	
R8- location 7	200	100	99.12
	150	100	
	100	100	
R8- location 8	200	100	98.8
	150	100	
	100	100	

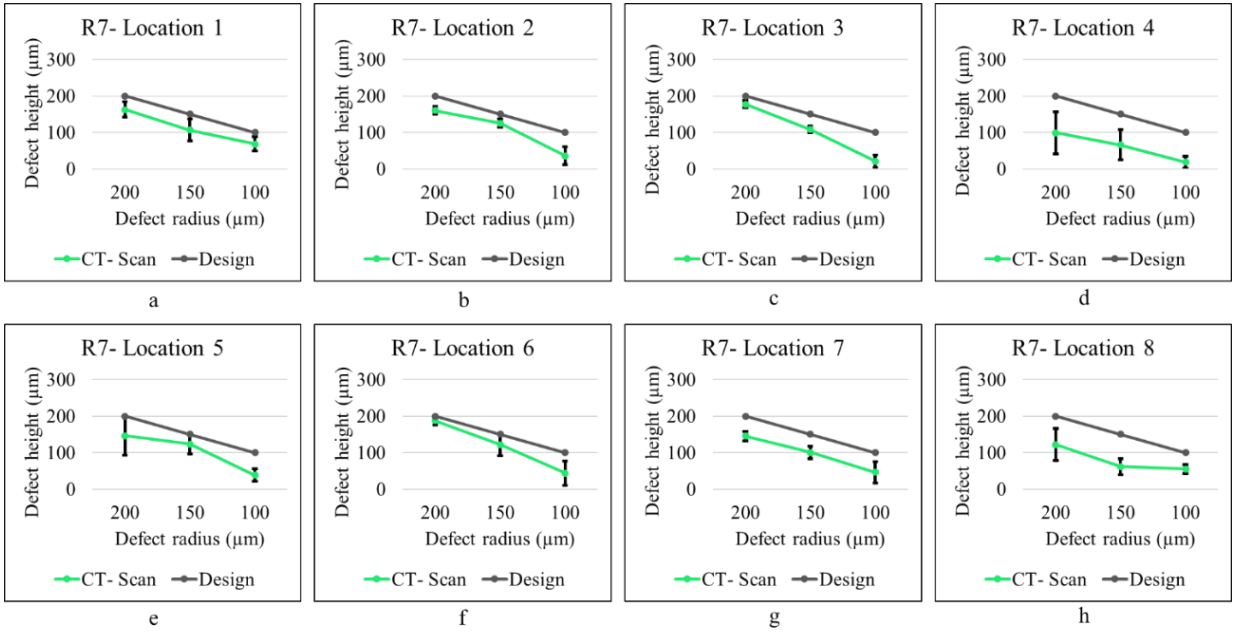


Figure 3-18: The amount of shrinkage in the sample R7 a) Location 1, b) Location 2, c) Location 3, d) Location 4, e) Location 5, f) Location 6, g) Location 7, and h) Location 8.

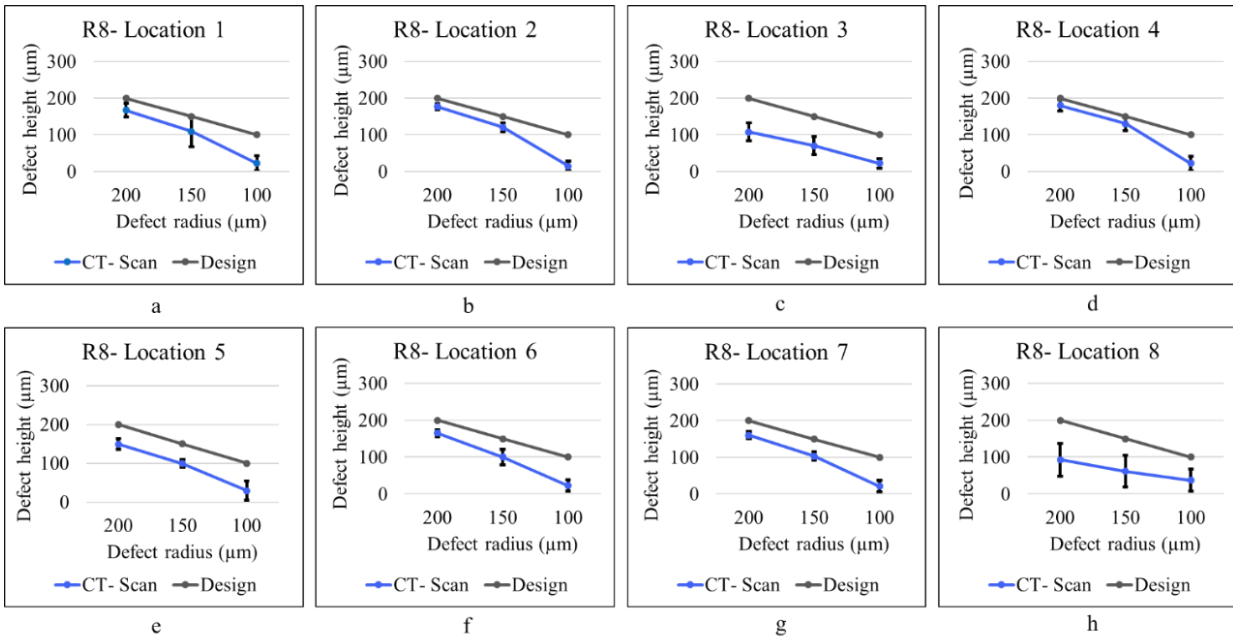


Figure 3-19: The amount of shrinkage in the sample R8 a) Location 1, b) Location 2, c) Location 3, d) Location 4, e) Location 5, f) Location 6, g) Location 7, and h) Location 8.

The CT-scan analysis for R7 and R8 is conducted for all of the positions on the build plate. By removing the healed pores, firstly two approaches which were discussed in Section 3.2.6.1 for voxels with yellow pixels on the edge demonstrate that 30 μm distance from the edge shows higher accuracy to identify defects as shown in Table 3-12 and Table 3-13 for samples R7 and R8.

Table 3-12: Accuracy (%) of AL algorithm to predict pores based on the CT-Scan result for sample R7 with two different sizes of distance (30 μm and 60 μm) from each voxel to avoid missing any partial pores or pores located on the edge of the voxel.

Distance from the edge	Location 1	Location 2	Location 3	Location 4	Location 5	Location 6	Location 7	Location 8
30 μm	76.76	73.81	69.89	71.6	73.66	75.71	77.51	76.94
60 μm	61.28	58.23	54.12	63.5	64.12	59.87	61.45	62.4

Table 3-13: Accuracy (%) of AL algorithm to predict pores based on the CT-Scan result for sample R8 with two different sizes of distance (30 μm and 60 μm) from each voxel to avoid missing any partial pores or pores located on the edge of the voxel.

Distance from the edge	Location 1	Location 2	Location 3	Location 4	Location 5	Location 6	Location 7	Location 8
30 μm	67.58	72.99	81.89	76.72	79.82	70.87	65.15	49.78
60 μm	59.25	62.78	68.53	67.24	68.45	61.78	57.47	40.12

When considering 60 μm from each edge, the accuracy for samples R7 is approximately between 54% to 64% and for sample R8 is approximately between 40% to 68%; however, considering 30 μm from each edge results in higher accuracy. Lower accuracy of 60 μm distance from each edge could be because most of the voxels have labeled as an anomaly which is not correct, resulting in a low number of TN rates when comparing the results with CT-Scan. As a result, 30 μm distance from each edge for voxels with less than three yellow pixels and with yellow pixel at the edge is considered for the following analysis.

By comparing the CT-scan analysis and AL algorithm result for R7 and R8, the detection of MPM analysis demonstrates most of the defects are identified in the samples printed with high hatching distance (Table 3-10) and high speed (Table 3-11). The dimension deviation of defects results in approximately $150.03 \pm 27.57 \mu\text{m}$, $101.74 \pm 23.63 \mu\text{m}$, and $40.97 \pm 21.23 \mu\text{m}$ for sample R7 and $155.69 \pm 20.40 \mu\text{m}$, $104.37 \pm 25.36 \mu\text{m}$, and $20.84 \pm 31.10 \mu\text{m}$ for sample R8, thus leading to the direct effect of defect size in deviation.

Additionally, the output results for the randomized defects are correlated with the computed tomography (Micro CT) to validate the AL algorithm accuracy in real scenarios. The voxel cell is considered the same size as the smallest pore detection size ($120\ \mu\text{m}\times 120\ \mu\text{m}\times 120\ \mu\text{m}$) to establish the correlation between CT-Scan and MPM results. The matching result of the samples with a high hatching distance and a high speed is evaluated using the matching matrix (Table 3-14 and Table 3-15), when true positive, true negative, and accuracy percentage of the AL algorithm are calculated.

Table 3-14: Evaluation metrics of AL algorithm based on the CT-Scan result for sample R7.

Performance	Location 1	Location 2	Location 3	Location 4	Location 5	Location 6	Location 7	Location 8
TP (%)	74.08	74.94	74.85	75.31	75.74	74.16	75.15	75.10
TN (%)	60.32	60.30	66.82	61.27	63.10	60.47	66.49	65.22
Accuracy (%)	76.76	73.81	69.89	71.60	73.66	75.71	77.51	76.94

Table 3-15: Evaluation metrics of AL algorithm based on the CT-Scan result for sample R8.

Performance	Location 1	Location 2	Location 3	Location 4	Location 5	Location 6	Location 7	Location 8
TP (%)	74.73	76.19	75.76	73.18	76.57	75.72	74.57	79.13
TN (%)	60.29	61.17	68.03	68.19	67.11	68.53	61.20	48.86
Accuracy (%)	67.58	72.99	81.89	76.72	79.82	70.87	65.15	49.78

The results of Sample R7 show the approximately $74.91\pm 0.56\%$ correct prediction compared to the actual porosity (TP) and $62.99\pm 2.81\%$ correct prediction of voxels without any porosity (TN). Also, the accuracy of Sample R7 guarantees more than $74.48\pm 2.73\%$ to identify correct nominal and abnormal voxels. Moreover, the TP rate results indicate a few numbers of FP voxels, meaning a high accuracy of porosity prediction. The result of Sample R8 shows a similar conclusion. In addition, the result of Sample R8 also indicates the effect of the sample's position on the light intensity signal. The accuracy of Sample R8 demonstrates that location 8 has the lowest rate of correct prediction among other samples, which indicates the effect of gas flow and recoater on the defect detection platform. Although there is a challenge to guarantee the repeatability of prediction for all build plate locations, the algorithm could identify the Lack-of-fusion porosity with high accuracy for most samples incorporating both artificial and randomized defects.

3.3.2.3 Correlation between CT- scan and Absolute Limits results for samples with only randomized defect (T2, T3, and T4)

In this step, the method of segmentation is the same as in Section 3.3.2.1. The evaluation metrics for samples T3 and T4 are represented in Table 3-16 and Table 3-17. Sample T2 shows around 30% accuracy and defect detection was not successful as also discussed for sample R6 in Section 3.3.2.2.

Table 3-16: Evaluation metrics of AL algorithm based on the CT-Scan result for sample T3.

Performance	Location 1	Location 2	Location 3	Location 4	Location 5	Location 6
TP (%)	73.83	74.42	73.52	74.26	74.47	74.05
TN (%)	51.56	57.46	50.78	51.76	54.42	53.81
Accuracy (%)	70.28	73.15	71.97	66.79	68.94	69.74

Table 3-17: Evaluation metrics of AL algorithm based on the CT-Scan result for sample T4.

Performance	Location 1	Location 2	Location 3	Location 4	Location 5	Location 6
TP (%)	75.18	75.30	76.37	75.20	75.15	75.47
TN (%)	70.44	73.38	70.41	63.82	64.28	65.19
Accuracy (%)	72.21	74.71	71.78	73.41	73.84	71.01

The result represents that the algorithm's sensitivity to finding the true positive rate for T3 (high hatching distance) and T4 (high speed) is more than $74.09 \pm 0.37\%$ and $75.44 \pm 0.46\%$, respectively, which confirm that the algorithm could detect the pore's location. Still, a true negative rate limits the performance of the algorithm. The accuracy of the AL Algorithm shows more than $70.14 \pm 2.24\%$ and $72.82 \pm 1.39\%$ correct detection; however, it can improve by reducing the number of false-positive (FP) voxels, which may be provided by changing the pixel resolution and threshold method. Although some studies were conducted to correlate sensors' data and quality of parts with better prediction [60], [84], [85], all of them used in-house developed systems where in-situ sensors were incorporated into the setup, exposing a challenge for users to replicate their results due to the accessibility issue to the in-house developed setups. In contrast, this study lays down the analysis of commercially available in-situ sensory data that users can replicate for industrial applications and academic research. In addition, a new machine learning detection algorithm to identify smaller defects is a part of an on-going effort to find smaller size defects rapidly and precisely.

3.4 Summary

In this study, the effect of a lack-of-fusion porosity was investigated on the light intensity signal emitted from the melt pool and collected by an in-situ photodiode(s). The collected intensity signal was analyzed by the Absolute Limits, Signal Dynamics, and Short-Term Fluctuation algorithms, followed by an image processing method. Artificial and randomized defects were designed and analyzed to evaluate the performance of hardware and algorithms. The predicted results were evaluated by the CT-scan through volumetric approach.

Chapter 4. An unsupervised machine learning algorithm for in-situ defect-detection in laser powder-bed fusion

4.1 Abstract

This chapter studies the development of a machine-learning algorithm to detect lack-of-fusion (LoF) porosity induced during laser powder bed fusion (LPBF). The detection algorithm is based on analyzing in-situ light intensity emitted from the melt pool during LPBF to not only predict the defect formation at a higher prediction rate more precisely but also analyze the real-time data stream faster than analytical methods. The integrated sensor used in this chapter is a commercial on-axial in-situ photodiode which was completely explained in Section 3.2.2. To this end, a Self-Organizing Map (SOM), an unsupervised machine learning algorithm, is thoroughly customized to classify disturbances in the light intensity signal, where the clustered disturbances are mapped with the geometrical feature and position of defects. To evaluate the proposed SOM algorithm, two sets of samples are designed: 1- samples with artificial micro-voids to mock the lack-of-fusion in the printed parts for assessing the sensor response and calibrating/optimizing the SOM algorithm and 2- samples with randomized pores induced normally during the process at different process parameters. The defects' position and size are correlated with the actual geometrical feature and position of defects identified through a post-processing computed tomography (CT) scanning. Thus, a volumetric segmentation method and confusion matrix are incorporated into the SOM-based algorithm to examine the true positive (TP) and true negative (TN) rates of defect prediction, as discussed in Section 3.2.6.1.

4.2 Methodologies and Experimental Setups

4.2.1 Design of experiments

Two sets of cubical-shape coupons with artificial and randomized pores were 3D printed. In the first set (R-series), artificial defects were embedded into the coupon samples, and in the second set (P-series), randomized pores induced from the lack-of-fusion (LoF) phenomenon were created when the energy density was decreased. All samples were fabricated with a stripe scan strategy of 67° rotation after each layer. Also, the laser spot size on the powder was 100 μm. Additionally, vertical and horizontal grooves were added to the geometry of samples for registering the pores' location in CT scan datasets, as demonstrated in Figure 3-1(a) (R-series) and Figure 4-1 (P-series).

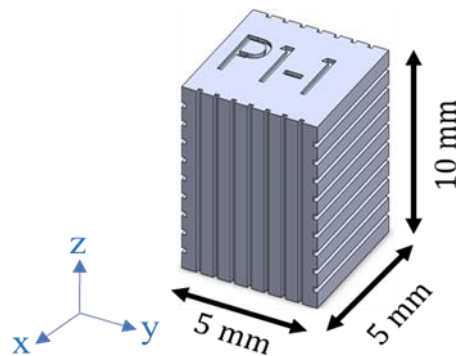


Figure 4-1: CAD model of a) R1-1 [40] () and b) P1-1

For each set, different process conditions were considered, as explained below.

4.2.1.1 Artificial defects

Four coupon samples of R-series (R2, R3, R4, and R5) were made with embedded micro-voids to mimic the LoF, as discussed previously (Section 3.2.1). These four samples from location 4 were selected to validate the SOM algorithm.

4.2.1.2 Randomized defects

This set of samples (P-series) was designed to create randomized LoF pores by decreasing the energy density. Firstly, cubical samples were designed with a size of $5 \times 5 \times 10$ (W \times L \times H) mm³. Then, samples were fabricated with different sets of print parameters, listed in Table 4-1. Four repetitions of each design were printed at different locations of the build plate (Figure 4-2). Sample P1 was fabricated with the standard print parameters used to obtain high-quality Hastelloy-X parts [48], thus considering as a control sample (Power= 200 W, hatching distance= 90 μ m, and speed= 1000 mm/sec). Samples P2, P3, and P4 were printed with three different laser powers (175, 150, and 125 W). Samples P5, P6, and P7 were fabricated with the variation of hatching distances (110, 130, and 150 μ m). Finally, samples P8, P9, and P10 were manufactured with different scanning speeds (1100, 1300, and 1500 mm/sec). As demonstrated in Table 4-1, the standard energy density (P1) is approximately 55.55 J/mm³. As a result, other samples were fabricated with low energy density to ensure that the randomized LoF pores are induced in the printed samples.

Table 4-1: Types and print parameters in P-series sample

Sample	Type	Power (Watt)	Hatching distance (μm)	Speed (mm/sec)	Layer thickness (μm)	The energy density (J/mm^3)
P1	Standard	200	90	1000	40	55.55
P2	Low power	175	90	1000	40	48.61
P3		150	90	1000	40	41.66
P4		125	90	1000	40	34.72
P5		High hatching distance	200	110	1000	40
P6	High hatching distance	200	130	1000	40	38.46
P7		200	150	1000	40	33.33
P8		200	90	1100	40	50.50
P9	High Speed	200	90	1300	40	42.73
P10		200	90	1500	40	37.03

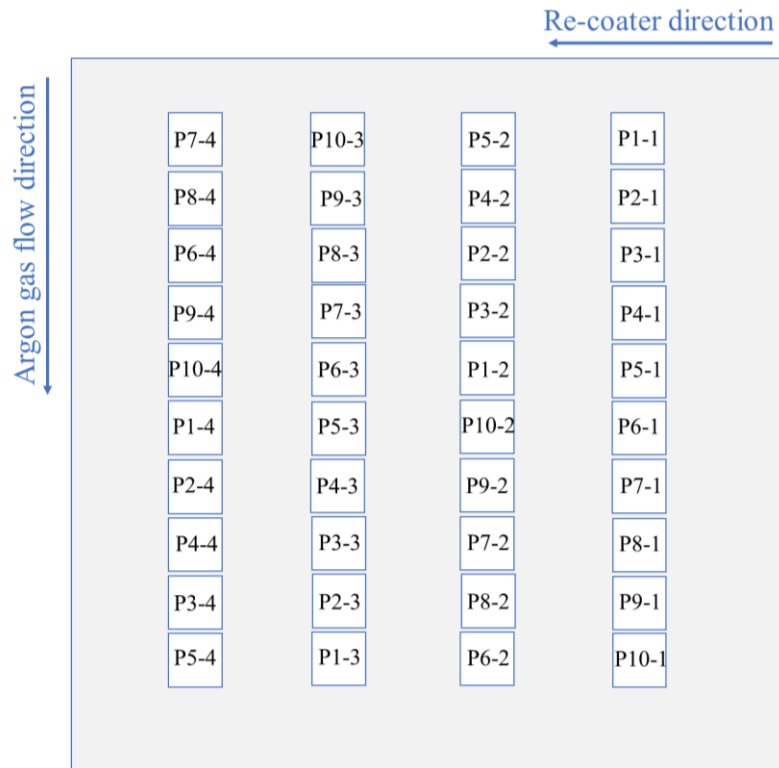


Figure 4-2: P-series sample layout on the build plate

The data collected from the printed samples with randomized defects were analyzed through the segmentation method, which was discussed previously (Section 3.2.6.1). After segmenting the data into the cubical voxels, the ground truth table was used to evaluate the detection algorithm.

In addition, three samples (T2, T3, and T4) with randomized defects were analyzed by the Absolute Limits (AL) algorithm in the EOSTATE MeltPool Monitoring software in Chapter 3. These three samples were also analyzed by the TP and TN rates to validate the performance of the AL algorithm. In this chapter, these samples were again analyzed by the proposed SOM algorithm to make a rational comparison between the performance of AL and SOM algorithms.

4.2.2 The clustering algorithm

In this study, the light intensity signal collected from the on-axial photodiode is analyzed to map its disturbance to the geometry to identify the pore position induced due to the lack-of-fusion. In Chapter 3, a threshold method was applied to predict the lack of fusion defects. Applying threshold algorithm resulted in the prediction of defects created by relative high hatching distance (150 μm) and high speed (1500 mm/sec) with the accuracy of approximately 70% and 72%, respectively, while the algorithm was not successful in predicting defects created with relatively low laser power (100 W). Unsuccessful prediction of defects could be due to the high sensitivity of the signal to print parameters, especially laser power. Hence, a more powerful algorithm should be customized to identify defects to increase the prediction rate of defects created by low power. On the other hand, parameters of threshold algorithms (e.g., threshold ranges and window length) need to be tuned/adjusted by users. Thus, the new algorithm should also be adaptive to remove the dependency of the algorithm on users' selection. For mentioned purpose, one of the potential methods is un-supervised clustering algorithms. Clustering analysis is a task to group the dataset based on their similarity. According to literature, K-means and agglomerative were applied to cluster in-situ data in LPBF; however, SOM (Self-Organized Map) has not been applied to data of LPBF. In this study, K-means and SOM were applied to in-situ photodiode data; however, since the result of SOM was more promising than K-means, only the SOM application will be reported here. The SOM generally is used to map the n-dimensional data into 2D/1D space and reduce the dimensions while the topological interrelationship between data is preserved [86], [87]. However, in this chapter, the SOM model is used to cluster the 1D intensity signal into different clusters. Then, each cluster is mapped with the geometry to identify the location of pores induced via the lack of fusion phenomenon. Additionally, since the in-situ photodiode data with the sampling frequency of 60 kHz would include more than five million data points in each layer for a regular small-size envelope of 25 \times 25 cm^2 when 80% of envelop area is solidified in each slice and process speed is in range of 1 m/s, thus, the customized SOM is ideally a proper platform to convert the big data into the smaller dataset.

The SOM works based on a neighborhood function where it maps the dataset by multiple steps [86], as demonstrated in Figure 4-3. In summary, the following steps are carried out in the SOM.

- 1- The initialization step: weights and biases are chosen randomly from uniform distribution.
- 2- The competition step: discriminant function is calculated given by [87]:

$$d_j(x) = \sum_{i=1}^D (x_i - w_{ji})^2 \quad (\text{Eq 3.1})$$

where x is a D -dimensional input space and w_{ji} is the connection weight between neurons i and j . At the end of the competition step, input space is mapped to the discrete output space by a simple competition process between neurons.

- 3- The cooperative step: winner neurons affect their neighboring neurons, similar to the human brain's neural network. So, lateral interaction or topological neighborhood effect is defined by [87]:

$$T_{j,I(x)} = \exp(-S_{j,I(x)}^2/2\sigma^2) \quad (\text{Eq 3.2})$$

where S_{ij} is the lateral distance between the winner neuron and its neighbor (j), and $I(x)$ is the index of the winner neuron. The topological neighborhood ($T_{j,I(x)}$) exponentially shrinks with time by σ .

- 4- The adaption step: weights are updated by [87]:

$$\Delta w_{ji} = \eta \cdot T_{j,I(x)}(t) \cdot (x_i - w_{ji}) \quad (\text{Eq 3.3})$$

where t is the iteration number and η is a learning rate and is not time-variant in this study.

- 5- The continuation step: the mapping process keeps returning to step 2 until the map stops changing.

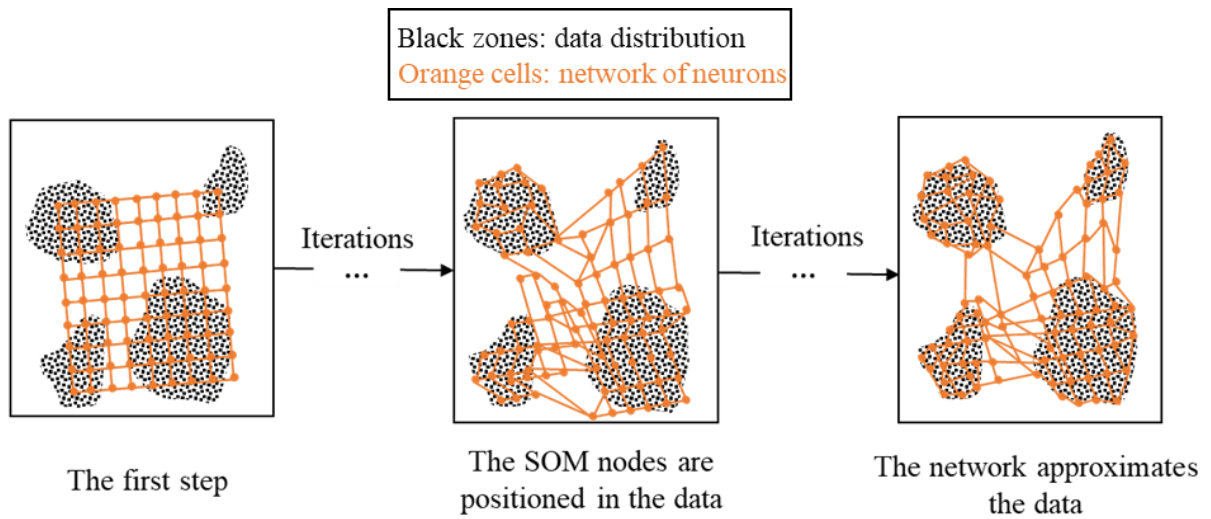


Figure 4-3: SOM concept and iterations to map nodes to the input space (redraw and adapted from [88])

Before applying the SOM, the number of clusters should be defined ($s \times s$ clusters), dictating the algorithm's output as s^2 clusters. For example, Figure 4-4(a) shows the neighbor weight distances among nine (1×9) clusters in which there is a spectrum of light to dark colors. Lighter and darker colors show cluster similarity and dissimilarity, respectively. Figure 4-4 (b) represents the population size of each cluster.

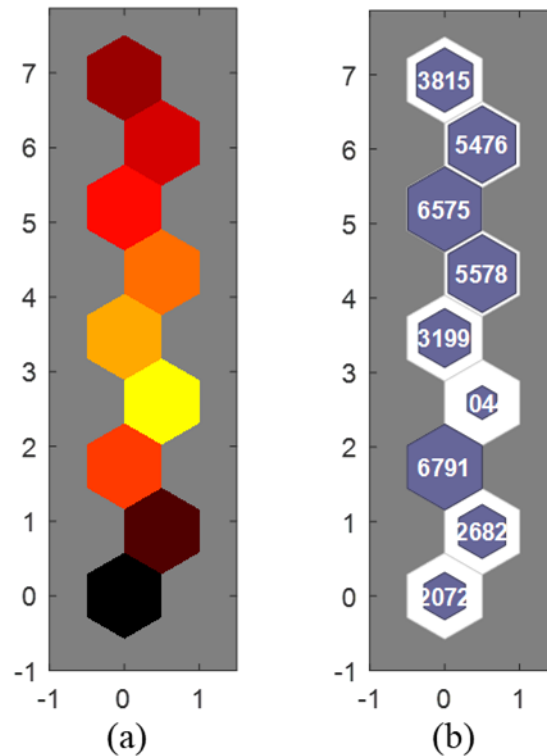


Figure 4-4: a) Neighbour weight distances and b) the population size of each cluster after applying the SOM with 1×9 clusters

The clustering using the SOM network adopts both 1-D and 2-D datasets. However, in this study, the SOM input is one dimension. The light intensity signal is a 1-D time series. As a result, applying SOM to 1-D data means clustering the signal into $1 \times N$ clusters. To assess the effect of the number of clusters on the prediction rate, a different number of dimensions/ clusters (5 to 10) is chosen and applied to the light intensity signal, where the results will be compared and discussed in 4.3.1.

4.2.3 Computed tomography (CT-Scanning)

Four R-series (R2, R3, R4, and R5), all T-series (T2, T3, and T4), and all P-series samples were micro-CT scanned (μ CT) to identify the position and distribution of actual pores. To compare the result with the result of Chapter 3, similar hardware (X-ray μ CT on Zeiss Xradia Versa 520 system) and software (Dragonfly Pro v4.0) were used for CT-Scanning the parts. The CT-Scan results of artificial and randomized defects are discussed in the following sections:

4.2.3.1 Artificial defects

The pores' diameter and location as well as the density of samples were identified through the μ CT imaging. The CT-scan analysis was carried out on samples R2- R5 in location 4 in the build plate. The front and top views of samples R2-4, R3-4, R4-4, and R5-4 are depicted in Figure 4-5 (a, e), Figure 4-5 (b, f), Figure 4-5 (c, g), and Figure 4-5 (d, h), respectively. It should be recognized that some pores were healed to the undetectable level during the fabrication according to the CT-scan analysis.

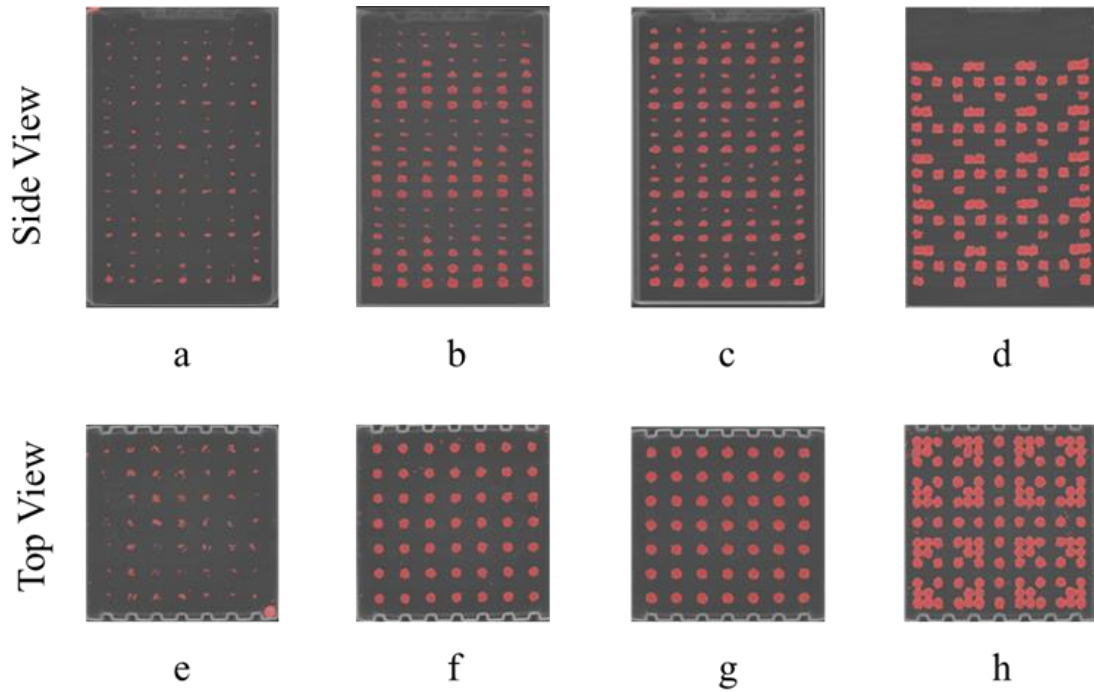


Figure 4-5: μ CT scan result of front view of a) R2, b) R3, c) R4, and d) R5 samples, and top view of e) R2, f) R3, g) R4, and h) R5 samples

4.2.3.2 Randomized defects

The pores' diameter, pores' location, and density of all samples were analyzed using the CT data. For instance, the CT results of P1- P10 samples printed in location 1 are presented in Figure 4-6 in which the front and top views of P-series samples are shown. Besides, the density of samples was measured, as demonstrated in Table 4-2.

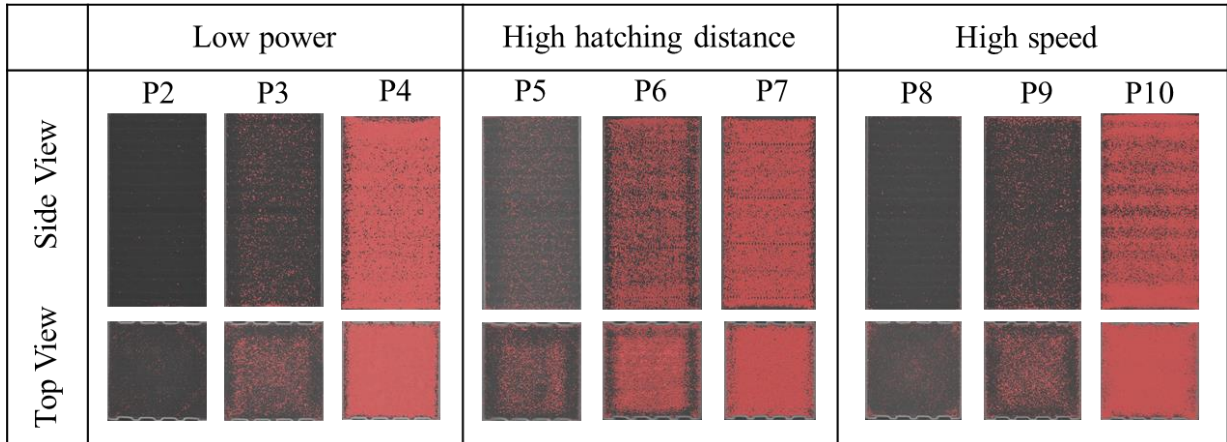


Figure 4-6: CT scan result of P-series sample

Table 4-2: Density of P-series sample

Sample #	P2				P3				P4			
Location	1	2	3	4	1	2	3	4	1	2	3	4
Density (%)	99.95	99.97	99.98	99.93	99.81	99.95	99.77	99.90	98.35	98.25	99.08	98.49
Sample #	P5				P6				P7			
Location	1	2	3	4	1	2	3	4	1	2	3	4
Density (%)	99.99	99.94	99.99	99.92	99.65	99.29	99.17	99.17	97.17	97.55	96.43	94.93
Sample #	P8				P9				P10			
Location	1	2	3	4	1	2	3	4	1	2	3	4
Density (%)	99.92	99.94	99.93	99.92	99.90	99.94	99.80	99.91	99.42	99.46	98.78	99.27

4.3 Results and discussion

4.3.1 Predicting porosity using SOM and comparing the result with CT-scanning

4.3.1.1 Artificial defects

- Clustering analysis

The goal of making artificial defects is to create voids with loosening powder particles that mimic LoF. Thus, the main analysis is carried out on the capping layer $n+1$ to identify the existence of defects in layer n . For example, Figure 4-7 (a) shows the geometrical position of artificial defects in layer n of sample R3 with a defect height of 160 μm and defect radius of 200 μm . The capping layer and the corresponding light intensity signal of layer $n+1$ are shown in Figure 4-7 (b and c), respectively. The SOM method (9 clusters) is applied to the light intensity signal of layer $n+1$ (Figure 4-7 (d)). After mapping each cluster to the geometry of the sample, the geometrical position of each cluster is shown

in Figure 4-7 (e). Figure 4-7 (e) indicates that the lower cluster (red color) corresponds to the pores' position (see the cluster shown on the right side of Figure 4-7 (e)). Thus, for the following analysis, the lower cluster is chosen as the main pore identifying cluster.

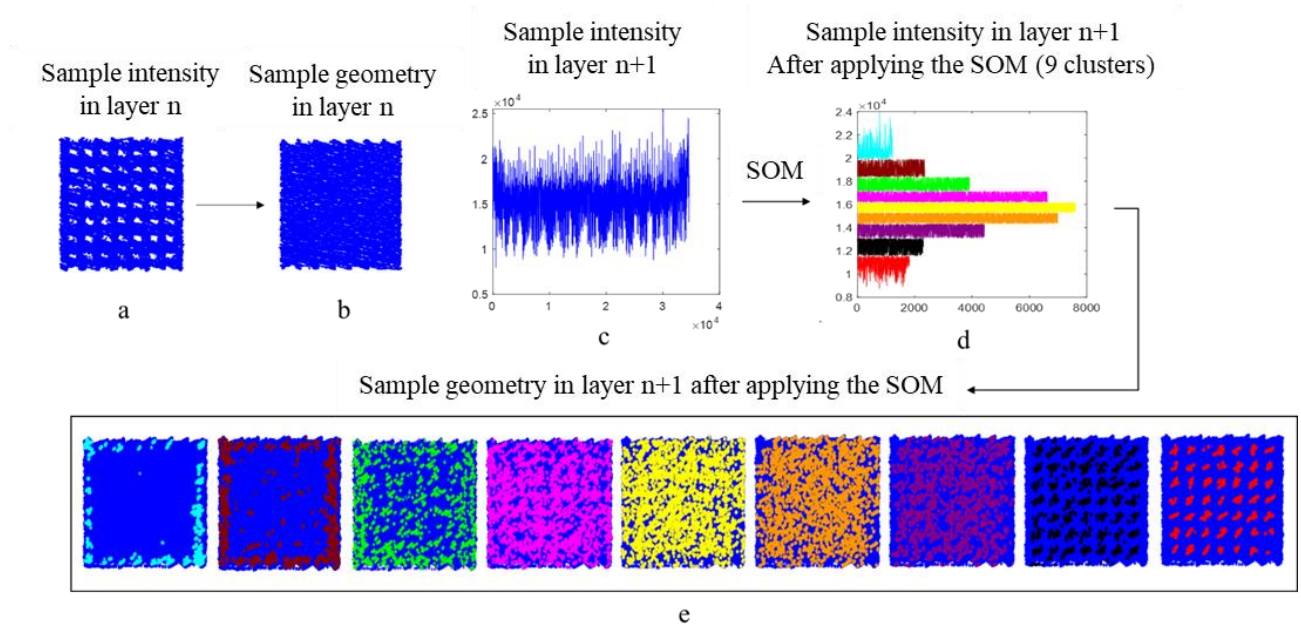


Figure 4-7: Defect detection procedure which demonstrated a) sample geometry with artificial defects in layer n , b) capping layer geometry of layer $n+1$, c) light intensity signal of capping layer on the layer $n+1$, d) light intensity signal of layer $n+1$ after applying the SOM with 1×9 dimensions, and e) capping layer geometry of layer $n+1$ after applying the SOM with 1×9 dimensions

The $1 \times N$ SOM, when $N=5, 6, 7, 8, 9, 10$, was applied to samples R2-R5. Table 4-3 shows the example of a comparison among different cluster dimensions. Additionally, iterations were first ranged in 100: 50: 500, then optimized and set to 200. The training was conducted in MATLAB R2020a.

Table 4-3: Applying SOM algorithms with 5, 6, 7, 8, 9 and 10 clusters to the on-axial photodiode signal to layer $n+1$ (sample R2: defect radius= 150 μm and defect height= 150 μm , sample R3: defect radius= 200 μm and defect height= 160 μm , sample R4: defect radius= 250 μm , and sample R5: defect radius= 200 μm , defect height= 200 μm , and defect distribution=5 \times 5)

Sample	Layer n Geometrical features	Layer $n+1$ Identified defects versus cluster dimensions					
		5	6	7	8	9	10
R2							
R3							
R4							
R5							

As seen in Table 4-3, six SOM cluster dimensions were applied to layer $n+1$ to assess the effect of the SOM dimensionality on the defect prediction rate. The 1 \times 5, 1 \times 6, and 1 \times 7 SOMs applied to the dataset resulted in a large number of undesired/unmatched red points compared to the 1 \times 8, 1 \times 9, and 1 \times 10 SOMs. Besides, in some samples (e.g., R3), the size of identified defects was obviously larger than the actual defects predicted by the 1 \times 5, 1 \times 6, and 1 \times 7 SOM. While the application of 1 \times 10 clusters results in fewer points mapped against the geometrical features of actual pores, several valuable points were not identified (see Table 4-3, sample R2). However, the 1 \times 8 and 1 \times 9 clusters result in better detection performance in terms of accuracy and effectiveness. Thus, the result of 1 \times 8 and 1 \times 9 SOMs are analyzed in which radius of each identified defect (red indicators in Table 4-3) is compared with the actual defect size in layer n . Table 4-4 represents the average radius of defects in layer n for all defects embedded in samples R2, R3, R4, and R5 and the average radius of identified defects in layer $n+1$ after applying 1 \times 8 and 1 \times 9 SOMs.

Table 4-4: Comparison between the average radius of identified defects after applying 1×8 and 1×9 SOMs in layer $n+1$ with the average radius of defects in layer n

Sample	Defect type	Designed defect size (μm)	Defect size in layer n (μm)	Identified indicator size in layer $n+1$ after applying 1×8 SOM (μm)	Identified indicator size in layer $n+1$ after applying 1×9 SOM (μm)
R2	Cylindrical	\emptyset , H=200	188±14	244±96	166±33
		\emptyset , H=150	135±32	168±44	138±10
		\emptyset , H=100	84±26	95±30	80±8
R3	Cylindrical	$\emptyset=200$, H=320	198±5	259±16	201±29
		$\emptyset=200$, H=280	178±14	231±13	181±6
		$\emptyset=200$, H=240	180±32	245±5	189±16
		$\emptyset=200$, H=200	170±24	230±23	172±17
		$\emptyset=200$, H=160	186±8	251±5	169±22
		$\emptyset=200$, H=120	177±17	237±9	183±12
R4	Spherical	$\emptyset=300$	199±11	252±13	173±6
		$\emptyset=250$	145±21	184±8	151±3
		$\emptyset=200$	132±7	153±12	125±9
R5	Cylindrical	\emptyset , H=200	183±3	242±17	192±4
		\emptyset , H=200	179±12	237±16	182±11
		\emptyset , H=200	187±8	250±4	175±21

As listed in Table 4-4, the defect radius in layer n had an approximately similar size to its design by considering the standard deviation. However, a comparison between the radius of identified defects in layer $n+1$ after applying 1×8 and 1×9 SOMs showed that the size of defects identified by 1×8 SOM was larger than the actual size of the defects and its corresponding number after applying 1×9 SOM. For example, in sample R2 for cylindrical defects with the designed size of \emptyset , H=200 (μm), the size of the actual defect in layer n was 188±14 (μm), whereas the size of identified defects by 1×8 SOM in layer $n+1$ was 244±96 (μm), which was larger than its underneath pore. On the other hand, the result of 1×9 SOM resulted in the size of 166±33 (μm), which was more compatible with the size of its underneath pore. A similar conclusion was drawn by comparing all sizes of defects listed in Table 4-4. As a result, 1×9 SOM was selected for the next step of the study.

It should be added that similar to the previous study of authors [4], after applying 1×9 SOM on the light intensity signal, less than three adjacent indicators were considered as noise, and more or equal than three adjacent indicators were considered as a defective area in the next step of the analysis.

- Comparison between CT-scan and SOM algorithm

After removing the healed pores from the analysis discussed in Section 4.2.3.1, SOM defect detection results are listed in Table 4-5.

Table 4-5: The percentage of identification for each size of the defect in samples R2-R5

Sample	Defect type	Defect size (μm)	Distribution of defects in one layer of sample	Percentage of artificial pore identified by the 1×9 SOM model
R2	Cylindrical	$\emptyset, H=200$	7×7	100
		$\emptyset, H=150$	7×7	100
		$\emptyset, H=100$	7×7	100
R3	Cylindrical	$\emptyset=200, H=320$	7×7	100
		$\emptyset=200, H=280$	7×7	100
		$\emptyset=200, H=240$	7×7	100
		$\emptyset=200, H=200$	7×7	100
		$\emptyset=200, H=160$	7×7	100
		$\emptyset=200, H=120$	7×7	100
R4	Spherical	$\emptyset=300$	7×7	100
		$\emptyset=250$	7×7	100
		$\emptyset=200$	7×7	100
R5	Cylindrical	$\emptyset, H=200$	5×5	100
		$\emptyset, H=200$	9×9	100
		$\emptyset, H=200$	8×8	100

Table 4-5 revealed that all artificial pores were predicted by the 1×9 SOM algorithm. In Section 3.3, the AL could not identify such defects. AL was applied with the fixed upper and lower threshold ranges for all parts printed at different positions of the build platform, resulting in poor detection of pores in some locations. However, since the SOM can cluster the datasets adaptively, the datasets were not clustered equally, leading to 100% identification of artificial pores. For example, in sample R5 (Figure 4-8), all artificial defects were detected by the SOM (Figure 4-8(b)), whereas most artificial pores could not be detected by the AL (Figure 4-8(a)) based on the result of CT-scan (Figure 4-8(c)).

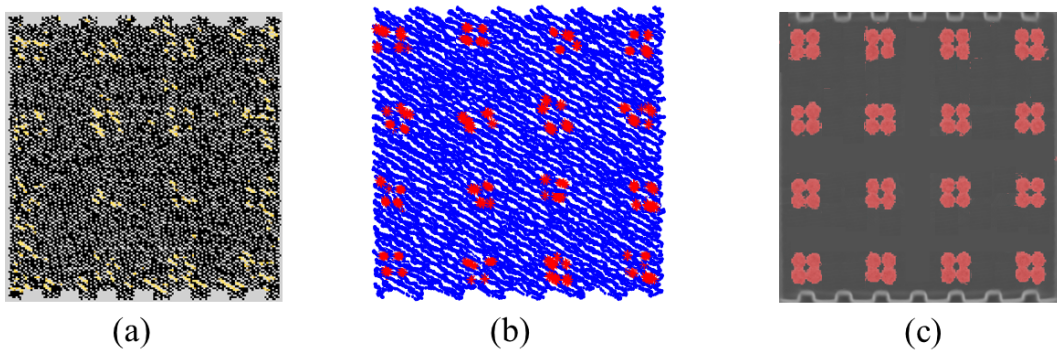


Figure 4-8: Defect position identified by a) AL-EOSTATE, b) SOM, and c) CT-scan in sample R5 with the distribution of 8×8

4.3.1.2 Randomized defects

The datasets of samples with randomized defects (P-series) were analyzed by the 1×9 SOM, where the corresponding parts were CT-scanned. The results of both steps were compared by the confusion matrix to obtain the TP and TN rates. The following sections disclose the TP and TN rates for the samples printed with different laser powers, hatching distances, and process speeds.

- Effect of laser power

Samples P2, P3, and P4 were printed with low energy density provided by low laser powers (175, 150, and 125 W). Table 4-6 compares the results of defect detection by the 1×9 SOM and the actual position of pores based on the TP and TN rates.

Table 4-6: Averaged TP and TN rates by comparing 1×9 SOM algorithm and CT-Scan for samples P2, P3, and P4

P2								
Location	1		2		3		4	
Classification	TP	TN	TP	TN	TP	TN	TP	TN
Averaged Detection Rate (%)	82	71	73	78	61	77	85	86
P3								
Location	1		2		3		4	
Classification	TP	TN	TP	TN	TP	TN	TP	TN
Averaged Detection Rate (%)	86	71	84	78	80	78	92	71
P4								
Location	1		2		3		4	
Classification	TP	TN	TP	TN	TP	TN	TP	TN
Averaged Detection Rate (%)	94	72	86	78	84	79	91	74

Table 4-6 lists TN and TP values at each location of the built plate. The overall average values and the corresponding standard deviation for four printed locations are as follows:

- Sample P2 at four locations: TP rate: 75±9% and TN rate: 78±5%
- Sample P3 at four locations: TP rate: 85±4.3% and TN rate: 75±3%
- Sample P4 at four locations: TP rate: 89±3% and TN rate: 76±3%

The results showed that the TP rate increases by decreasing the laser power (from samples P2 to P4). Additionally, Table 4-2 indicated that the density drops when the laser power decreases, implying that the number of pores increases. On the other hand, TN rates of these three samples showed that the 1×9 SOM performed more and less the same when it comes to the TN identification. Therefore, the 1×9 SOM algorithm is able to predict the randomized defects induced due to variation in laser power with the TP rate of more than %75. However, in Section 3.3.2.3, analyzing sample T2, printed with a low

power (P= 100 W) using the AL algorithm, resulted in a very low prediction (TP rate< 30%); however, sample T2 was again analyzed in this study by 1×9 SOM algorithm, and the results were compared with the CT-Scan, as shown in Table 4-7.

Table 4-7: TP and TN raters by comparing the 1×9 SOM algorithm and CT-Scan for sample T2

Performance	Location 1	Location 2	Location 3	Location 4	Location 5	Location 6
TP (%)	90	91	91	88	92	91
TN (%)	78	80	88	89	87	89

According to Table 4-7, pores induced in sample T2 could identify with the TP rate of approximately 90±1% and TN rates of 85±4%, which indicated the higher accuracy of the SOM algorithm compared to the AL for identifying pores induced by the deviation in the low power (Section 3.3.2.3).

- Effect of hatching distance

Samples P5, P6, and P7 were printed with low energy density provided by a high hatching distance (110, 130, and 150 μm). After applying the 1×9 SOM, the results of defect detection were compared with the CT-scan data. Then, the TP and TN rates were calculated, as listed in Table 4-8.

Table 4-8: TP and TN raters by comparing SOM algorithm and CT-Scan for samples P5, P6, and P7

P5								
Location	1		2		3		4	
Classification	TP	TN	TP	TN	TP	TN	TP	TN
Averaged Detection Rate (%)	82	72	80	75	61	86	79	73
P6								
Location	1		2		3		4	
Classification	TP	TN	TP	TN	TP	TN	TP	TN
Averaged Detection Rate (%)	76	73	62	85	65	79	79	84
P7								
Location	1		2		3		4	
Classification	TP	TN	TP	TN	TP	TN	TP	TN
Averaged Detection Rate (%)	72	88	75	86	67	86	75	82

The overall average values and the corresponding standard deviation for four printed locations are as follows:

- Sample P5 at four locations: TP rate: 76±8 % and TN rate: 76±6%
- Sample P6 at four locations: TP rate: 70±7% and TN rate: 80±4%
- Sample P7 at four locations: TP rate: 72±3% and TN rate: 86±2%

TP and TN rates showed more than approximately 70% and 80% true predictions for samples P5, P6, and P7, respectively; however, the TP rates of these samples were 1%-15% less than the TP rates in samples fabricated with low laser powers. Additionally, sample P7 was printed with similar parameters to sample T3 in Section 3.3.2.3. Sample T3 was also analyzed by the SOM. Then, the identified defects were compared with the CT-Scan result through a confusion matrix. The TP and TN rates are demonstrated in Table 4-9.

Table 4-9: TP and TN raters by comparing SOM algorithm and CT-Scan for sample T3

Performance	Location 1	Location 2	Location 3	Location 4	Location 5	Location 6
TP (%)	78	74	71	74	72	72
TN (%)	87	86	80	87	84	88

The average and standard deviation for 6 different locations for sample T3 resulted in:

- 1- SOM: TP rate= $74\pm 2\%$ and TN rate= $85\pm 3\%$, and
- 2- AL: TP rate= $74\pm 1\%$ and TN rates= $53\pm 2\%$

By comparing the outcomes of the AL-EOSTATE and SOM, the TP rate was not changed significantly; however, the SOM exhibited a better performance to identify true negative cells by which the TN rate has increased up to 31%, indicating a higher precision for the SOM algorithm compared to the AL-EOSTATE.

- Effect of process speed

Samples P8, P9, and P10 were printed with low energy densities carried by high process speeds (1100, 1300, and 1500 mm/sec). After applying the SOM algorithm, TP and TN rates were calculated based on the CT-scan results, as demonstrated in Table 4-10.

Table 4-10: TP and TN raters by comparing SOM algorithm and CT-Scan for samples P8, P9, and P10

P8								
Location	1		2		3		4	
Classification	TP	TN	TP	TN	TP	TN	TP	TN
Averaged Detection Rate (%)	64	69	64	73	66	78	90	93
P9								
Location	1		2		3		4	
Classification	TP	TN	TP	TN	TP	TN	TP	TN
Averaged Detection Rate (%)	73	82	61	85	75	85	73	82
P10								
Location	1		2		3		4	
Classification	TP	TN	TP	TN	TP	TN	TP	TN
Averaged Detection Rate (%)	75	87	76	90	78	89	76	86

By analyzing the average and standard deviation of TP and TN rates on four printed locations, the following results are calculated:

- Sample P8 at four locations: TP rate: $71\pm 11\%$ and TN rate: $78\pm 9\%$
- Sample P9 at four locations: TP rate: $71\pm 6\%$ and TN rate: $84\pm 2\%$
- Sample P10 at four locations: TP rate: $76\pm 1\%$ and TN rate: $88\pm 2\%$

The results confirmed that the TP and TN rates increased when more pores were induced due to the high process speed (i.e., sample P10). Additionally, Table 4-10 indicated that the randomized lack-of-fusion pores created by increasing the speed could be identified by applying the SOM algorithm with the TP rate of $\sim 71\%$ and the TN rate of $\sim 78\%$.

In addition to samples P8, P9, and P10, sample T4 was analyzed by the SOM algorithm. Performance of the SOM was evaluated by the CT-scan through the confusion matrix, as represented in Table 4-11.

Table 4-11: TP and TN raters by comparing SOM algorithm and CT-Scan for sample T4

Performance	Location 1	Location 2	Location 3	Location 4	Location 5	Location 6
TP (%)	78	75	76	79	79	78
TN (%)	86	90	89	86	86	86

The average and standard deviation of sample T4 averaged at all six locations result in:

- 1- SOM: TP rate= $78\pm 1\%$ and TN rate= $87\pm 2\%$, and
- 2- AL: TP rate= $75\pm 1\%$ and TN rates= $68\pm 4\%$

The result indicates that the TP is almost similar for both the SOM and AL-EOSTATE. On the other hand, the TN increases from 67% in the AL-EOSTATE to 87% in the SOM.

The comparison of the AL-EOSTATE (Chapter 3) and SOM asserted that the SOM exhibits better performance when identifying randomized defects induced in parts printed by LPBF. On the other hand, these two algorithms could compare based on their computational time. These two algorithms were compared in terms of the computational elapsed time required for one individual layer of a part with a cross-section area of $5 \times 5 \text{ mm}^2$. For example, Table 4-12 represents the analysis time of sample P2-1 in layers 1, 30, 60, 90, 120, 150, 180, 210, and 240 by applying the AL and SOM algorithms. According to Table 4-12, one layer of sample P2-1 was analyzed in less than 1 second by the SOM and in approximately 5 seconds by the AL, which showed $\sim 86\%$ improvement in the computational time. It should be noted that the SOM computational script was run in a PC with Intel(R) Core (TM) i7-7700 CPU @ 3.60 GHz, whereas the AL computational procedure was run in PC with Intel(R) Xeon(R) CPU

E5-2680 v4 @ 2.40 GHz (2 processors). As a result, with the current hardware, the SOM algorithm is more appropriate for dealing with the process in real-time.

Table 4-12: Computational time of AL and SOM for sample P2- 1 for layers 1, 30, 60, 90, 120, 150, 180, 210, and 240

Sample	Layer #	Sample cross section area (mm ²)	AL computational time (seconds)	SOM computational time (seconds)	Improvement percentage (%)
P2-1	1	5 × 5	5.49	0.792	85.57
P2-1	30	5 × 5	5.31	0.764	85.61
P2-1	60	5 × 5	5.36	0.754	85.93
P2-1	90	5 × 5	5.29	0.772	85.41
P2-1	120	5 × 5	5.40	0.752	86.07
P2-1	150	5 × 5	5.26	0.751	85.72
P2-1	180	5 × 5	5.25	0.797	84.82
P2-1	210	5 × 5	5.16	0.785	84.79
P2-1	240	5 × 5	5.25	0.882	83.20

Nevertheless, the SOM has shown promising outcomes in terms of computational speed and also predication rates; however, the SOM has not been able to fully provide a remedy for the detection dependency on the parts' location in the build plate. For example, the TP rates in sample P8 in Locations 1, 2, and 3 were not as high as the TP rate in Location 4 (see Table 4-10), which was drawn a similar conclusion that the position of samples in the build plate could affect the accuracy and precision of detection [4], [82], [83]. One suggestion to tackle this challenge would be developing a new intensity correction factor which will be discussed in the future study.

4.4 Summary

In this chapter, the commercial on-axial photodiode installed in the LPBF machine was used to collect light intensity signals from the melt pool. The collected intensity signal was analyzed by the Self-Organizing Map (SOM) algorithm to predict the porosity induced due to the lack-of-fusion during the LPBF process. Two sets of studies that included artificial and randomized defects were then designed and embedded in the coupon samples. Artificial defects were used to customize the SOM algorithm to predict the actual defects by comparing the prediction with the design and CT-scan. Randomized defects were used to evaluate the customized algorithm's performance. The randomized defects predicted by the SOM algorithm were compared with the actual defects identified by the CT-scan through the segmentation approach and confusion matrix. Also, the SOM results were compared with the Absolute Limits (AL) algorithm, which was discussed in Chapter 3.

Chapter 5. Development of an intermittent controller for LPBF

5.1 Abstract

This chapter explains the methodology and validation results of an intermittent close-loop control system in which the laser power is intelligently increased in segmental zones of the successive layer and on top of the defected zones for healing lack-of-fusion (LoF) defects in a part created during the LPBF process. To this end, defects identified by the Self-Organizing Map (SOM) algorithm (discussed in Chapter 4) are clustered in each area of 1 mm² using the K-means algorithm. Then, the targeted zone around the center of each cluster is optimized as the position at which the laser power is increased in the successive layer to heal the induced defects. To identify the optimum laser power value, various artificial defects are embedded in the coupon samples, and their capping layer is manufactured by increasing the laser power in order to minimize the size and number of artificial defects. Then, based on the optimum power and defect size, knowledge-based rules are defined to calculate the new laser power. The new laser power value is calculated in a Laser Correction File (LCF), after the deposition of each layer and before starting the new layer. Additionally, a Message Queuing Telemetry Transport (MQTT) broker is used to connect the data acquisition system, the defect detection algorithm, the LCF calculation algorithm, and the actuator (e.g., laser in this case). Finally, two new sets of experiments are designed and manufactured to evaluate the performance of the control system.

5.2 Methodologies and Experimental Setups

5.2.1 The detrending algorithm

5.2.1.1 The number and coverage area of defect indicators based on their size

After applying the Self-Organizing Map (SOM) algorithm to identify the locations of defects, the number of indicators on the capping zone (equal to defect size) on each defect is calculated. Figure 5-1 demonstrates one example of the procedure. Figure 5-1 (a) shows the 2D image of the last layer (layer n) incorporating artificial cylindrical defects with the size of \emptyset , $H=200\ \mu\text{m}$ from the R2 sample (refer to Section 3.2.1). Figure 5-1 (b) represents the positions of indicators in layer $n+1$ after applying a defect detection algorithm on the successive layer of artificial defects (layer $n+1$). To identify the number of indicators on top of each defect, the capping zone on each defect is analyzed based on the actual size of the defects.

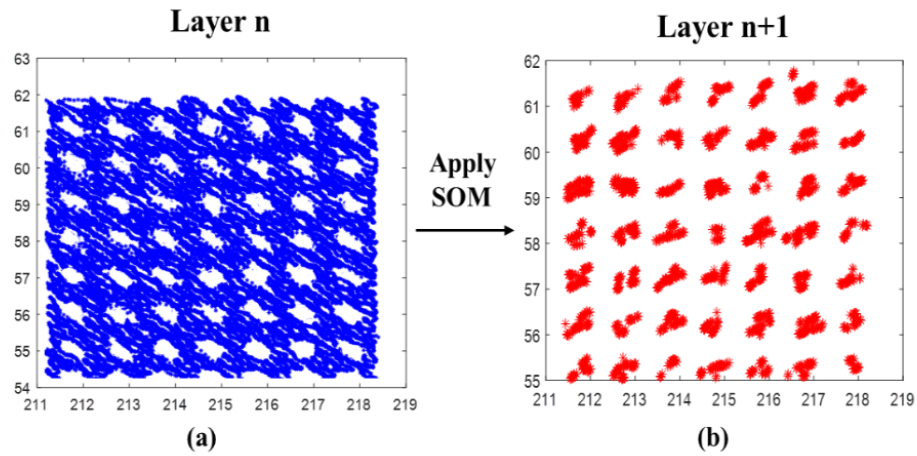


Figure 5-1: One example of the defect detection procedure in which a) a layer with artificial defects with the size of $200\ \mu\text{m}\times 200\ \mu\text{m}\times 200\ \mu\text{m}$ and b) the positions of defects after applying the SOM algorithm on the capping layer on artificial defects in Sample R2

The investigation is applied to the artificial defects of samples R2, R3, and R4 for all eight locations (Figure 3-3(a)) to shed some light on repeatability. Thus, the following numbers of defects are considered, as listed in Table 5-1:

- 1- 2325 artificial defects for each size of defects embedded in sample R2 (\emptyset , $H=200\ \mu\text{m}$, \emptyset , $H=150\ \mu\text{m}$, and \emptyset , $H=100\ \mu\text{m}$),
- 2- 1176 artificial defects for each size of defects embedded in sample R3 ($\emptyset=200\times H=320$, $\emptyset=200\times H=280$, $\emptyset=200\times H=240$, $\emptyset=200\times H=200$, $\emptyset=200\times H=160$, and $\emptyset=200\times H=120$), and
- 3- 2325 artificial defects for each size of defects embedded in sample R4 ($\emptyset=400\ \mu\text{m}$, $\emptyset=300\ \mu\text{m}$, and $\emptyset=200\ \mu\text{m}$).

Table 5-1: Calculation of numbers of artificial defects in Samples R2, R3, and R4

Sample	Type of defects	Size of defects (μm)	Number of locations	Numbers of defects in one location	Total numbers of defects
R2	Cylindrical	Ø, H=200	8	294	2325
		Ø, H=150		294	2325
		Ø, H=100		294	2325
R3	Cylindrical	Ø=200, H=320	8	147	1176
		Ø=200, H=280		147	1176
		Ø=200, H=240		147	1176
		Ø=200, H=200		147	1176
		Ø=200, H=160		147	1176
		Ø=200, H=120		147	1176
R4	Spherical	Ø=300	8	294	2325
		Ø=250		294	2325
		Ø=200		294	2325

By calculating the number of indicators on the capping zones on defects and applying average and standard deviation on the number of indicators, the results are summarized in Table 5-2.

Table 5-2: Average and standard deviations of numbers of indicators in Samples R2, R3, and R4 in the capping layer and defect zones based on the size

Sample	Type of defects	Size of defects (μm)	Average and standard deviations of the number of indicators
R2	Cylindrical	Ø, H=200	30 ± 2
		Ø, H=150	26 ± 2
		Ø, H=100	23 ± 3
R3	Cylindrical	Ø=200, H=320	35 ± 1
		Ø=200, H=280	33 ± 1
		Ø=200, H=240	31 ± 2
		Ø=200, H=200	30 ± 1
		Ø=200, H=160	28 ± 2
		Ø=200, H=120	26 ± 2
R4	Spherical	Ø=300	33 ± 2
		Ø=250	29 ± 3
		Ø=200	25 ± 1

Table 5-2 confirmed that the number of identified indicators increased by increasing the size of artificial defects. However, the number of indicators in sample R4 was less than its corresponding number in other samples, which could be due to its defect geometry. For example, indicators' number in sample R4 with the defect size of Ø=200 μm was approximately 25; however, in sample R2, the similar size of defects resulted in 30 indicators. Therefore, according to the shape of lack-of-fusion defects, which is more similar to a cylinder, the results of samples R2 and R3 are used for the next step of this study. It should also be noted that if the control system could heal cylindrical defects, it could definitely heal spherical defects with the same radius.

Based on Table 5-2, detecting any zone filled by more than 20 indicators (considering standard deviation) could be corresponding to the defect larger than 100 μm . According to Table 5-2, four groups are defined to correlate the number of indicators to the potential size of defects, as listed in Table 5-3.

Table 5-3: The potential size of defects based on the identified indicators

Number of indicators	The potential size of defects (μm)
>34	>300
30-34	200- 300
25-30	100- 200
20-25	~100

After detecting the indicators in each $1\text{ mm} \times 1\text{ mm}$, they are clustered by the K-means algorithm as one defect. For instance, Figure 5-2 demonstrates one example of applying the SOM algorithm on layer $n+1$ for detecting defect positions (Figure 5-2. a) and applying the K-means algorithm (Figure 5-2. b).

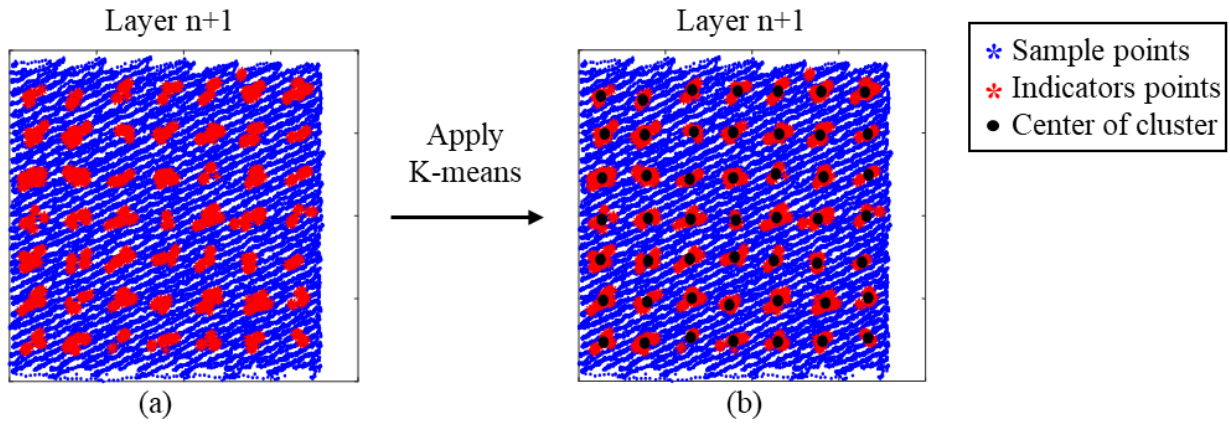


Figure 5-2: One example of a) applying the SOM algorithm on the capping layer on artificial defects to highlight the positions of defects shown by red colour and b) identifying the center of each cluster by K-means algorithm (artificial defects size is $200\ \mu\text{m} \times 200\ \mu\text{m}$ embedded in Sample R2)

After calculating the center of each cluster and finding the number of indicators in each cluster, two scenarios should be considered based on Table 5-3:

- 1- A cluster includes less than 20 indicators \rightarrow the cluster is identified as normal.
- 2- A cluster includes more than 20 indicators \rightarrow the cluster is identified as abnormal.

In the abnormal case, the number of indicators within each cluster specifies the actual size of defects based on Table 5-3.

Besides the number of indicators discussed above, the area covered by each cluster was another factor to analyze. As observed in Figure 5-2, the geometry of the cluster of indicators was not symmetric,

which might be due to the hatching direction. Thus, the maximum radius of each cluster from X (left to right) and Y (top to bottom) is measured. Then, the average and standard deviation of the maximum radius of all clusters are calculated and listed in Table 5-4 based on the size of defects.

Table 5-4: Average and standard deviations of maximum radius of X and Y directions of clusters in Samples R2 and R3 in the capping area on defective zones based on defect size

Sample	Type of defects	Size of defects (μm)	Average and standard deviations of maximum radius of X direction (mm)	Average and standard deviations of maximum radius of Y direction (mm)
R2	Cylindrical	$\emptyset, H=200$	0.29 ± 0.01	0.27 ± 0.02
		$\emptyset, H=150$	0.28 ± 0.06	0.22 ± 0.07
		$\emptyset, H=100$	0.22 ± 0.08	0.18 ± 0.09
R3	Cylindrical	$\emptyset=200, H=320$	0.28 ± 0.03	0.20 ± 0.04
		$\emptyset=200, H=280$	0.27 ± 0.02	0.13 ± 0.03
		$\emptyset=200, H=240$	0.27 ± 0.03	0.24 ± 0.08
		$\emptyset=200, H=200$	0.25 ± 0.02	0.18 ± 0.02
		$\emptyset=200, H=160$	0.26 ± 0.02	0.16 ± 0.05
		$\emptyset=200, H=120$	0.25 ± 0.03	0.17 ± 0.04

Table 5-4 indicated that even by changing the defect size, areas covered by the cluster of indicators had approximately similar radius. For example, in Sample R2 for defect size of $\emptyset, H=200 \mu\text{m}$ and $\emptyset, H=150 \mu\text{m}$, the maximum radius of clusters in X direction was approximately 0.29 mm. Thus, the maximum radius of indicators' clusters was almost in the same range and between 0.21 (mm) to 0.31 (mm) in X-direction and between 0.11 (mm) to 0.29 (mm) in Y-direction. Thus, the maximum radius of 0.3 mm was assumed for the next step in which a $0.6 \times 0.6 \text{ (mm}^2\text{)}$ square (0.3 from the center to each direction) was considered around the center of each cluster. For instance, Figure 5-3 shows the $0.6 \times 0.6 \text{ (mm}^2\text{)}$ square around the center of each cluster in layer $n+1$ printed on top of layer n with defect size of $\emptyset, H=200 \text{ (}\mu\text{m)}$.

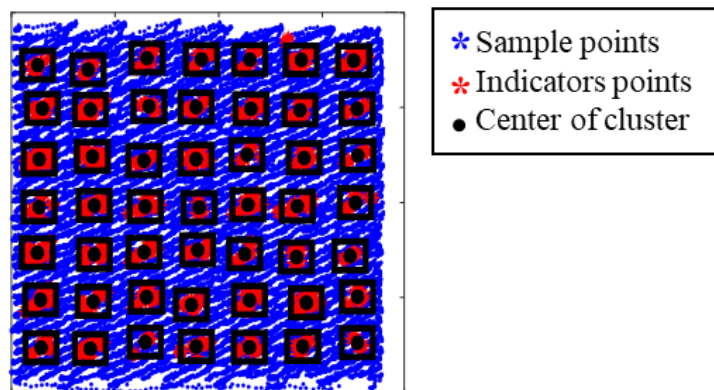


Figure 5-3: Considering a square with a size of $0.6 \times 0.6 \text{ mm}^2$ around the center of clusters in layer $n+1$ printed on top of layer n with defect size of $\emptyset, H=200 \text{ (}\mu\text{m)}$

Figure 5-3 visualized that a square with a side length of 0.6 (mm) around the cluster's center could cover a defective area. Thus, a 0.6×0.6 (mm²) square was chosen as an area where the laser power will be increased. However, the optimum laser power should be identified, which will be discussed in Sections 5.3.1 and 5.5.1. Next, to change the laser power in a square area of 0.6×0.6 (mm²), the following procedure is explained in Section 5.2.1.2.

5.2.1.2 Gridding the build plate into 2500× 2500 cells

As discussed in Chapter 4, the minimum size of identified defects was 100 μm. Thus, the build plate of 25×25 cm² was gridded into 2500×2500 cells with a size of 100 μm×100 μm. These 2500×2500 cells were considered in one table named Laser Correction File (LCF). The LCF was defined to contain information about the laser powers. As a result, each cell of LCF included the laser power value, which could vary from cell to cell.

5.2.1.3 Choosing a programming environment for collecting data, applying the defect detection algorithm, and calculating the LCF

Two programming environments are tested to gather real-time data, apply data correction and defect detection algorithms, and calculate the LCF table. These environments are MATLAB 2020a and LabVIEW 2020, which are compared based on their processing speed. The computational time of each programming environment is listed in Table 5-5, which shows the time of data acquisition, data correction, defect detection, and LCF calculation for one layer of the print.

Table 5-5: Comparing the computational time of MATLAB and LabVIEW

Environment	Computational time (seconds)
MATLAB	0.913
LabVIEW	~ 9

According to Table 5-5, LabVIEW resulted in slow processing time which is due to the lack of the SOM built-in function in LabVIEW. Thus, the SOM algorithm was manually developed in LabVIEW that had not been optimized compared to built-in functions. On the other hand, since MATLAB processing time was good enough for analyzing data and creating the LCF, MATLAB was chosen for the next step of this study, instead of optimizing the code in the LabVIEW environment.

5.2.1.4 Communicating between data acquisition, the defect detection algorithm, and the actuator

As discussed in Section 5.2.1.3, to collect real-time data, apply the defect detection algorithm, and calculate the LCF, MATLAB 2020a was used. Thus, the new LCF is calculated in MATLAB and should be transferred to the actuator (laser), which is controlled by the PLC system of the LPBF machine (the name is confidential; it is so-called EOS-Controller). To connect MATLAB to the EOS-Controller, the Message Queuing Telemetry Transport (MQTT) broker is used. The MQTT broker is a publish-subscribe network protocol that transports messages between devices [89]. The below procedure was used in this study:

- 1- EOS-Controller publishes the layer number, simultaneously MATLAB subscribes the message, and MATLAB starts collecting data from the current layer of the print,
- 2- As soon as EOS-Controller publishes another notification message which shows a layer of print is finished, MATLAB stops the data acquisition of the current layer and starts applying geometry and intensity corrections and defect detection algorithm on the collected data, then MATLAB calculates and publishes the LCF (a table with 2500×2500 cells) to the MQTT broker before exposure of the next layer, and
- 3- EOS-Controller subscribes to the LCF and changes the laser power of the next layer based on the new LCF file.

The LCF is transferred as a single-byte character encoding of the Latin alphabet (Windows-1252) to minimize communication speed. For example, the nominal laser power in this study is 200 W which corresponds to € in Windows-1252 format.

5.3 Design of experiments

5.3.1 Identifying the optimum amount of laser power to heal defects

Four cubical-shaped coupon samples (N1, N2, N3, and N4) with seeded artificial defects were designed. Samples N1 and N2 with a size of 5×5×10 (W×L×H) mm³ and samples N3 and N4 with a size of 5×5×5 (W×L×H) mm³ were fabricated, as shown in Figure 5-4. All of the samples were 3D-printed with a similar material (Hastelloy-X), scan strategy, and laser spot size as discussed in Sections 3.2.1 and 4.2.1. Also, vertical and horizontal rectangle-shape grooves were added to the geometry of samples to ease identifying the location of pores in the CT scan analysis.

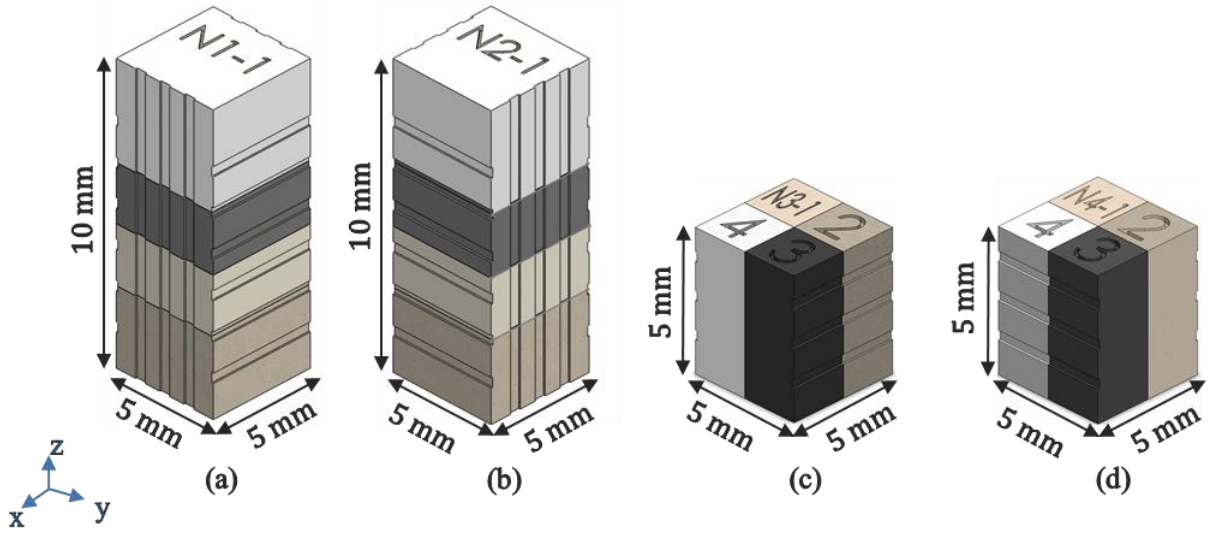


Figure 5-4: CAD model of Samples: a) N1, b) N2, c) N3, and d) N4

Each sample was segmented into four parts (P1, P2, P3, and P4). In each part, three sizes of cylindrical defects were embedded, as demonstrated in Figure 5-5.

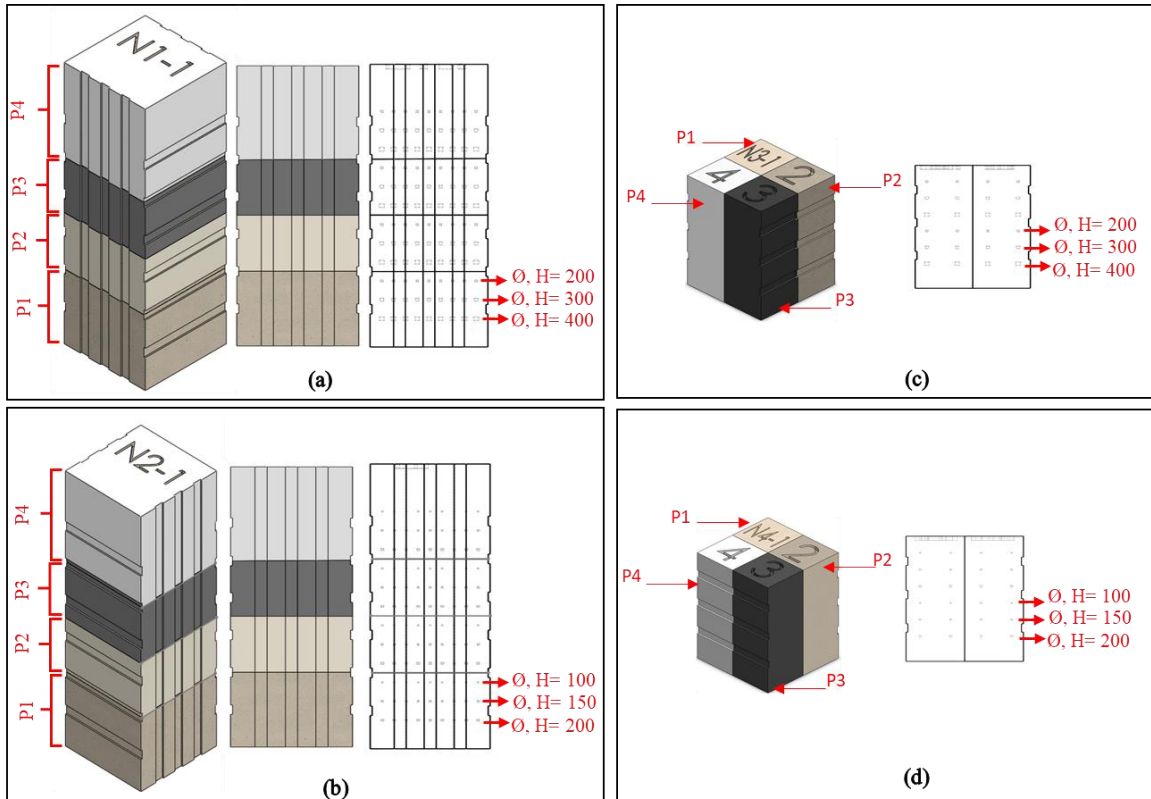


Figure 5-5: 3D and 2D cross-sections of samples showing the distribution of the artificial defects in Samples: a) N1, b) N2, c) N3, and d) N4.

Four repetitions of each coupon were designed, labeled, and printed at different locations of the build plate, as shown in Figure 5-6. Figure 5-6(a) demonstrates the samples layout on the build plate, and Figure 5-6(b) displays the printed parts. All samples were fabricated with a hatching distance of 90 μm , a layer thickness of 40 μm , and a laser speed of 1000 mm/sec; however, the laser power varied during the part fabrication. The laser power of all layers of the print, except the capping layer on the artificial defects, was fixed to 200 W, while the laser power of the consecutive layer of artificial defects was changed during the print based on the values listed in Table 5-6.

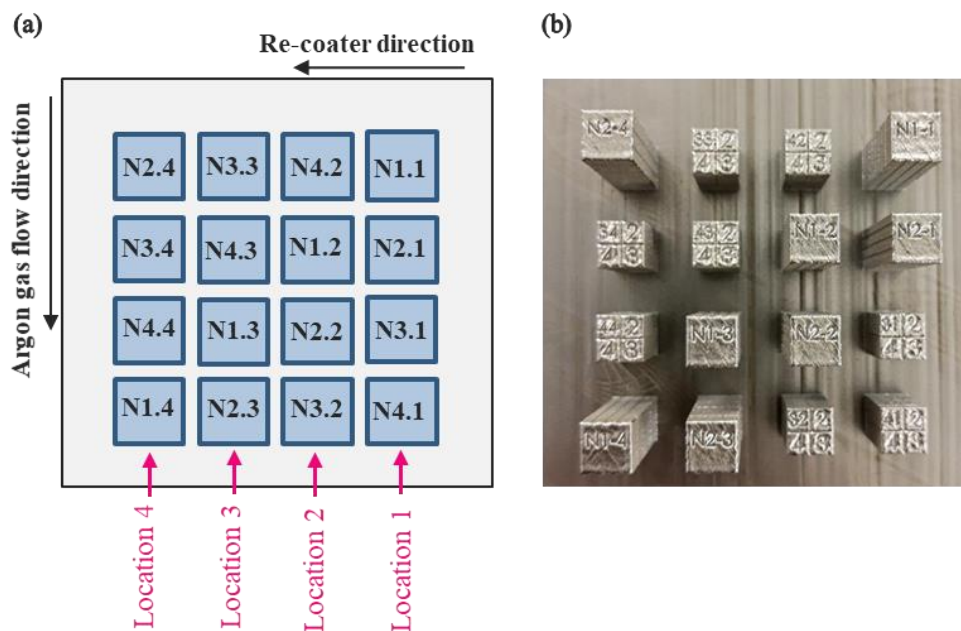


Figure 5-6: (a) Sample layout and (b) printed samples on the build plate

Table 5-6: Laser power variation at capping layer in four parts of each sample based on their location

	P1	P2	P3	P4
Location 1	200	220	240	260
Location 2	205	225	245	265
Location 3	210	230	250	270
Location 4	215	235	255	275

5.3.2 Validating the controller by two different sets of experiments

Two sets of experiments were designed with the size of 15×15×25 (W×L×H) mm³ and labeled as X-series and Y-series. All of the X-series and Y-series were fabricated with Hastelloy-X. Also, vertical rectangle-shape grooves were added to the geometry of these samples to facilitate finding the location of pores in the analysis.

1- X-series included two cubical-shape coupon samples (X1 and X2) with similar distribution and size of artificial defects, as shown in Figure 5-7(a) and Figure 5-7(b). In the design of X-series, seven sizes of cylindrical artificial defects were considered ranging from $\emptyset, H=100 \mu\text{m}$ to $\emptyset, H=400 \mu\text{m}$. Then, two repetitions of each size were randomly distributed inside the samples. Figure 5-7(c) and Figure 5-7(d) represented the locations, ids, and sizes of defects. Also, sample X1 was printed with the standard print parameters used to obtain high-quality Hastelloy-X parts (power= 200 W, layer thickness= 40 μm , hatching distance= 90 μm , and speed= 1000 mm/sec). As a result, the print parameters of sample X1 were fixed during the print. Sample X2 was also fabricated with a similar hatching distance, layer thickness, and scan speed to X1. Although its power initially was set to 200 W, it could change based on the methodology discussed in Section 5.2.1.

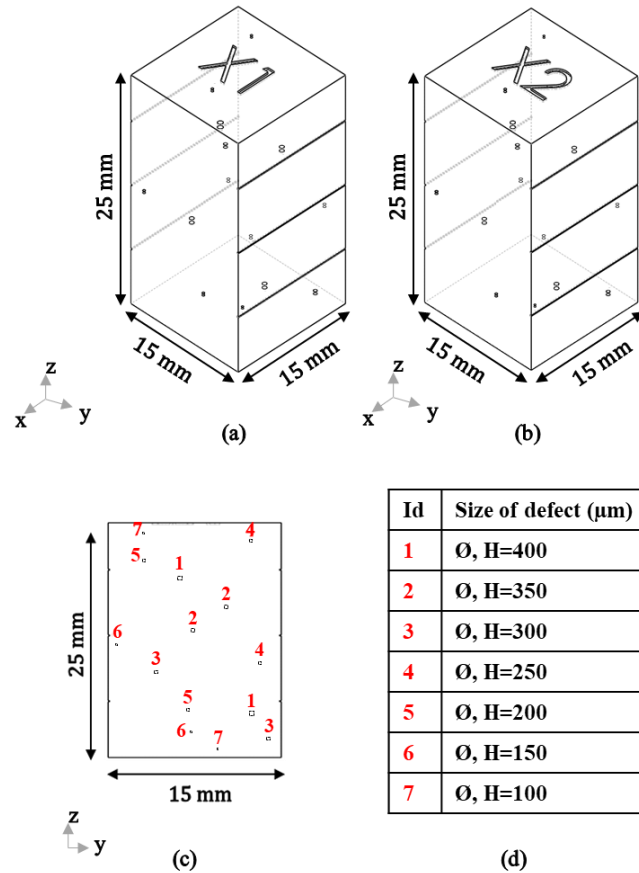


Figure 5-7: a) 3D view of X1, b) 3D view of X2, c) x-z coordinate of X-series samples, and d) x-y coordinate of X-series samples showing the distribution of the artificial defects

2- Y-series also included two cubical-shape coupon samples (Y1 and Y2) with randomized defects, as shown in Figure 5-8. To mimic the randomized defects and create a low, dense part, energy density was reduced in Y-series parts by decreasing the power to 150 W. Thus, the following parameters were considered:

- Power= 150 W,
- Layer thickness=40 μm ,
- Hatching distance= 90 μm , and
- Speed= 1000 mm/sec.

The Y1 print parameters were fixed during the print. In addition, the layer thickness, hatching distance, and speed of sample Y2 were set similar to corresponding parameters in sample Y1; however, its power could change based on the algorithm discussed in Section 5.2.1.

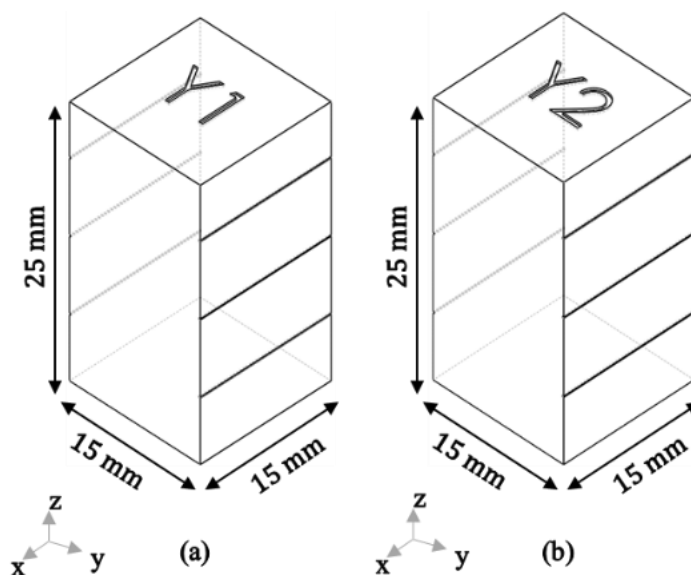
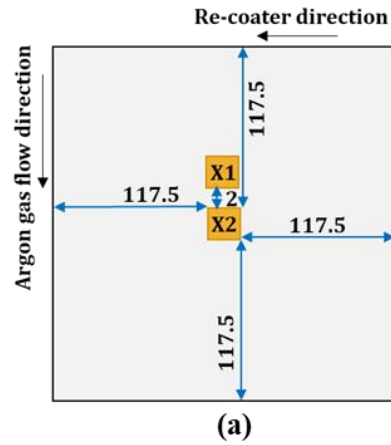
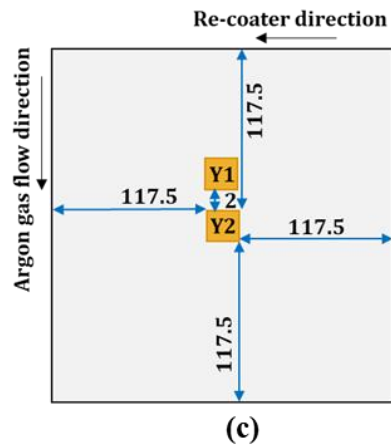


Figure 5-8: a) 3D view of Y1 and b) 3D view of Y2

Figure 5-9(a) and Figure 5-9(c) show the location of X-series and Y-series, respectively. As shown in Figure 5-9(a) and Figure 5-9(c), X2 and Y2 were fabricated in the center of the build plate. Additionally, samples X1 and Y1 were printed close to X2 and Y2 (2 mm distance) to reduce the effect of location on detection quality which was discussed in Chapter 3 and Chapter 4.



(b)



(d)

Figure 5-9: (a) Sample layout of X-series, (b) printed X-series samples on the build plate, c) Sample layout of Y-series, and (d) printed Y-series samples on the build plate

5.4 Computed tomography (CT-Scanning)

All samples (N-series, X-series, and Y-series) were CT-scanned to detect the position and size of actual defects with similar hardware and software to previous chapters. CT-Scan results of N-series, X-series, and Y-series samples are discussed in the following sections:

5.4.1 N-series sample

The pores' information (diameter and location) was measured through the μ CT. The front view of samples (N1, N2, N3, and N4) are represented in Figure 5-10. It should be reminded that the laser power was changed during the fabrication to heal pores.

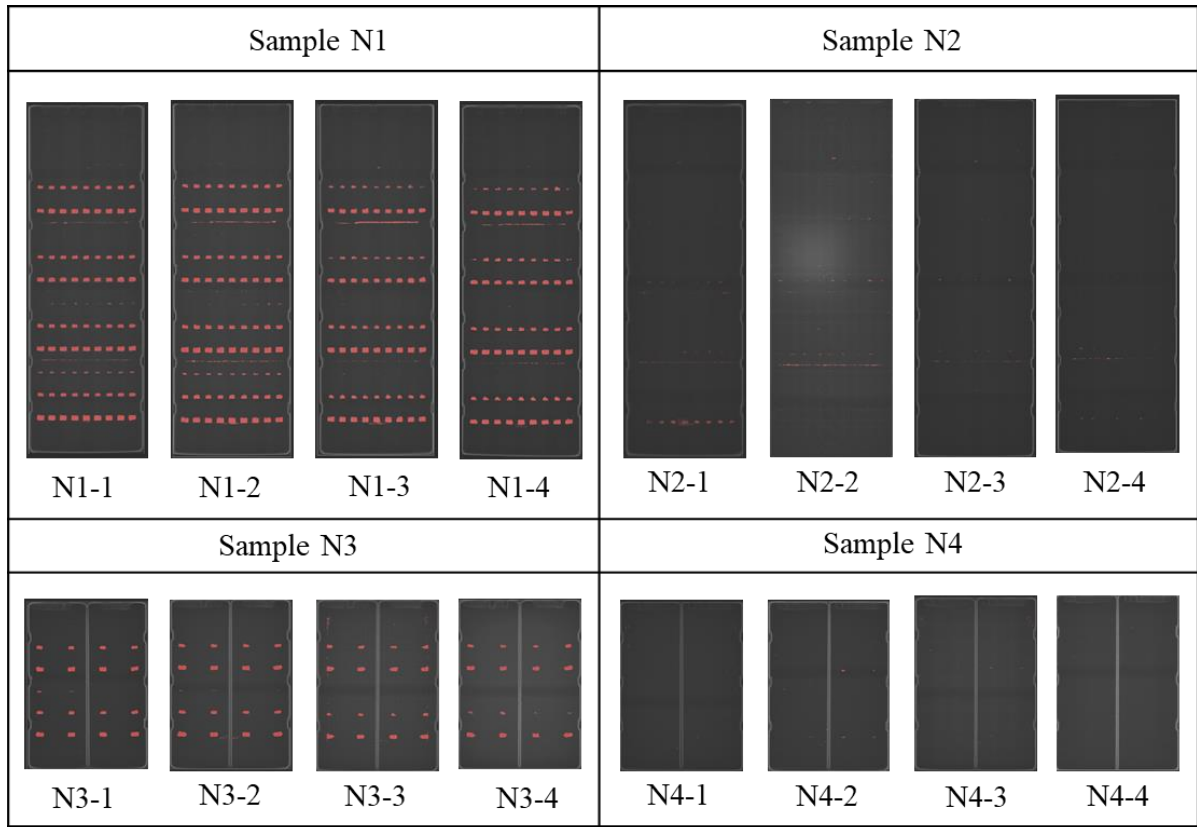


Figure 5-10: CT scan result of N-series sample

5.4.2 X-series sample

The pores' size and location were calculated through the μ CT. The front view of samples (X1 and X2) are depicted in Figure 5-11, in which pores are labeled as shown in Figure 5-7(c). It should be recognized that CT-scan's results were filtered to only highlight the artificial defects.

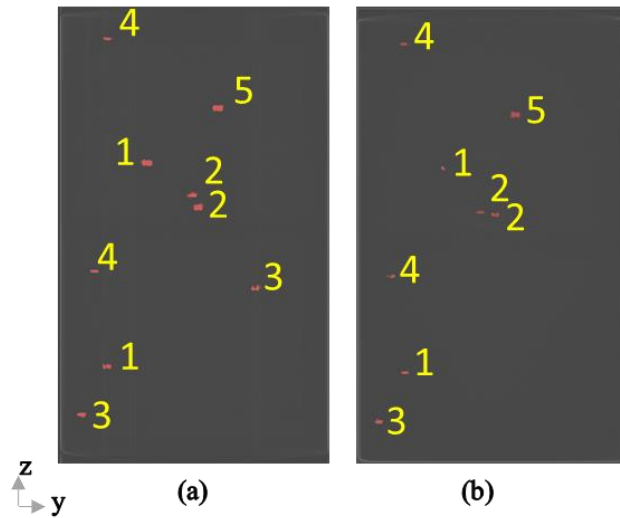


Figure 5-11: CT scan result of Samples a) X1 and b) X2

5.4.3 Y-series sample

Y-series samples also were CT-scanned. The identified pores through μ CT were filtered out pores smaller than $100\ \mu\text{m}$ since the defect detection algorithm is only cable to detect porosity larger than $100\ \mu\text{m}$, discussed in Chapter 4. So, the front view of samples Y1 and Y2 are shown in Figure 5-12(a) and Figure 5-12(b), respectively.

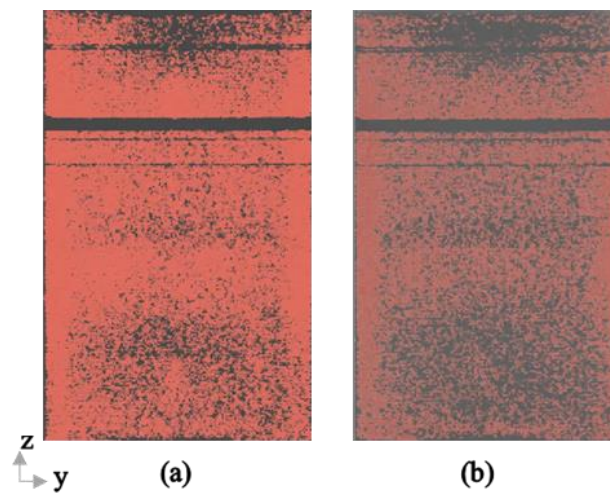


Figure 5-12: CT scan result of Samples a) Y1 and b) Y2

5.5 Results and discussion

5.5.1 Identifying the optimum amount of laser power to heal defects

As discussed in Section 5.3.1, N samples were designed and fabricated to enhance the knowledge about what amount of laser power could heal different sizes of defects. Thus, five sizes of cylindrical defects were embedded in N samples. To find more precise result, the total number of 89 defects for each size of \emptyset , H=100 μm , \emptyset , H=150 μm , \emptyset , H=300 μm , and \emptyset , H=400 μm and 178 defects for \emptyset , H=200 μm were embedded in N-series samples. The next consecutive layer of these defects was fabricated using sixteen various laser powers from 200 W to 275 W with a step size of 5. First, all samples were CT-scanned, and then the percentage of healing of each size of artificial defects was analyzed and listed in Table 5-7 and visualized in Figure 5-13.

Table 5-7: Percentage of healing of five sizes of artificial defects after applying sixteen amounts of laser power

Defect Size (μm) Power (W)	\emptyset , H=100	\emptyset , H=150	\emptyset , H=200	\emptyset , H=300	\emptyset , H=400
200	20.22	8.99	3.37	0.00	0.00
205	78.65	85.39	10.11	0.00	0.00
210	100.00	91.21	52.25	0.00	0.00
215	100.00	95.51	49.44	0.00	0.00
220	100.00	98.88	55.62	0.00	0.00
225	100.00	100.00	57.30	0.00	0.00
230	100.00	100.00	78.65	2.25	0.00
235	100.00	100.00	71.35	4.49	0.00
240	100.00	100.00	84.83	0.00	0.00
245	100.00	100.00	78.65	0.00	0.00
250	100.00	100.00	95.51	11.24	0.00
255	100.00	100.00	93.82	13.48	0.00
260	100.00	100.00	100.00	11.24	0.00
265	100.00	100.00	100.00	11.24	0.00
270	100.00	100.00	100.00	20.22	1.12

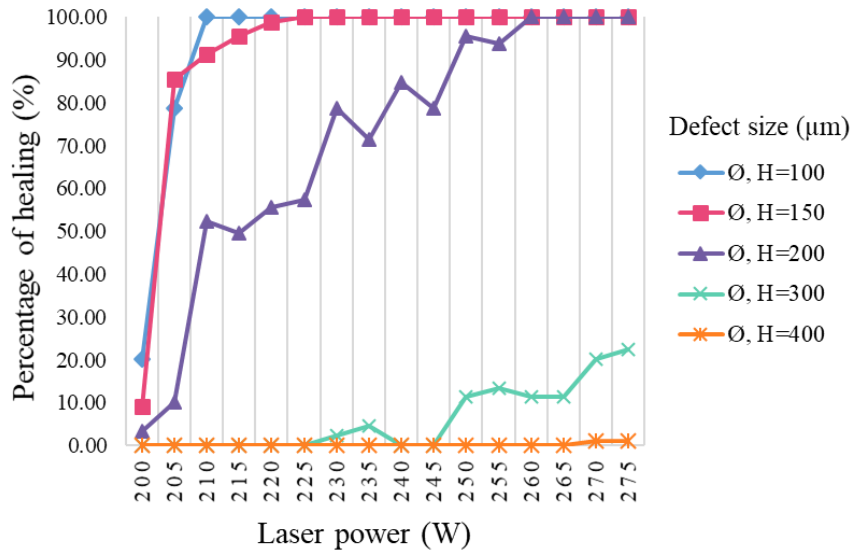


Figure 5-13: Percentage of healing of five sizes of artificial defects after applying sixteen amounts of laser power

Based on Table 5-7 and Figure 5-13, defects with the size of Ø, H=100 µm, Ø, H=150 µm, and Ø, H=200 µm were completely disappeared with the laser power of 210 W, 225 W, 260 W, respectively. It should be noted that increasing the power to 260 W might result in the key-hole porosity and also change the desired microstructure. On the other hand, Ø, H=300 µm and Ø, H=400 µm defects were not healed even under the exposure of 270 W laser power. As a result, for defects with the size of Ø, H=100 µm and Ø, H=150 µm, 210 W and 225 W were set for the next step of this research, respectively; however, for other three sizes of defects (Ø, H=200 µm, Ø, H=300 µm, and Ø, H=400 µm), the size of remaining un-healed defects was calculated and averaged as demonstrated in Figure 5-14.

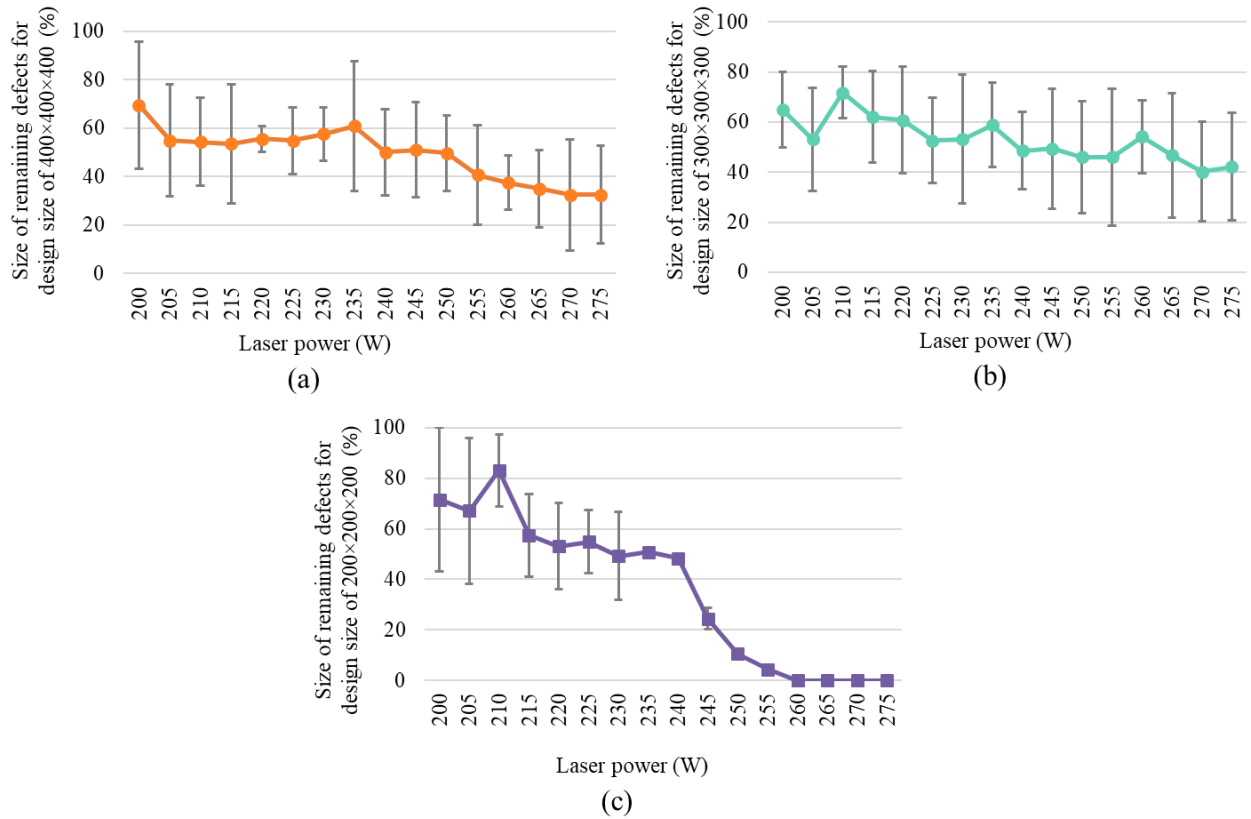


Figure 5-14: Percentage of sizes of um-healed defects after applying sixteen amounts of laser power on the consecutive layer of defects with the size of a) \emptyset , H=400 μm , b) \emptyset , H=300 μm , and c) \emptyset , H=200 μm

Figure 5-14 indicated that the size of the remaining defects slightly decreased by increasing the laser power, although none of the defects in Figure 5-14 (a) and Figure 5-14 (b) were healed completely. As a result, instead of finding the laser power by which defects were healed completely, the laser power was selected when it could heal defects up to 50% of their original size to avoid creating any key-hole defects. Thus, 240 W and 250 W were selected for healing defects with the size of \emptyset , H=300 μm and \emptyset , H=400 μm , respectively. With a similar approach, 230 W was chosen for the defects size of \emptyset , H=200 μm . Also, for the defect size of (\emptyset , H=200 μm), there are limited numbers of un-healed defects when the laser power is more than 230 W. As shown in Figure 5-14 (c), only one defect was not healed under the exposure of 235 W, 240 W, 250 W, and 255 W where two defects were not healed by 245 W, which their sizes were approximately 20% of its designed size ($\sim 40 \mu\text{m}$). As a result, the following amount of laser power was selected:

- 210 W for defect size of \emptyset , H=100 μm ,
- 225 W for defect size of \emptyset , H=150 μm ,

- 230 W for defect size of \emptyset , H=200 μm ,
- 240 W for defect size of \emptyset , H=300 μm , and
- 250 W for defect size of \emptyset , H=400 μm .

5.5.2 Validating the controller by two different experimental sets

After fabricating X-series and Y-series, LCF tables of both prints were checked, and all samples were analyzed by CT-scan. The results of applying the controller on samples X2 and Y2 will be presented and compared with the result of standard samples (X1 and Y1) and CT-scan in Sections 5.5.2.1 and 5.5.2.2.

5.5.2.1 X-series sample (samples incorporating artificial defects)

X-series samples (X1 and X2) were fabricated to evaluate the performance of the controller. Sample X1 was fabricated when the controller was inactive, and sample X2 was printed when the controller was active. In other words, sample X1 was printed with the standard print parameters, fixed during the print, while the power of sample X2 was changed during the fabrication based on the LCF table, which was transferred via the MQTT broker to the laser. The LCF tables created during the fabrication of X2 are examined for the layer printed on top of artificial defects, and the result demonstrated that the control system worked properly and power was changed during the process; however, based on the analysis discussed in Section 5.5.1, the increase of laser power for each size of defect should be as follows:

Table 5-8: Change of laser power in a capping zone on artificial defects based on their id based on analysis (Figure 5-7)

Id	Power (W)
1	250
2	240
3	240
4	230
5	230
6	225
7	210

Whereas LCF tables created during the process showed that the increase of laser power was less than expected, which is listed below in Table 5-9:

Table 5-9: Change of laser power in a capping zone on artificial defects based on their id in the real-time process

Id	Power (W)
1	240
2	230
3	230
4	225
5	225
6	210
7	210

The potential reason for this mismatch could be detecting fewer numbers of indicators in X2 than R-series samples. Therefore, one level decrease in changing the laser power was observed.

Table 5-10 lists the actual radius of defects based on the CT-scan results, showing the comparison between sizes of porosities in samples X1 and X2.

Table 5-10: The actual radius of defects embedded in X1 and X2 based on the CT-scan results

Id	Design size (μm^3)	Defect radius in X1 (μm)	Defect radius in X2 (μm)
1	\emptyset , H=400 μm	394.05	344.56
	\emptyset , H=400 μm	383.13	274.74
2	\emptyset , H=350 μm	331.38	265.06
	\emptyset , H=350 μm	321.38	238.32
3	\emptyset , H=300 μm	299.27	230.14
	\emptyset , H=300 μm	291.57	-
4	\emptyset , H=250 μm	246.80	200.55
	\emptyset , H=250 μm	238.89	196.67
5	\emptyset , H=200 μm	199.07	174.2
	\emptyset , H=200 μm	-	-
6	\emptyset , H=150 μm	-	-
	\emptyset , H=150 μm	-	-
7	\emptyset , H=100 μm	-	-
	\emptyset , H=100 μm	-	-

As listed in Table 5-10, the following results are drawn:

- Defects 6 and 7 were completely healed during the process for both X1 and X2.
- One of the defects 5 was filled in both samples. In contrast, another one was filled 25 (μm) in X2 and less than 1 (μm) in X1.
- The radius of defects 4 showed that their shrinkage was 3 (μm) and 11 (μm) in X1; however, the shrinkage of these defects embedded in sample X2 was approximately 50 (μm) and 53 (μm).

- One of the defects 3 was completely healed in X2, whereas the shrinkage of the similar defect in sample X1 was only 8.5 (μm). Additionally, another position of defect 3 showed that its shrinkage was limited to 70 (μm) in X2, while the size of a similar one in X1 was unchanged (no shrinkage).
- The radiuses of defects 2 showed that defects of X1 were filled 19 (μm) and 29 (μm), whereas defects of X2 was healed up to 112 (μm) and 120 (μm).
- Finally, the shrinkage of defects 1 was approximately 6 (μm) and 17 (μm) in X1, and the corresponding ones in sample X2 showed the shrinkage of 56 (μm) and 126 (μm).

The above results confirmed that the shrinkage of defects embedded in sample X2 was more than its corresponding defects in X1, which showed the controller's functionality. However, the laser power should increase to heal at least half size of defects (as discussed in Section 5.1). For example, for the defect with sizes of \emptyset , H=400 μm , it was supposed to the laser power would increase to 250 W (Table 5-8) to shrink the defects to 200 μm , whereas the power was changed to 240 W (Table 5-9) and the shrinkage limited to 126 μm . Thus, the laser power should be increased one level to obtain better and more promising results.

5.5.2.2 Y-series sample (randomized defects)

Samples Y1 and Y2 were manufactured by low energy density to create randomized defects. Therefore, these two samples were used to evaluate the performance of the developed controller. As observed in Figure 5-12, the identified porosities in sample Y1 were more than detected pores in sample Y2. To confirm this claim, the density of both samples is measured, which resulted in 97.56% and 98.50% for samples Y1 and Y2, respectively. Also, the histogram of pores revealed that the numbers and size of lack-of-fusion pores of sample Y2 is less than their corresponding amounts in sample Y1 (Figure 5-15). For instance, the largest size of defect identified in samples Y1 and Y2 was 487 (μm) and 280 (μm), respectively. The CT-scan analysis also revealed that 32380 and 26978 pores were detected in samples Y1 and Y2, respectively. Thus, all of the results mentioned above confirmed that using the controller increased the density of the part printed when the controller was active compared to the printed parts when the controller was inactive.

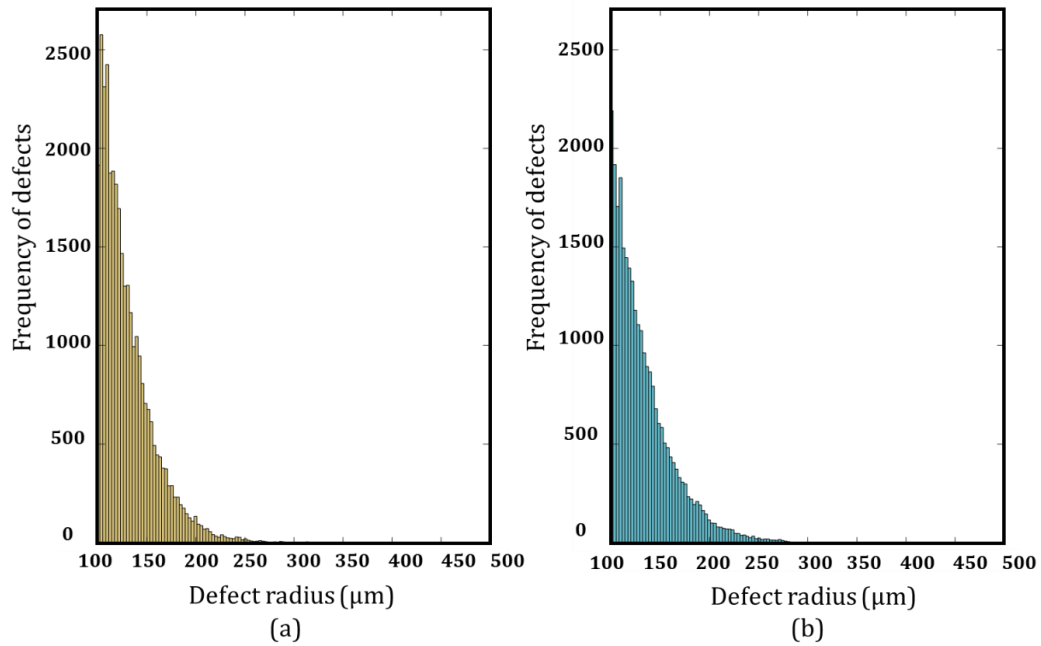


Figure 5-15: The histogram of pores identified in samples a) Y1 and b) Y2

Although this methodology has not been able to heal porosities completely, it resulted in a 0.94% increase in the density of sample Y2 compared to sample Y1. Thus, it was a great achievement towards developing the intermittent closed-loop controller for the commercial EOS M290 LPBF-AM system. However, more experimental analyses are required to fully heal defects.

5.6 Summary

In this chapter, based on the result of the SOM algorithm (discussed in Chapter 4), the identified indicators were clustered by the K-means algorithm. Then, an optimized square area of $0.6 \times 0.6 \text{ mm}^2$ was considered around the center of each cluster as a zone at which the laser power should be increased in the next deposition layer to heal/minimize the induced defects. To identify the optimum laser power value, a set of samples with seeded artificial voids was designed and printed with the fixed hatching distance, scanning speed, and layer thickness; however, its laser power was increased in the capping layer on the artificial voids to minimize their size and number. Then by analyzing the result of the CT-scan, the optimum value of laser power was identified for healing each size of defects. By considering the defect size and optimum laser power, rules were defined to calculate the new laser power named as a Laser Correction File. Additionally, different components of the closed-loop approach were connected via the MQTT broker for collecting data, correcting data, detecting defects, calculating the

LCF, and sending the new LCF to the actuator. Lastly, the proposed controller was applied to two sets of experiments that included artificial and randomized defects to validate the performance of the controller.

Chapter 6. Conclusions and Future Work

6.1 Conclusions

The focus of this dissertation was the development of in-situ defect detection algorithms and intermittent closed-loop control system for minimizing defects induced due to the lack of fusion during the part fabrication by the commercial LPBF system. To this end, light intensity emitted from the melt pool was collected by a commercial in-situ photodiode sensor during the fabrication of multiple Hastelloy-X coupons. Then, the collected dataset was analyzed by three analytical algorithms: 1) Absolute Limits (AL), 2) Signal Dynamics (SD), and 3) Short-Term Fluctuations (STF), as well as one unsupervised algorithm known as Self-Organizing Map (SOM). These algorithms were calibrated and customized based on the CT-scan analysis to detect artificial defects. Eventually, the SOM detection algorithm was integrated into an intermittent controller for healing the randomized defects.

The following conclusions can be drawn from this thesis:

- Among the analytical algorithms used in this study, the Absolute Limits (AL) algorithm resulted in better accuracy in detecting the location and size of artificial and randomized defects compared to the Signal Dynamics (SD) and Short-Term Fluctuations (STF) algorithms.
- The smallest size of artificially seeded defects identified by the AL algorithm was 120 μm . On the other hand, the detection of randomized defects demonstrated that the TP rate of AL in detecting defects created by decreasing the laser power (i.e., 100 Watt) was $<30\%$. However, the AL resulted in a better pore detection created by high speeds and high hatching distances, respectively showing accuracies of $70.14 \pm 2.24\%$ and $72.82 \pm 1.39\%$.
- Applying the SOM algorithm on artificial defects ranging from 100 to 320 μm with different geometries and distributions disclosed that the smallest size of defects detected was 100 μm . Additionally, analyzing the randomized defects by calculating true positive and true negative rates uncovered that the identification of porosity induced by the lack-of-fusion was successful for the samples printed with relatively low laser powers of 175, 150, and 125 W, high hatching distances of 110, 130, and 150 μm , and high process speeds of 1100, 1300, and 1500 mm/s. The results revealed that the pores created by low laser power were identified at the TP rate of $\sim 75\%$ by the SOM, which was not achievable through applying the AL when the TP rate was $<30\%$. Additionally, the SOM exhibited similar detection rates to those of the AL in identifying pores

induced due to the high hatching distances and high speeds; however, the SOM improved the TN rates up to 31% and 20% for such samples, respectively.

- The position of parts in the build plate affects the light intensity signal and the accuracy of defect detection. The AL and SOM algorithms did not provide a remedy for the detection dependency on the part's location in the build plate.
- The AL and SOM algorithms were also compared based on their computational speed. The SOM was found to detect defects per layer approximately 86% faster than the AL.
- Applying the intermittent controller during the LPBF process to heal lack-of-fusion defects revealed that the proposed control system worked properly. The CT-scan analysis of artificial defects in the part printed with the controller showed shrinkage of 25 (μm)- 120 (μm) more than the corresponding defects in the part printed when the controller was off. Additionally, CT- scan analysis of parts with randomized defects uncovered that the controller could increase the density of the part up to approximately 1% compared to the printed parts when the controller was inactive. This suggests a great improvement that is very welcome by the industry.

6.2 Recommendations and Future Work

The research described in this dissertation has focused on the development of advanced defect detection algorithms and an intermittent control system for the commercial LPBF machine. However, to achieve our intended vision of developing the commercially ready control system for the LPBF additive manufacturing machine, further research on hardware, algorithms, and materials should be conducted.

1. This research has described the use of commercial on-axial photodiode to detect lack-of-fusion pores. The Photodiode's resolution led to the identification of defects larger than 100 μm ; however, using a higher-resolution photodiode with the combination of other available sensors is recommended. In addition, collecting data from multiple sensors could help achieve more accurate detection, leading to the detection of pores sized smaller than 100 μm .
2. The applied intensity correction developed by the EOS company was not completely able to remove the position dependency of the dataset. Thus, the development of a new intensity correction is recommended to tackle this concern and increase the accuracy of defect detection algorithms.
3. The targeted zone around the identified defects (discussed in Chapter 5) is currently fixed in terms of size and geometry. The size of the zone could be adaptively changed based on defect size.

Additionally, the geometry of the zone could also be changed. Based on the experimental analysis, the identified defects are usually circle/oval-shaped. As a result, circular/oval shapes could be considered instead of squares to avoid re-melting the corners and creating key-hole pores.

4. In this study, only one experimental set was printed and analyzed to identify the optimum laser power, which resulted in defects not being healed completely. Thus, to fully heal defects, different sets of process parameters could be printed and analyzed to achieve optimum laser power.
5. To remove any potential glitching issue in the communication via MQTT, the use of a buffer is highly recommended. Using the buffer could also help provide enough time to the PC hardware for writing and reading the dataset.
6. To evaluate the controller's functionality, the density of printed samples was calculated in this study. Applying and analyzing other mechanical tests are suggested to determine the mechanical properties of the final parts.
7. To increase the computational time of the communication between different components, converting the code in the C++ environment is suggested. Additionally, developing the whole package in one software is strongly recommended.
8. This study has focused on Hastelloy-X material. However, the proposed methodology could be applied to other materials (e.g., Titanium) to allow developing the adaptive algorithm for adjusting and changing the laser power based on the material type.
9. It is recommended to apply the proposed methodology to other EOS M290 systems to increase the repeatability of evaluation and confidence of the algorithm for commercial use.

Letter of copyright permission

Chapter 2:

JOHN WILEY AND SONS LICENSE TERMS AND CONDITIONS

Nov 17, 2021

This Agreement between University of Waterloo – Katayoon Taherkhani ("You") and John Wiley and Sons ("John Wiley and Sons") consists of your license details and the terms and conditions provided by John Wiley and Sons and Copyright Clearance Center.

License Number	5190931489328
License date	Nov 16, 2021
Licensed Content Publisher	John Wiley and Sons
Licensed Content Publication	Wiley Books
Licensed Content Title	Monitoring and Quality Assurance for Metal Additive Manufacturing
Licensed Content Date	Oct 22, 2021
Licensed Content Pages	69
Type of Use	Dissertation/Thesis
Requestor type	University/Academic
Format	Print and electronic
Portion	Figure/table
Number of figures/tables	1
Will you be translating?	No
Title	In-Situ Monitoring and Quality Assurance Algorithms for Laser Powder-Bed Fusion
Institution name	UWaterloo
Expected presentation date	Feb 2022
Portions	Figure 11.9
Requestor Location	University of Waterloo Unit 174, 350 Columbia St. West Waterloo, ON N2L6P1 Canada Attn: University of Waterloo
Publisher Tax ID	EU826007151
Total	0.00 USD
Terms and Conditions	

Figure 2-2:

JOHN WILEY AND SONS LICENSE TERMS AND CONDITIONS

Nov 16, 2021

This Agreement between University of Waterloo – Katayoon Taherkhani ("You") and John Wiley and Sons ("John Wiley and Sons") consists of your license details and the terms and conditions provided by John Wiley and Sons and Copyright Clearance Center.

License Number	5190931489328
License date	Nov 16, 2021
Licensed Content Publisher	John Wiley and Sons
Licensed Content Publication	Wiley Books
Licensed Content Title	Monitoring and Quality Assurance for Metal Additive Manufacturing
Licensed Content Date	Oct 22, 2021
Licensed Content Pages	69
Type of Use	Dissertation/Thesis
Requestor type	University/Academic
Format	Print and electronic
Portion	Figure/table
Number of figures/tables	1
Will you be translating?	No
Title	In-Situ Monitoring and Quality Assurance Algorithms for Laser Powder-Bed Fusion
Institution name	UWaterloo
Expected presentation date	Feb 2022
Portions	Figure 11.9
Requestor Location	University of Waterloo Unit 174, 350 Columbia St. West Waterloo, ON N2L6P1 Canada Attn: University of Waterloo
Publisher Tax ID	EU826007151
Total	0.00 USD
Terms and Conditions	

Figure 2-3(a):

ELSEVIER LICENSE TERMS AND CONDITIONS

Nov 16, 2021

This Agreement between University of Waterloo – Katayoon Taherkhani ("You") and Elsevier ("Elsevier") consists of your license details and the terms and conditions provided by Elsevier and Copyright Clearance Center.

License Number	5190940963647
License date	Nov 16, 2021
Licensed Content Publisher	Elsevier
Licensed Content Publication	Physics Procedia
Licensed Content Title	Pyrometric analysis of thermal processes in SLM technology
Licensed Content Author	M. Pavlov,M. Doubenskaia,I. Smurov
Licensed Content Date	Jan 1, 2010
Licensed Content Volume	5
Licensed Content Issue	n/a
Licensed Content Pages	9
Start Page	523
End Page	531
Type of Use	reuse in a thesis/dissertation
Portion	figures/tables/illustrations
Number of figures/tables/illustrations	1
Format	both print and electronic
Are you the author of this Elsevier article?	No
Will you be translating?	No
Title	In-Situ Monitoring and Quality Assurance Algorithms for Laser Powder-Bed Fusion
Institution name	UWaterloo
Expected presentation date	Feb 2022
Portions	Fig .2
Requestor Location	University of Waterloo Unit 174, 350 Columbia St. West Waterloo, ON N2L6P1 Canada Attn: University of Waterloo
Publisher Tax ID	GB 494 6272 12
Total	0.00 USD
Terms and Conditions	

Figure 2-3(b):

ELSEVIER LICENSE TERMS AND CONDITIONS

Nov 16, 2021

This Agreement between University of Waterloo – Katayoon Taherkhani ("You") and Elsevier ("Elsevier") consists of your license details and the terms and conditions provided by Elsevier and Copyright Clearance Center.

License Number	5190941172767
License date	Nov 16, 2021
Licensed Content Publisher	Elsevier
Licensed Content Publication	Additive Manufacturing
Licensed Content Title	Tracking and controlling the morphology evolution of 3D powder-bed fusion in situ using inline coherent imaging
Licensed Content Author	Tristan G. Fleming, Stephen G.L. Nestor, Troy R. Allen, Mark A. Boukhaled, Nathan J. Smith, James M. Fraser
Licensed Content Date	Mar 1, 2020
Licensed Content Volume	32
Licensed Content Issue	n/a
Licensed Content Pages	1
Start Page	100978
End Page	0
Type of Use	reuse in a thesis/dissertation
Portion	figures/tables/illustrations
Number of figures/tables/illustrations	1
Format	both print and electronic
Are you the author of this Elsevier article?	No
Will you be translating?	No
Title	In-Situ Monitoring and Quality Assurance Algorithms for Laser Powder-Bed Fusion
Institution name	UWaterloo
Expected presentation date	Feb 2022
Portions	Fig. 1(b)
Requestor Location	University of Waterloo Unit 174, 350 Columbia St. West Waterloo, ON N2L6P1 Canada Attn: University of Waterloo
Publisher Tax ID	GB 494 6272 12
Total	0.00 USD
Terms and Conditions	

Figure 2-4 (a):

ELSEVIER LICENSE TERMS AND CONDITIONS

Nov 18, 2021

This Agreement between University of Waterloo – Katayoon Taherkhani ("You") and Elsevier ("Elsevier") consists of your license details and the terms and conditions provided by Elsevier and Copyright Clearance Center.

License Number	5192150675742
License date	Nov 18, 2021
Licensed Content Publisher	Elsevier
Licensed Content Publication	Additive Manufacturing
Licensed Content Title	On the use of spatter signature for in-situ monitoring of Laser Powder Bed Fusion
Licensed Content Author	Giulia Repossini, Vittorio Laguzza, Marco Grasso, Bianca Maria Colosimo
Licensed Content Date	Aug 1, 2017
Licensed Content Volume	16
Licensed Content Issue	n/a
Licensed Content Pages	14
Start Page	35
End Page	48
Type of Use	reuse in a thesis/dissertation
Portion	figures/tables/illustrations
Number of figures/tables/illustrations	1
Format	both print and electronic
Are you the author of this Elsevier article?	No
Will you be translating?	No
Title	In-Situ Monitoring and Quality Assurance Algorithms for Laser Powder-Bed Fusion
Institution name	UWaterloo
Expected presentation date	Feb 2022
Portions	Fig. 2.
Requestor Location	University of Waterloo Unit 174, 350 Columbia St. West Waterloo, ON N2L6P1 Canada Attn: University of Waterloo
Publisher Tax ID	GB 494 6272 12
Total	0.00 USD

Figure 2-4 (b):

ELSEVIER LICENSE TERMS AND CONDITIONS

Nov 18, 2021

This Agreement between University of Waterloo -- Katayoon Taherkhani ("You") and Elsevier ("Elsevier") consists of your license details and the terms and conditions provided by Elsevier and Copyright Clearance Center.

License Number	5192150921843
License date	Nov 18, 2021
Licensed Content Publisher	Elsevier
Licensed Content Publication	Additive Manufacturing
Licensed Content Title	Application of supervised machine learning for defect detection during metallic powder bed fusion additive manufacturing using high resolution imaging.
Licensed Content Author	Christian Gobert,Edward W. Reutzel,Jan Petrich,Abdalla R. Nassar,Shashi Phoha
Licensed Content Date	May 1, 2018
Licensed Content Volume	21
Licensed Content Issue	n/a
Licensed Content Pages	12
Start Page	517
End Page	528
Type of Use	reuse in a thesis/dissertation
Portion	figures/tables/illustrations
Number of figures/tables/illustrations	1
Format	both print and electronic
Are you the author of this Elsevier article?	No
Will you be translating?	No
Title	In-Situ Monitoring and Quality Assurance Algorithms for Laser Powder-Bed Fusion
Institution name	UWaterloo
Expected presentation date	Feb 2022
Portions	Fig. 4
Requestor Location	University of Waterloo Unit 174, 350 Columbia St. West Waterloo, ON N2L6P1 Canada Attn: University of Waterloo
Publisher Tax ID	GB 494 6272 12
Total	0.00 USD

Figure 2-6:

ELSEVIER LICENSE TERMS AND CONDITIONS

Nov 18, 2021

This Agreement between University of Waterloo -- Katayoon Taherkhani ("You") and Elsevier ("Elsevier") consists of your license details and the terms and conditions provided by Elsevier and Copyright Clearance Center.

License Number	5192151102599
License date	Nov 18, 2021
Licensed Content Publisher	Elsevier
Licensed Content Publication	Additive Manufacturing
Licensed Content Title	Flaw detection in powder bed fusion using optical imaging
Licensed Content Author	Mostafa Abdelrahman,Edward W. Reutzel,Abdalla R. Nassar,Thomas L. Starr
Licensed Content Date	May 1, 2017
Licensed Content Volume	15
Licensed Content Issue	n/a
Licensed Content Pages	11
Start Page	1
End Page	11
Type of Use	reuse in a thesis/dissertation
Portion	figures/tables/illustrations
Number of figures/tables/illustrations	1
Format	both print and electronic
Are you the author of this Elsevier article?	No
Will you be translating?	No
Title	In-Situ Monitoring and Quality Assurance Algorithms for Laser Powder-Bed Fusion
Institution name	UWaterloo
Expected presentation date	Feb 2022
Portions	Fig. 9
Requestor Location	University of Waterloo Unit 174, 350 Columbia St. West Waterloo, ON N2L6P1 Canada Attn: University of Waterloo
Publisher Tax ID	GB 494 6272 12
Total	0.00 USD

Figure 2-7:

AIP PUBLISHING LICENSE TERMS AND CONDITIONS

Nov 18, 2021

This Agreement between University of Waterloo -- Katayoon Taherkhani ("You") and AIP Publishing ("AIP Publishing") consists of your license details and the terms and conditions provided by AIP Publishing and Copyright Clearance Center.

License Number	5192160104079
License date	Nov 18, 2021
Licensed Content Publisher	AIP Publishing
Licensed Content Publication	AIP Conference Proceedings
Licensed Content Title	Process monitoring of additive manufacturing by using optical tomography
Licensed Content Author	Guenter Zenzinger, Joachim Bamberg, Alexander Ladewig, et al
Licensed Content Date	Mar 31, 2015
Licensed Content Volume	1650
Licensed Content Issue	1
Type of Use	Thesis/Dissertation
Requestor type	Student
Format	Print and electronic
Portion	Figure/Table
Number of figures/tables	1
Will you be translating?	No
Title	In-Situ Monitoring and Quality Assurance Algorithms for Laser Powder-Bed Fusion
Institution name	UWaterloo
Expected presentation date	Feb 2022
Portions	Figure 8
Requestor Location	University of Waterloo Unit 174, 350 Columbia St. West Waterloo, ON N2L6P1 Canada Attn: University of Waterloo
Total	0.00 USD

Figure 2-8:

SPRINGER NATURE LICENSE TERMS AND CONDITIONS

Nov 18, 2021

This Agreement between University of Waterloo – Katayoon Taherkhani ("You") and Springer Nature ("Springer Nature") consists of your license details and the terms and conditions provided by Springer Nature and Copyright Clearance Center.

License Number	5192160341220
License date	Nov 18, 2021
Licensed Content Publisher	Springer Nature
Licensed Content Publication	The International Journal of Advanced Manufacturing Technology
Licensed Content Title	Gaussian process-based surrogate modeling framework for process planning in laser powder-bed fusion additive manufacturing of 316L stainless steel
Licensed Content Author	Gustavo Tapia et al
Licensed Content Date	Sep 22, 2017
Type of Use	Thesis/Dissertation
Requestor type	academic/university or research institute
Format	print and electronic
Portion	figures/tables/illustrations
Number of figures/tables/illustrations	1
Will you be translating?	no
Circulation/distribution	1 - 29
Author of this Springer Nature content	no
Title	In-Situ Monitoring and Quality Assurance Algorithms for Laser Powder-Bed Fusion
Institution name	UWaterloo
Expected presentation date	Feb 2022
Portions	Fig. 3
Requestor Location	University of Waterloo Unit 174, 350 Columbia St. West Waterloo, ON N2L6P1 Canada Attn: University of Waterloo
Total	0.00 USD

Chapter 3:



Research Paper

Development of a defect-detection platform using photodiode signals collected from the melt pool of laser powder-bed fusion

Katayoon Taherkhani ^a, Esmat Sheydaei ^a, Christopher Eischer ^b, Martin Otto ^b, Ehsan Toyserkani ^a

[Show more](#)

[+](#) Add to Mendeley [↻](#) Share [🗨](#) Cite

<https://doi.org/10.1016/j.addma.2021.102152>

[Get rights and content](#)

Under a [Creative Commons license](#)

[open access](#)

Creative Commons

This is an open access article distributed under the terms of the [Creative Commons CC-BY license](#), which permits unrestricted use, distribution, and reproduction in any medium, provided the original work is properly cited.

You are not required to obtain permission to reuse this article.

To request permission for a type of use not listed, please contact [Elsevier Global Rights Department](#).

Are you the [author](#) of this Elsevier journal article?

References

- [1] E. Toyserkani, D. Sarker, O. O. Ibhado, F. Liravi, P. Russo, and K. Taherkhani, “Monitoring and Quality Assurance for Metal Additive Manufacturing,” in *Metal Additive Manufacturing*, 2021.
- [2] M. J. Matthews, G. Guss, S. A. Khairallah, A. M. Rubenchik, P. J. Depond, and W. E. King, “Denudation of metal powder layers in laser powder bed fusion processes,” *Acta Mater.*, vol. 114, pp. 33–42, 2016, doi: 10.1016/j.actamat.2016.05.017.
- [3] E. Toyserkani, D. Sarker, O. O. Ibhado, F. Liravi, P. Russo, and K. Taherkhani, *Metal Additive Manufacturing*, 1st ed. John Wiley, 2021.
- [4] K. Taherkhani, E. Sheydaeian, C. Eischer, M. Otto, and E. Toyserkani, “Development of a defect-detection platform using photodiode signals collected from the melt pool of laser powder-bed fusion,” *Addit. Manuf.*, vol. 46, p. 102152, Oct. 2021, doi: 10.1016/J.ADDMA.2021.102152.
- [5] V. Sergi, F. Caiazzo, L. Cuccaro, V. Alfieri, and F. Cardaropoli, “Experimental analysis of selective laser melting process for Ti-6Al-4V turbine blade manufacturing,” *XIX Int. Symp. High-Power Laser Syst. Appl. 2012*, vol. 8677, no. January 2013, p. 86771H, 2013, doi: 10.1117/12.2010577.
- [6] C. Yan, L. Hao, A. Hussein, and P. Young, “Ti-6Al-4V triply periodic minimal surface structures for bone implants fabricated via selective laser melting,” *J. Mech. Behav. Biomed. Mater.*, vol. 51, pp. 61–73, 2015, doi: 10.1016/j.jmbbm.2015.06.024.
- [7] K. Osakada and M. Shiomi, “Flexible manufacturing of metallic products by selective laser melting of powder,” *Int. J. Mach. Tools Manuf.*, vol. 46, no. 11 SPEC. ISS., pp. 1188–1193, 2006, doi: 10.1016/j.ijmachtools.2006.01.024.
- [8] M. Wong, I. Owen, C. J. Sutcliffe, and A. Puri, “Convective heat transfer and pressure losses across novel heat sinks fabricated by Selective Laser Melting,” *Int. J. Heat Mass Transf.*, vol. 52, no. 1–2, pp. 281–288, 2009, doi: 10.1016/j.ijheatmasstransfer.2008.06.002.
- [9] I. Yadroitsev, P. Bertrand, and I. Smurov, “Parametric analysis of the selective laser melting process,” *Appl. Surf. Sci.*, vol. 253, no. 19, pp. 8064–8069, 2007, doi:

10.1016/j.apsusc.2007.02.088.

- [10] K. Kempen, L. Thijs, E. Yasa, M. Badrossamay, W. Verheecke, and J. P. Kruth, "Process optimization and microstructural analysis for selective laser melting of AlSi10Mg," in *22nd Annual International Solid Freeform Fabrication Symposium - An Additive Manufacturing Conference, SFF 2011*, 2011, no. August, pp. 484–495.
- [11] B. Zhang, Y. Li, and Q. Bai, "Defect Formation Mechanisms in Selective Laser Melting: A Review," *Chinese J. Mech. Eng. (English Ed.)*, vol. 30, no. 3, pp. 515–527, 2017, doi: 10.1007/s10033-017-0121-5.
- [12] H. Gong, K. Rafi, H. Gu, T. Starr, and B. Stucker, "Analysis of defect generation in Ti-6Al-4V parts made using powder bed fusion additive manufacturing processes," *Addit. Manuf.*, vol. 1, pp. 87–98, 2014, doi: 10.1016/j.addma.2014.08.002.
- [13] T. Vilaro, C. Colin, and J. D. Bartout, "As-fabricated and heat-treated microstructures of the Ti-6Al-4V alloy processed by selective laser melting," *Metall. Mater. Trans. A Phys. Metall. Mater. Sci.*, vol. 42, no. 10, pp. 3190–3199, 2011, doi: 10.1007/s11661-011-0731-y.
- [14] M. Leary, J. Elambasseril, S. J. Sun, P. K. Sharp, Q. C. Liu, and M. Brandt, "The Effect of Manufacturing Defects on the Fatigue Behaviour of Ti-6Al-4V Specimens Fabricated Using Selective Laser Melting," *Adv. Mater. Res.*, vol. 891–892, pp. 1519–1524, 2014, doi: 10.4028/www.scientific.net/amr.891-892.1519.
- [15] E. Toyserkani, A. Khajepour, and S. S. Corbin, *Laser cladding*. CRC PRESS LLC, 2004.
- [16] O. Optoelectronics and Osi Optoelectronics, "Photodiode Characteristics," *Osi Optoelectronics*, 2009. <http://www.osioptoelectronics.com/application-notes/an-photodiode-parameters-characteristics.pdf>.
- [17] W. Electronics Inc, "AN-LD17: Photodiode Basics: Selection & Operation," no. 406, pp. 1–4, 2020, [Online]. Available: www.teamWavelength.com.
- [18] J. Low, M. Kreider, D. Pulsifer, A. Jones, and T. Gilani, "Band Gap Energy in Silicon," *Am. J. Undergrad. Res.*, 2009, doi: 10.33697/ajur.2009.017.
- [19] S. Radovanović, A. J. Annema, and B. Nauta, "A 3-Gb/s optical detector in standard CMOS for 850-nm optical communication," *IEEE J. Solid-State Circuits*, vol. 40, no. 8, pp. 1706–

- 1717, 2005, doi: 10.1109/JSSC.2005.852030.
- [20] J. M. Fédéli *et al.*, “High-performance waveguide-integrated germanium PIN photodiodes for optical communication applications,” in *2014 7th International Silicon-Germanium Technology and Device Meeting (ISTDM)*, 2014, pp. 131–132, doi: 10.1109/ISTDM.2014.6874690.
- [21] K. S. Shah, R. Farrell, R. Grazioso, E. S. Harmon, and E. Karplus, “Position-sensitive avalanche photodiodes for gamma-ray imaging,” *IEEE Trans. Nucl. Sci.*, vol. 49, no. 4, pp. 1687–1692, 2002, doi: 10.1109/TNS.2002.801510.
- [22] C. M. Pepin *et al.*, “New UV-enhanced, ultra-low noise silicon avalanche photodiode for radiation detection and medical imaging,” in *IEEE Nuclear Science Symposium Conference Record*, 2010, pp. 1740–1746, doi: 10.1109/NSSMIC.2010.5874072.
- [23] D. L. Gilblom, S. K. Yoo, and P. Ventura, “Operation and performance of a color image sensor with layered photodiodes,” *Infrared Technol. Appl.* XXIX, vol. 5074, pp. 318–331, 2003, doi: 10.1117/12.498557.
- [24] C. E. Hunt *et al.*, “P-i-n High-Speed Photodiodes for X-Ray and Infrared Imagers Fabricated by in Situ-Doped APCVD Germanium Homoepitaxy,” *IEEE Trans. Electron Devices*, vol. 67, no. 8, pp. 3235–3241, 2020, doi: 10.1109/TED.2020.3006810.
- [25] M. Bisht, N. Ray, F. Verbist, and S. Coeck, “Correlation of selective laser melting-melt pool events with the tensile properties of Ti-6Al-4V ELI processed by laser powder bed fusion,” *Addit. Manuf.*, vol. 22, 2018, doi: 10.1016/j.addma.2018.05.004.
- [26] J. Kruth, P. Mercelis, J. Van Vaerenbergh, and T. Craeghs, “Feedback control of Selective Laser Melting,” *Proc. 3rd Int. Conf. Adv. Res. Virtual Rapid Prototyp.*, pp. 1–7, 2007.
- [27] S. Berumen, F. Bechmann, S. Lindner, J. P. Kruth, and T. Craeghs, “Quality control of laser- and powder bed-based Additive Manufacturing (AM) technologies,” in *Physics Procedia*, 2010, vol. 5, no. PART 2, pp. 617–622, doi: 10.1016/j.phpro.2010.08.089.
- [28] V. K. Nadipalli, S. A. Andersen, J. S. Nielsen, and D. B. Pedersen, “Considerations for interpreting in-situ photodiode sensor data in pulsed mode laser powder bed fusion,” *Proc. Jt. Spec. Interes. Gr. Meet. between euspen ASPE Adv. Precis. Addit. Manuf.*, no. September, pp. 66–69, 2019.

- [29] S. Clijsters, T. Craeghs, S. Buls, K. Kempen, and J. P. Kruth, “In situ quality control of the selective laser melting process using a high-speed, real-time melt pool monitoring system,” *Int. J. Adv. Manuf. Technol.*, vol. 75, no. 5–8, pp. 1089–1101, 2014, doi: 10.1007/s00170-014-6214-8.
- [30] T. Craeghs, F. Bechmann, S. Berumen, and J. P. Kruth, “Feedback control of Layerwise Laser Melting using optical sensors,” *Phys. Procedia*, vol. 5, no. PART 2, pp. 505–514, 2010, doi: 10.1016/j.phpro.2010.08.078.
- [31] C. Van Gestel, “Study of physical phenomena of selective laser melting towards increased productivity,” in *Thesis EPFL*, 2015, p. 117, doi: 10.1016/0168-9002(90)90810-S.
- [32] I. A. Okaro, S. Jayasinghe, C. Sutcliffe, K. Black, P. Paoletti, and P. L. Green, “Automatic fault detection for laser powder-bed fusion using semi-supervised machine learning,” *Addit. Manuf.*, vol. 27, pp. 42–53, 2019, doi: 10.1016/j.addma.2019.01.006.
- [33] D. S. Egan, C. M. Ryan, A. C. Parnell, and D. P. Dowling, “Using in-situ process monitoring data to identify defective layers in Ti-6Al-4V additively manufactured porous biomaterials,” *J. Manuf. Process.*, vol. 64, pp. 1248–1254, Apr. 2021, doi: 10.1016/j.jmapro.2021.03.002.
- [34] A. Gökhan Demir, C. De Giorgi, and B. Previtali, “Design and Implementation of a Multisensor Coaxial Monitoring System with Correction Strategies for Selective Laser Melting of a Maraging Steel,” *J. Manuf. Sci. Eng. Trans. ASME*, vol. 140, no. 4, 2018, doi: 10.1115/1.4038568.
- [35] S. Jayasinghe, P. Paoletti, C. Sutcliffe, J. Dardis, N. Jones, and P. L. Green, “Automatic quality assessments of laser powder bed fusion builds from photodiode sensor measurements,” *Addit. Manuf.*, no. April, p. Preprints, 2020, doi: 10.20944/preprints202004.0055.v1.
- [36] P. Yadav, O. Rigo, C. Arvieu, E. Le Guen, and E. Lacoste, “Data Treatment of In Situ Monitoring Systems in Selective Laser Melting Machines,” *Adv. Eng. Mater.*, vol. 23, no. 5, pp. 1–15, 2021, doi: 10.1002/adem.202001327.
- [37] A. J. Dunbar and A. R. Nassar, “Assessment of optical emission analysis for in-process monitoring of powder bed fusion additive manufacturing,” *Virtual Phys. Prototyp.*, vol. 13, no. 1, pp. 14–19, Jan. 2018, doi: 10.1080/17452759.2017.1392683.
- [38] M. Montazeri, A. R. Nassar, A. J. Dunbar, and P. Rao, “In-process monitoring of porosity in

- additive manufacturing using optical emission spectroscopy,” *IISE Trans.*, vol. 52, no. 5, pp. 500–515, May 2020, doi: 10.1080/24725854.2019.1659525.
- [39] K. Artzt, M. Siggel, J. Kleinert, J. Riccius, G. Requena, and J. Haubrich, “Pyrometric-based melt pool monitoring study of CuCr1Zr processed using L-PBF,” *Materials (Basel)*, vol. 13, no. 20, pp. 1–22, Oct. 2020, doi: 10.3390/ma13204626.
- [40] M. Grasso and B. M. Colosimo, “Process defects and in situ monitoring methods in metal powder bed fusion: A review,” *Meas. Sci. Technol.*, vol. 28, no. 4, p. aa5c4f, 2017, doi: 10.1088/1361-6501/aa5c4f.
- [41] M. Pavlov, M. Doubenskaia, and I. Smurov, “Pyrometric analysis of thermal processes in SLM technology,” *Phys. Procedia*, vol. 5, no. n/a, pp. 523–531, 2010, doi: 10.1016/j.phpro.2010.08.080.
- [42] T. G. Fleming, S. G. L. Nestor, T. R. Allen, M. A. Boukhaled, N. J. Smith, and J. M. Fraser, “Tracking and controlling the morphology evolution of 3D powder-bed fusion in situ using inline coherent imaging,” *Addit. Manuf.*, vol. 32, p. 100978, Mar. 2020, doi: 10.1016/j.addma.2019.100978.
- [43] G. Repossini, V. Laguzza, M. Grasso, and B. M. Colosimo, “On the use of spatter signature for in-situ monitoring of Laser Powder Bed Fusion,” *Addit. Manuf.*, vol. 16, pp. 35–48, 2017, doi: 10.1016/j.addma.2017.05.004.
- [44] C. Gobert, E. W. Reutzel, J. Petrich, A. R. Nassar, and S. Phoha, “Application of supervised machine learning for defect detection during metallic powder bed fusion additive manufacturing using high resolution imaging,” *Addit. Manuf.*, vol. 21, no. n/a, pp. 517–528, 2018, doi: 10.1016/j.addma.2018.04.005.
- [45] L. Fuchs and C. Eischer, “In-process monitoring systems for metal additive manufacturing,” *White paper*, 2018. <https://www.eos-apac.info/upload/2020-07/159522956575650000.pdf>.
- [46] SLM Solution, “Melt pool monitoring,” *Report*, p. 1.
- [47] SLM Solution, “Laser Power Monitoring,” *Report*, pp. 1–2, [Online]. Available: https://www.slm-solutions.com/fileadmin/user_upload/downloads/de/603xx171025-01-001-lpm_web.pdf.

- [48] T. Toepfel *et al.*, “3D analysis in laser beam melting based on real-time process monitoring,” *Mater. Sci. Technol. Conf. Exhib. 2016, MS T 2016*, vol. 1, pp. 123–132, 2016.
- [49] M. A. Doubenskaia, I. Y. Smurov, V. I. Teleshevskiy, P. Bertrand, and I. V. Zhirnov, “Determination of True Temperature in Selective Laser Melting of Metal Powder Using Infrared Camera,” *Mater. Sci. Forum*, vol. 834, no. November, pp. 93–102, 2015, doi: 10.4028/www.scientific.net/msf.834.93.
- [50] Renishaw PLC, “InfiniAM Spectral – Energy input and melt pool emissions monitoring for AM systems,” *Report*, pp. 1–5, 2017, [Online]. Available: <http://resources.renishaw.com/en/details/data-sheet-renam-500q--99032>.
- [51] T. Furumoto, M. R. Alkahari, T. Ueda, M. S. A. Aziz, and A. Hosokawa, “Monitoring of Laser Consolidation Process of Metal Powder with High Speed Video Camera,” *Phys. Procedia*, vol. 39, pp. 706–766, 2012, doi: 10.1016/j.phpro.2012.10.098.
- [52] T. Furumoto, T. Ueda, M. R. Alkahari, and A. Hosokawa, “Investigation of laser consolidation process for metal powder by two-color pyrometer and high-speed video camera,” *CIRP Ann. - Manuf. Technol.*, vol. 62, no. 1, pp. 223–226, 2013, doi: 10.1016/j.cirp.2013.03.032.
- [53] A. Gaikwad, F. Imani, P. Rao, H. Yang, and E. Reutzel, “Design rules and in-situ quality monitoring of thin-wall features made using laser powder bed fusion,” in *proceedings of the ASME 2019 14th International Manufacturing Science and Engineering Conference (MSEC2019)*, 2019, p. 20, doi: 10.1115/MSEC2019-3035.
- [54] T. Craeghs, S. Clijsters, J. P. Kruth, F. Bechmann, and M. C. Ebert, “Detection of Process Failures in Layerwise Laser Melting with Optical Process Monitoring,” *Phys. Procedia*, vol. 39, pp. 753–759, 2012, doi: 10.1016/j.phpro.2012.10.097.
- [55] C. Foster, B., Reutzel, E., Nassar, A., Hall, B.T., Brown, S., & Dickman, “Optical, layerwise monitoring of powder bed fusion,” in *Solid Freedom Fabrication Symp. Proc. pp 295–307*, 2015, p. 13.
- [56] M. Abdelrahman, E. W. Reutzel, A. R. Nassar, and T. L. Starr, “Flaw detection in powder bed fusion using optical imaging,” *Addit. Manuf.*, vol. 15, no. n/a, pp. 1–11, 2017, doi: 10.1016/j.addma.2017.02.001.
- [57] G. Zenzinger, J. Bamberg, A. Ladewig, T. Hess, B. Henkel, and W. Satzger, “Process

- monitoring of additive manufacturing by using optical tomography,” in *AIP Conference Proceedings*, vol. 1650, no. 1, 2015, pp. 164–170, doi: 10.1063/1.4914606.
- [58] J. Bamberg, G. Zenzinger, and A. Ladewig, “In-Process Control of Selective Laser Melting by Quantitative Optical Tomography,” in *19th World Conference on Non-Destructive Testing*, 2016, p. 8.
- [59] A. Gögelein, A. Ladewig, G. Zenzinger, and J. Bamberg, “Process Monitoring of Additive Manufacturing by Using Optical Tomography,” 2018, doi: 10.21611/qirt.2018.004.
- [60] J. Petrich, C. Gobert, S. Phoha, A. R. Nassar, and E. W. Reutzel, “Machine learning for defect detection for PBFAM using high resolution layerwise imaging coupled with post-build CT scans,” in *Solid Freeform Fabrication 2017: Proceedings of the 28th Annual International Solid Freeform Fabrication Symposium - An Additive Manufacturing Conference, SFF 2017*, 2017, pp. 1363–1381.
- [61] F. Imani, A. Gaikwad, M. Montazeri, P. Rao, H. Yang, and E. Reutzel, “Layerwise in-process quality monitoring in laser powder bed fusion,” in *ASME 2018 13th International Manufacturing Science and Engineering Conference, MSEC 2018, Vol. 51357*, 2018, p. V001T01A038, doi: 10.1115/MSEC2018-6477.
- [62] L. Scime and J. Beuth, “Using machine learning to identify in-situ melt pool signatures indicative of flaw formation in a laser powder bed fusion additive manufacturing process,” *Addit. Manuf.*, vol. 25, pp. 151–165, 2019, doi: 10.1016/j.addma.2018.11.010.
- [63] M. Mahmoudi, A. A. Ezzat, and A. Elwany, “Layerwise Anomaly Detection in Laser Powder-Bed Fusion Metal Additive Manufacturing,” *J. Manuf. Sci. Eng. Trans. ASME*, vol. 141, no. 3, Mar. 2019, doi: 10.1115/1.4042108.
- [64] Z. Snow, B. Diehl, E. W. Reutzel, and A. Nassar, “Toward in-situ flaw detection in laser powder bed fusion additive manufacturing through layerwise imagery and machine learning,” *J. Manuf. Syst.*, vol. 59, no. October 2020, pp. 12–26, 2021, doi: 10.1016/j.jmsy.2021.01.008.
- [65] N. Eschner, L. Weiser, B. Häfner, and G. Lanza, “Classification of specimen density in Laser Powder Bed Fusion (L-PBF) using in-process structure-borne acoustic process emissions,” *Addit. Manuf.*, vol. 34, 2020, doi: 10.1016/j.addma.2020.101324.
- [66] L. Scime, D. Siddel, S. Baird, and V. Paquit, “Layer-wise anomaly detection and classification

for powder bed additive manufacturing processes: A machine-agnostic algorithm for real-time pixel-wise semantic segmentation,” *Addit. Manuf.*, vol. 36, Dec. 2020, doi: 10.1016/j.addma.2020.101453.

- [67] S. A. Shevchik, C. Kenel, C. Leinenbach, and K. Wasmer, “Acoustic emission for in situ quality monitoring in additive manufacturing using spectral convolutional neural networks,” *Addit. Manuf.*, vol. 21, pp. 598–604, 2018, doi: 10.1016/j.addma.2017.11.012.
- [68] A. Caggiano, J. Zhang, V. Alfieri, F. Caiazzo, R. Gao, and R. Teti, “Machine learning-based image processing for on-line defect recognition in additive manufacturing,” *CIRP Ann.*, vol. 68, no. 1, pp. 451–454, 2019, doi: 10.1016/j.cirp.2019.03.021.
- [69] D. S. Ertay *et al.*, “Toward Sub-Surface Pore Prediction Capabilities for Laser Powder Bed Fusion Using Data Science,” *J. Manuf. Sci. Eng.*, vol. 143, no. 7, 2021, doi: 10.1115/1.4050461.
- [70] G. Tapia, A. H. Elwany, and H. Sang, “Prediction of porosity in metal-based additive manufacturing using spatial Gaussian process models,” *Addit. Manuf.*, vol. 12, pp. 282–290, 2016, doi: 10.1016/j.addma.2016.05.009.
- [71] J. Williams, P. Dryburgh, A. Clare, P. Rao, and A. Samal, “Defect detection and monitoring in metal additive manufactured parts through deep learning of spatially resolved acoustic spectroscopy signals,” *Smart Sustain. Manuf. Syst.*, 2018, doi: 10.1520/SSMS20180035.
- [72] O. Kwon *et al.*, “A deep neural network for classification of melt-pool images in metal additive manufacturing,” *J. Intell. Manuf.*, vol. 31, pp. 375–386, 2020, doi: 10.1007/s10845-018-1451-6.
- [73] Y. Zhang, G. S. Hong, D. Ye, K. Zhu, and J. Y. H. Fuh, “Extraction and evaluation of melt pool, plume and spatter information for powder-bed fusion AM process monitoring,” *Mater. Des.*, vol. 156, pp. 458–469, 2018, doi: 10.1016/j.matdes.2018.07.002.
- [74] G. Tapia, S. Khairallah, M. Matthews, W. E. King, and A. Elwany, “Gaussian process-based surrogate modeling framework for process planning in laser powder-bed fusion additive manufacturing of 316L stainless steel,” *Int. J. Adv. Manuf. Technol.*, vol. 94, no. 9, pp. 3591–3603, 2018, doi: 10.1007/s00170-017-1045-z.
- [75] R. J. Smith, W. Li, J. Coulson, M. Clark, M. G. Somekh, and S. D. Sharples, “Spatially

resolved acoustic spectroscopy for rapid imaging of material microstructure and grain orientation,” *Meas. Sci. Technol.*, vol. 25, no. 5, p. 055902, 2014, doi: 10.1088/0957-0233/25/5/055902.

- [76] K. He, X. Zhang, S. Ren, and J. Sun, “Deep residual learning for image recognition,” in *Proceedings of the IEEE Computer Society Conference on Computer Vision and Pattern Recognition*, 2016, pp. 770–778, doi: 10.1109/CVPR.2016.90.
- [77] G. Huang, Z. Liu, L. Van Der Maaten, and K. Q. Weinberger, “Densely connected convolutional networks,” in *Proceedings - 30th IEEE Conference on Computer Vision and Pattern Recognition, CVPR 2017*, 2017, pp. 4700–4708, doi: 10.1109/CVPR.2017.243.
- [78] R. Esmailizadeh *et al.*, “Customizing mechanical properties of additively manufactured Hastelloy X parts by adjusting laser scanning speed,” *J. Alloys Compd.*, vol. 812, p. 152097, 2020, doi: 10.1016/j.jallcom.2019.152097.
- [79] J. A. Kanko, A. P. Sibley, and J. M. Fraser, “In situ morphology-based defect detection of selective laser melting through inline coherent imaging,” *J. Mater. Process. Technol.*, vol. 231, no. n/a, pp. 488–500, 2016, doi: 10.1016/j.jmatprotec.2015.12.024.
- [80] T. Fawcett, “An introduction to ROC analysis,” *Pattern Recognit. Lett.*, 2006, doi: 10.1016/j.patrec.2005.10.010.
- [81] D. Chicco and G. Jurman, “The advantages of the Matthews correlation coefficient (MCC) over F1 score and accuracy in binary classification evaluation,” *BMC Genomics*, vol. 21, no. 1, pp. 1–13, 2020, doi: 10.1186/s12864-019-6413-7.
- [82] J. Reijonen, A. Revuelta, T. Riipinen, K. Ruusuvoori, and P. Puukko, “On the effect of shielding gas flow on porosity and melt pool geometry in laser powder bed fusion additive manufacturing,” *Addit. Manuf.*, vol. 32, p. 101030, 2020, doi: 10.1016/j.addma.2019.101030.
- [83] B. Ferrar, L. Mullen, E. Jones, R. Stamp, and C. J. Sutcliffe, “Gas flow effects on selective laser melting (SLM) manufacturing performance,” *J. Mater. Process. Technol.*, vol. 212, no. 2, pp. 355–364, 2012, doi: 10.1016/j.jmatprotec.2011.09.020.
- [84] H. Baumgartl, J. Tomas, R. Buettner, and M. Merkel, “A deep learning-based model for defect detection in laser-powder bed fusion using in-situ thermographic monitoring,” *Prog. Addit. Manuf.*, vol. 5, pp. 277–285, 2020, doi: 10.1007/s40964-019-00108-3.

- [85] S. Coeck, M. Bisht, J. Plas, and F. Verbist, "Prediction of lack of fusion porosity in selective laser melting based on melt pool monitoring data," *Addit. Manuf.*, vol. 25, no. September 2018, pp. 347–356, 2018, doi: 10.1016/j.addma.2018.11.015.
- [86] S. Haykin, "Chapter 9: Self-Organizing Maps," *Neural Networks A Compr. Found.*, 1999.
- [87] R. Kamimura, "Information-Theoretic Approach to Interpret Internal Representations of Self-Organizing Maps," in *Self Organizing Maps - Applications and Novel Algorithm Design*, 2011.
- [88] V. Chaudhary, R. S. Bhatia, and A. K. Ahlawat, "A novel Self-Organizing Map (SOM) learning algorithm with nearest and farthest neurons," *Alexandria Eng. J.*, 2014, doi: 10.1016/j.aej.2014.09.007.
- [89] R. Coppen, A. Banks, E. Briggs, K. Borgendale, and R. Gupta, "MQTT Version 5.0," *OASIS Standard*, 2019. <https://docs.oasis-open.org/mqtt/mqtt/v5.0/mqtt-v5.0.html>.